Skin Dynamics in the Tactile Sensing of Shape

by

Joshua P. Cysyk

Bachelor of Science, Engineering Science and Mechanics
Pennsylvania State University, 1997

Submitted to the Department of Electrical Engineering and Computer Science
in partial fulfillment of the requirements for the degree of

Masters of Science in Electrical Engineering and Computer Science

at the

MASSACHUSETTS INSTITUTE OF TECHNOLOGY

September 1999

Author..... .....
Department of Electrical Engineering and Computer Science
September 30, 1999

Certified by..... .....
Dr. Mandayam A. Srinivasan
Principal Research Scientist
Thesis Supervisor

Accepted by..... .....
Arthur C. Smith
Chairman, Departmental Committee on Graduate Students

Skin Dynamics in the Tactile Sensing of Shape

by

Joshua P. Cysyk

Submitted to the Department of Electrical Engineering and Computer Science
on September 30, 1999 in Partial Fulfillment of the
Requirements for the Degree of Master of Science in
Electrical Engineering and Computer Science

ABSTRACT

This thesis is focused on understanding the biomechanics of the human tactile system. During touch, Slowly Adapting Type-I (SA-I) receptors beneath the skin surface are mechanically loaded and respond with a series of neural impulses. The current research is to determine the relevant mechanical stimulus for the SA-I mechanoreceptors during tactile encoding of object shape.

A multilayered finite element model of the human fingerpad was created that accurately represented its internal and external geometry. By matching model predictions with biomechanical experimental data, the viscoelastic parameters for each skin layer were estimated and the biomechanical behavior of the model was validated. To simulate the mechanics of touch, surfaces of different curvatures were indented into the finger model, and the contact force was held constant until steady state conditions were reached. In addition, a surface of alternating convex and concave segments, each with a different curvature, was stroked across the finger at various velocities. The results from the simulation studies were compared with previously obtained neurophysiological data from the corresponding experiments.

The principal findings are as follows. (1) Under both indentation and stroking of shaped objects, the contact pressure across the fingerpad is the primary mechanical stimulus, and it is found to be directly proportional to the object curvature. (2) The use of a layered model, as opposed to a homogeneous model, has a profound effect on the shape of the contact pressure distribution across the skin surface. (3) The strain energy at depths below the skin surface can be predicted from a convolution sum of the contact pressure distribution. (4) A linear combination of the strain energy and the strain energy rate at typical mechanoreceptor locations can reasonably predict the SA-I neural response during both indentation and stroking experiments.

Thesis Supervisor: Dr. Mandayam A. Srinivasan
Title: Principal Research Scientist.

Acknowledgements

I would like to thank my advisor, Srini, for the guidance and intuition that he gave me during my thesis research. I also appreciate his patience and positive attitude that he has shown me over the years that I've been in his lab.

I would like to thank Raju and Suvranu for the knowledge they passed on to me over the past two years.

I would like to thank my lab mates in general, Raju, Suvranu, Chi-Hao, Cagatay, Tim, James, Guru, Wan-Chen, and any others who have passed through, for making the lab atmosphere enjoyable.

I would like to thank my family, especially my parents, for giving me guidance and support, and not asking too much of me while I was working on my thesis.

I would like to thank my friends for giving me enough distractions to get my mind off my research when I needed to.

And of course I would like to thank Christine, whose support, caring, and understanding have been of tremendous importance to me.

Contents

List of Figures

List of Tables

1

Introduction

1.1 Overview

The sense of touch plays a role in every facet of life. Touch receptors are located in the skin throughout the entire human body, and these receptors are constantly providing information about the world around us. Still, however, little is understood about the complex mechanisms involved in touch. The use of artificial touch sensors is beginning to gain prominence in the engineering industry, but the technology is far inferior to the biological counterpart. The human tactile system is capable of coding and decoding touch information in a far more efficient and expedient manner than man-made sensors can. A complete understanding of human touch could provide a tool that scientists and engineers could use for artificial limbs, tactile displays, robotic touch sensors, virtual realty haptic interfaces, and an endless amount of new possibilities.

As the finger comes into contact with an object, there are two parallel sensory mechanisms that occur: (1) tactile encoding, where mechanoreceptors under the skin respond to force and deformation applied at the skin surface; and (2) kinesthetic encoding of information provided by the posture and motion of the finger along with forces sensed at the joints, muscles, and tendons.

The focus of this research is in understanding the tactile encoding of information, which can be organized into a series of stages:

1. The object comes into contact with the fingerpad, deforms the skin, and creates a pressure distribution over the contact region.
2. This pressure and deformation field filters through the skin, producing a stress-strain distribution throughout the finger.
3. Mechanoreceptors at various depths below the skin surface are subjected to the mechanical loading, and respond by releasing a series of neural impulses.
4. The brain decodes the information contained in the neural impulses, providing a tactile image of the object in contact with the skin.

Research in the field of the human tactile system is generally aimed at understanding one step of the process. Psychophysical studies focus on determining the relationship between the physical features of an object and the human perception of that object during touch. Neurophysiological studies attempt to understand the role of each mechanoreceptor by recording neural impulses discharged during various contact conditions. Biomechanical studies concentrate on the mechanical state of the skin during touch, in an effort to relate the pressure field at the skin's surface and the subsurface stresses to the firing mechanism of various mechanoreceptors.

1.2 Motivation

This thesis focuses on understanding the biomechanics aspect of touch. The goal is to understand the relevant mechanical stimulus or stimuli for each mechanoreceptor. In order to accomplish this, the mechanics of touch must be understood. As the finger comes in contact with an object, skin deformation occurs and a contact pressure distribution presents itself on the skin surface. This pressure profile filters through the skin and places stresses and strains upon the mechanoreceptor. Unfortunately, no current experimental techniques can measure the stress field under the skin during touch. For this reason a mechanistic model of the finger must be created in order to reliably predict

the relevant mechanical parameters. The finite element method provides an accurate and robust method to model the mechanical properties of the fingerpad. Previous research has proven the finite element method to be a useful tool in investigating the mechanics of touch. The goal of this thesis research is to probe further into the mechanics of touch through the use of a finite element model of the fingerpad. By simulating various contact conditions and comparing the results to neurophysiological recordings, the mechanical parameters that determine the neural firing patterns can be understood. This knowledge would be able to provide a relationship between the macroscopic properties of touch to the neural mechanisms of impulse generation under the skin surface. This would aid in the development of prosthetic fingers, human-machine tactile interfaces, robotic touch sensors, and a broad array of haptic devices.

1.3 Thesis Overview

The goal of this thesis is to understand further the biomechanics involved in tactile sensing. Focus will be on Slowly Adapting Type-I (SA-I) receptors innervating the fingerpad. Previous neurophysiological research has recorded the neural impulses from these receptors during ramp and hold indentation experiments with surfaces of various curvatures, and during experiments where curved surfaces were stroked across the fingerpad. Using a finite element model, these same experiments will be simulated, and the results will be correlated with the neurophysiological recordings. An attempt will be made to develop a unifying model that describes the behavior of SA-I mechanoreceptors during touch. The research will be described in stages as follows.

Chapter 2 provides background information necessary in the study of human haptics. The anatomy of the finger, the role of different mechanoreceptor types, and the generation of action potentials are discussed. Previous research is summarized, and the need for continued studies is established.

Chapter 3 discusses the use of cross-sectional images of the fingertip obtained using MRI to develop a finite element model with realistic internal and external geometry. The verification of the model using surface deformation profiles and force response data is described.

Chapter 4 describes the simulation of ramp and hold experiments with surfaces of various shapes. The mechanical properties of contact are explained. Comparison with neurophysiological recordings is discussed, and a candidate relevant stimulus is proposed.

Chapter 5 deals with the stroking of curved surfaces across the finger. The relevant stimulus model is further discussed and verified. Inner ridges are introduced into the model, and their role in touch is investigated.

Chapter 6 summarizes the important findings in this research and discusses possible areas for future work.

2

Background

2.1 Human Fingertip

The human hand is used for exploration and manipulation in the surrounding environment. The fingertip is the primary tool for tactile sensing and information gathering about the shape, size, and texture of objects. The fingertip contains a high density of nerve fibers that detect and encode objects indenting into the skin surface. A rigid bone through the center of the finger provides the support needed for tactile exploration, while the surrounding skin is deformable to allow for shapes and textures to present a force profile on the skin surface. The average fingertip size in humans is 10-20 mm in diameter. Ridges are present on the surface of the skin that can act as levers to assist in the detection of movement and vibrational cues.

The human skin is a complex organ with many functional components. In addition to providing a touch sensing interface with the environment, skin also transmits information about temperature and emotions, such as blushing and the release of pheromones. The skin regulates body temperature through sweat glands and serves as a protection barrier for the body against hot and cold, infection, water and electrolyte loss, harmful chemicals, and UV radiation.

The human fingerpad skin is comprised of the epidermis and dermis layers. Figure 2-1 shows a cross-section of the human fingertip skin. The epidermis is the outermost layer of the fingertip skin. The epidermis is comprised of five layers, from outside to inside: the stratum corneum, the stratum lucidum, the stratum granulosum, the malphigian layer,

and the stratum basale. The stratum corneum is the outer layer containing dead keratinocytes. This layer is water proof and provides protection from the environment. The stratum basale is attached to the basement membrane which in turn is connected to the dermis by collagen fibrils. Despite its small thickness, the epidermis is considerably stronger and stiffer than the dermis region. On the surface of the epidermis are a series of ridges that determine the fingerprint of an individual. Between the epidermis and the dermis are another series of ridges that mimic the exterior ridges. The shallow ridge is the limiting ridge, and the deeper ridge with the sweat gland terminals are the intermediate ridges. These ridges are thought to serve as a lever, amplifying the surface forces to subsurface tactile sensors (Tubiana, 1981).

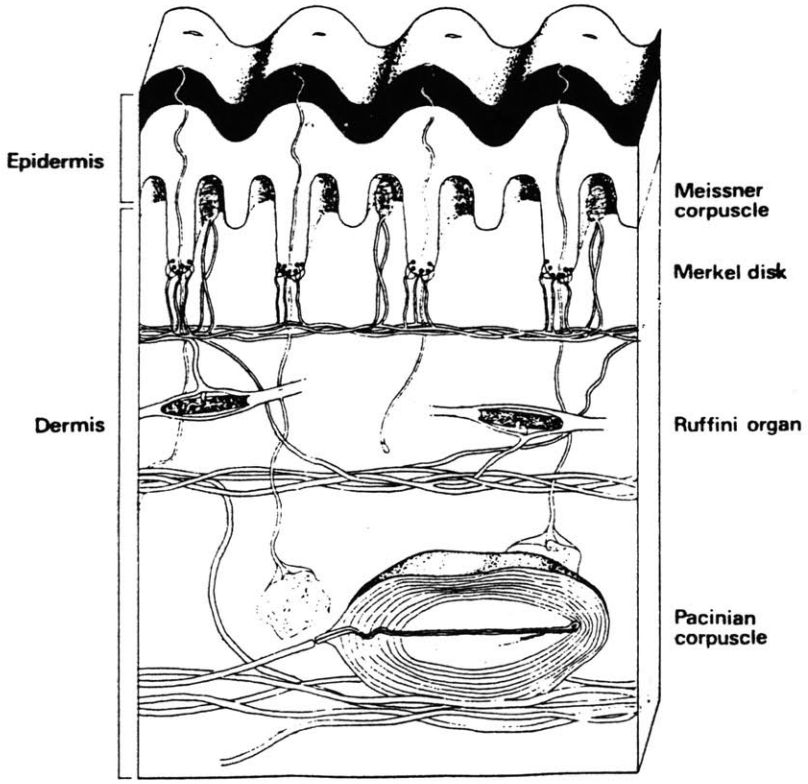

Figure 2-1. Schematic of the epidermis and dermis layers of the human fingerpad. The outer and inner ridges can be seen, and the four types of mechanoreceptors are also shown (adapted from Darian-Smith, 1984).

The dermis can be divided into the papillary and reticular layer. The papillary layer is comprised of a network of fibrous and elastic tissue, weaved together to provide support to the epidermis layers. The reticular layer predominantly consist of collagen fibers that make up the bulk of the skin. Elastin fibers, blood vessels, nerves, and fat cells are interspersed throughout this layer to form the base of the skin.

2.2 Mechanoreceptors

The human hand is innervated by a variety of afferent nerve fibers. At the end of the nerve fibers are receptors that can be classified into three broad classes: mechanoreceptors, thermal receptors, and nociceptors. Mechanoreceptors are responsible for tactile sensing, and they will be reviewed here. The analysis of tactile sensing and mechanoreceptor response is based heavily on physiological studies on other animal species. However, histological studies on human hand tissue has shown that the structure and function of human mechanoreceptors mimic those seen in other primates (Burgess and Perl, 1973).

Approximately 17,000 mechanoreceptor units innervate the glabrous skin of the human hand (Johansson and Vallbo, 1983). They can be classified into four types depending on their size, location, and neural behavior. These are the Meissner's Corpuscles, Merkel Discs, Ruffini Corpuscles, and Pacinian Corpuscles, and their locations are shown in Figure 2-1. The properties of each mechanoreceptor are summarized in Table 2.1.

From studies on animals, the nerve fibers innervating the mechanoreceptors have been classified based on *ramp and hold* response. A stimulus is indented into the skin at the most sensitive spot (MSS) of the receptor, held at a constant force or constant displacement, and then released. The neural responses can be divided into two major categories as seen in Figure 2-2. Two afferent nerve fibers only respond to the dynamic phases of the ramp and hold, during indentation and release. These are the Rapidly Adapting (RA) afferents of the Meissner Corpuscles and the afferents of the Pacinian Corpuscles (PC). The other two afferents respond both during the dynamic phase and the

Table 2.1 Comparison of four mechanoreceptors found in the primate fingerpad (Adapted from Dandekar and Srinivasan, 1996).

	Merkel	Ruffini	Meissner	Pacini
Location	Basal layer cells of the epithelial glandular ridges	Dermis	Dermal papillae protruding upward into the epidermis	Deeper layers of dermis, subcutaneous fat
Depth	0.7–1.0 mm	0.8–1.5 mm	0.5–0.7 mm	1.2–2.0 mm
Size	10 μm	500–1000 μm long, 200 μm in central zone, and 30 – 40 μm diameter near the poles	100 x 50 μm	Long axis 0.3 – 1.5 mm, diameter 0.2 – 0.7 mm
Shape	Oval or rounded	Ellipsoidal	Ellipsoidal	Ovoid
Morphological Classification	Un-encapsulated, Epidermal	Encapsulated, Dermal	Encapsulated, Dermal	Encapsulated, Dermal
Structure	Groups of 5 – 10 cells at a site	4–5 layers of lamellar cells covered by a basement membrane	Each fiber has an irregular discoidal form oriented at right angles to the long axis of the corpuscle	Several layers of concentrically packed lamellar cells, subcapsular space filled with fluid
Sensitivity to Stimuli	Displacement and velocity	Displacement and velocity	Velocity	Velocity
Innervating Afferent Fiber	Slowly Adapting Type-I (SA-I)	Slowly Adapting Type-II (SA-II)	Rapidly Adapting (RA)	Pacinian (PC)

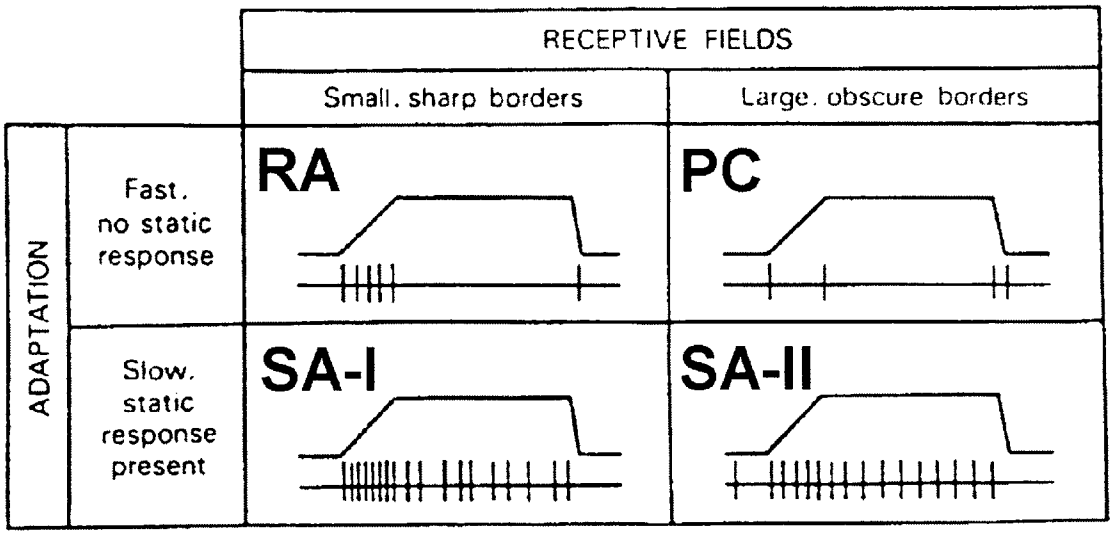

Figure 2-2. Classification of mechanoreceptive afferent units of the human hand, based on response to ramp and hold stimulation (Adapted from Johansson and Vallbo, 1983).

static hold phase of the experiment. They are termed Slowly Adapting Type-I (SA-I) and Slowly Adapting Type-II (SA-II) afferents, from the Merkel Discs and Ruffini Corpuscles, respectively.

2.3 Neuron Firing Mechanism

During touch, the stresses and strains on the mechanoreceptors cause a voltage depolarization in the afferent nerve cells. When the depolarization crosses a threshold, a neural impulse, or action potential, is fired. For each class of nerve afferent, the relevant tactile information is encoded in the frequency of the action potentials.

The action potential is an all or nothing event. Once the level of depolarization crosses a threshold (approximately –50 mV in most neurons), the magnitude of the action potential is independent of the stimulus strength. The threshold reflects the need to trigger the sodium gated ion channels. Once the sodium channels are open, Na^+ ions rush into the cell, depolarizing it further, causing more sodium channels to open, creating a positive

feedback loop. This regenerative process drives a rapidly accelerating increase in the membrane potential, termed an action potential. The peak of the action potential is around +55 mV, which is the Nernst equilibrium potential for Na^+. After an initial delay, potassium ion channels open, and there is an outflux of K^+ ions. This causes the voltage potential to drop rapidly, and hyperpolarization occurs where the cell potential drops below its resting potential. The potassium channels close, and the cell gradually returns to the resting potential. A full schematic of the action potential generation is shown in Figure 2-3.

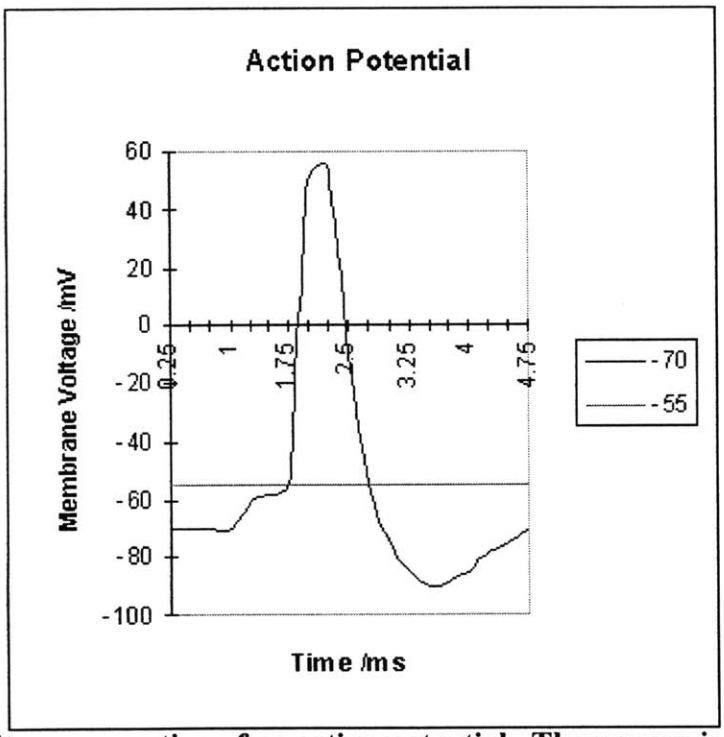

Figure 2-3. Voltage generation of an action potential. The neuron is at rest at –70 mV. A stimulus causes depolarization to occur. Once the voltage increase crosses the threshold of –55 mV, there is a rapid increase in voltage to a peak of 50 mV. Relaxation occurs and the cell returns to its resting potential. The rapid increase in voltage is referred to as the action potential (Adapted from Duncan).

After the peak of the action potential, there are two refractory periods, absolute and relative. During the absolute refractory period the sodium ion channels cannot open regardless of the magnitude of the stimulus. After this period, during the relative refractory period, the threshold for the sodium channels gradually decreases. Therefore, the greater the magnitude of the stimulus the sooner the threshold is crossed, and the subsequent creation of action potentials. It is because of this relative refractory period that the stimulus strength can be encoded by the frequency of neural impulses. Hodgkin and Huxley (1952) created an accurate model of this action potential generation mechanism for the giant squid axon hillock. .

The mechanism that causes the voltage depolarization in the mechanoreceptors of the human hand is not known. Stretch activated ion channels have been identified in mechanoreceptors in other parts of the body and in other species. Under mechanical loading, these channels stretch and inject a current into the cell. It is believed that the mechanoreceptors in the human hand operate under this mechanism (Levitan, 1991). Research has also shown the voltage depolarization is not only dependent on the stretch of the channel, but also on the stretch rate. Figure 2-4 is the voltage response of an isolated stretch activated ion channel, illustrating the dynamic effects of stretch rate.

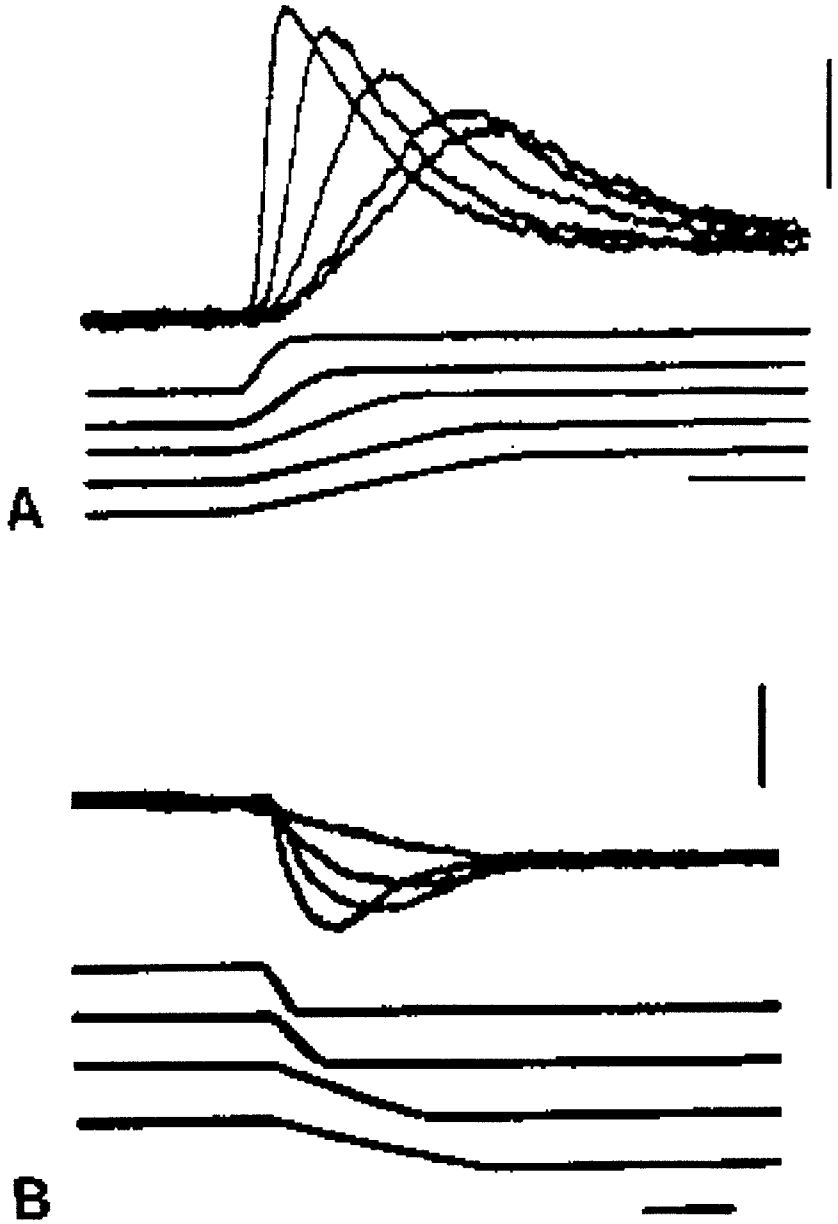

Figure 2-4. Dependence of the dynamic peak amplitude (A) and the post-release hyperpolarization amplitude (B) on the mechanical stimulus rate of growth and decay, respectively. The voltage response (top traces in A and B) is from an isolated stretch activated ion channel under mechanical stretch to the same final value with different stretch rates (bottom traces in A and B). (A) stretch to the final value of 250 μm; vertical bar line = 1 mV; horizontal bar line = 10ms. (B) stretch amplitude of 345 μm; vertical bar line = 4 mV; horizontal bar line = 500ms (adapted from Akoev, 1988).

2.4 *Previous Research*

Research on tactile sensing can be divided into three areas of study: biomechanics, neurophysiology, and psychophysics.

Biomechanics

Biomechanics research on tactile sensing is concerned with determining the mechanical properties of skin, the pressure and deformation profiles occurring during contact, and the stress-strain distribution throughout the fingerpad during touch. The overall focus is in understanding the mechanics behind touch, and the relevant stress-strain parameters which cause the various mechanoreceptors to fire neural impulses. Phillips and Johnson (1981b) first began studying the relationship between subsurface strain measures and neurological recordings. They proposed modeling the finger as an infinite, isotropic, linear elastic, homogenous medium. In an attempt to improve the model, Srinivasan (1989) proposed an incompressible fluid enclosed in an elastic membrane, the *waterbed model*. This model accurately depicted the surface deformation profile during contact, but could not predict the stress-strain distribution under the skin surface. Dandekar and Srinivasan (1996) began using finite element models to investigate the skin mechanics during touch. A three dimensional, multi-layered model of the fingertip was produced. This model accurately predicted the surface deformation during contact and was able to determine the stresses and strains occurring under the skin surface during touch. Raju and Srinivasan (1999), using this model, determined that the strain energy density was a good candidate as the relevant stimulus for SA-I afferent fibers.

In the MIT Touch Lab, the mechanical properties of the fingertip skin has been studied extensively in order to model the finger more accurately. Force response profiles were obtained from ramp and hold indentations into the finger of human subjects (Gulati and Srinivasan, 1996). Using the results from these experiments, the first order viscoelastic parameters of the skin were determined (De and Srinivasan, 1999). Surfaces were stroked across the finger of human subjects to determine the friction coefficient of skin (Liao and Srinivasan, 1999). The friction coefficient was found to be a function of the

indentation depth. Using Magnetic Resonance Imaging (MRI), the inner geometry of the fingerpad was imaged (Voss and Srinivasan, 1998).

Neurophysiology

Neurophysiological studies on tactile sensing are concerned with understanding the coding of object properties into neural impulses. As the objects are indented into or stroked across the fingerpad, the neural impulses from afferent nerve fibers are recorded. These neural impulses are all of the same magnitude, with the firing frequency coding all the touch information. Different types of mechanoreceptors and associated afferent nerve fibers exist under the skin, and they vary in location and in the relevant contact information coded into neural impulses. Rapidly Adapting (RA) and Pacinian (PC) afferents respond only to dynamic phases of contact, while Slowly Adapting Type-I (SA-I) and Slowly Adapting Type-II (SA-II) respond to both dynamic and static phases of contact. Phillips and Johnson (1981a) recorded neural impulses from slowly adapting fibers in monkeys, investigating the encoding of surface edges. Research has been done into temporal pattern encoding, through sinusoidal movement (Goodwin and Morley, 1987) and vibration (Freeman and Johnson, 1982a) studies. The encoding of shape, both statically and dynamically, through RA and SA-I type afferent fibers has been studied extensively. Ramp and hold experiments were done by LaMotte and Srinivasan (1993). Curved surfaces were moved across the fingerpad in a succession of steps (Srinivasan and LaMotte, 1987c) and stroked across the fingerpad (Srinivasan and LaMotte, 1987a, 1987b; LaMotte and Srinivasan, 1996), while recording the neural impulse patterns. Goodwin *et al* (1995) studied the representation of curvature in the impulse frequency of afferent fibers innervating the monkey fingerpad. Finger stretch and relative slip was investigated using glass plates with and without surface texture stroked across the finger (Srinivasan *et al*, 1990). Freeman and Johnson (1982) developed a linear circuit model of the mechanoreceptor firing mechanism. The model contained the membrane capacitance, receptor channels whose conductance is modified by mechanical deformation, and impulse channels that produce action potentials when the voltage potential exceeds threshold. Using this model, the frequency responses of SA-I, RA, and PC afferents to vibratory stimuli were predicted.

Psychophysics

Psychophysical research is aimed at understanding the relationship between an object stimulating the skin surface, and the behavioral response from the brain. Using carefully design test conditions, the relationship between the physical stimuli and the resulting human perception is investigated. The tactile encoding mechanism is treated as a black box. Specific research has involved the tactile study of roughness perception (Lederman and Taylor, 1972), spatial resolution (Loomis, 1979), texture discrimination (Lamb, 1983), curvature discrimination (Goodwin *et al* , 1991; Goodwin and Wheat, 1992), softness discrimination (Srinivasan and LaMotte, 1995), and thickness discrimination (John *et al.*, 1989; Ho and Srinivasan, 1996) during touch. Psychophysiological studies were combined with neurophysiological studies in order to relate neural responses to human perception during flutter-vibration (Talbot *et. al.*, 1968). Bolanowski *et. al.* (1988) reviews the psychophysical evidence that four "channels", with unique physical properties, participate in tactile perception.

2.5 Need for Continued Research

Previous biomechanical studies on touch have been focused on static indentation, or the steady state response during contact. During active exploration the finger is constantly moving across the surface of the object in order to gather a precise picture. To fully understand the mechanics of touch, the dynamic events need to be understood. Neurophysiological data is available from ramp and hold and stroking experiments. The next step is to correlate the time evolution of the neural response to the relevant mechanical properties of the fingerpad, as a curved surface is indenting and/or moving across the fingerpad. In order to accomplish this, a higher resolution model is needed that incorporates the viscoelastic properties of skin.

The previous finite element models are accurate in the external profile of the fingerpad, deformed and undeformed. To increase the validity of the model, the inner geometry of the fingerpad layers needs to be incorporated.

3

Fingerpad Model Generation and Verification

3.1 Motivation

During touch, as the fingerpad makes contact with an object, pressure is applied on the fingerpad, skin deformation occurs, and a stress and strain distribution develops throughout the fingerpad. The mechanoreceptors below the skin surface are subjected to the stress and strain field, resulting in emissions of neural impulses. The frequency of the impulses depends on the magnitude of the relevant stimulus for the various mechanoreceptors. In order to fully understand the functioning of SA mechanoreceptors, it is important to determine the relevant stimulus for each receptor. Ultimately, it is desirable to understand the transduction of the mechanical state of the fingerpad into neural impulses. During neurophysiological experiments on how object shape is represented in peripheral neural response, the input shape, the depth of indentation, and the resultant force are known with great accuracy. An SA mechanoreceptive fiber is selected and the neural impulses are recorded as tick marks, all of the same magnitude, only the firing frequency contains shape and contact information. Currently, no information pertaining to the mechanical state of the mechanoreceptors during touch can be directly measured. In order to estimate the stress/strain state of the mechanoreceptors, a model needs to be developed which accurately describes the biomechanics of the fingerpad. Using the same input parameters as in the neurophysiological experiments, the mechanical state of fingerpad can be computed and matched with the neurophysiological recordings, and the transduction mechanism of the receptors can be inferred.

Analytical models have been developed for the purpose of investigation touch mechanisms. (Phillips and Johnson, 1981; Srinivasan, 1989) These models are very specific to the boundary conditions and loads that can be applied, and to the amount of information that can be obtained from them. No analytical model has been developed which can fully explain the deformation and mechanical loading throughout the finger during touch. Fortunately, a numerical analysis procedure exists which enables the formulation of a complete mechanistic model of the finger under any possible loading: the finite element method

3.2 Finite Element Method

The finite element (FE) method is widely used to solve physical problems in engineering analysis and design (Bathe, 1996). The physical problem is first idealized by a mathematical model. In this mathematical model, assumptions are made about the geometry, material properties, loading, boundary conditions, etc. of the physical problem. Fluid dynamics, heat transfer, and solid mechanics problems are all examples of types of physical problems that can be modeled, each with its own set of assumptions and governing equations. For the fingerpad model, a continuum-mechanics mathematical model is implemented based on the theory of elasticity. This model produces a series of governing differential equations that in general cannot be solved analytically. The finite element method is a tool that solves these governing equations numerically. First, the continuum model is divided into a discrete number of elements and nodes, which encompass the entire volume of the problem. The external forces on the system are lumped onto the element nodes. Each element is controlled by the equilibrium equations governing the entire model. These elements are then assembled together so that they satisfy a set of compatibility requirements, and an algebraic set of simultaneous equations is developed. This set of equations is quite large for any problem of significance, and therefore, computer algorithms are used to solve the set of equations efficiently. ABAQUS is the finite element analysis package used for the numerical analysis in this research project (ABAQUS, 1998). The final solution satisfies the equilibrium equations only at the nodes and across each individual element, instead of continuously throughout

the entire model. If the element mesh is fine enough, then the nodal solution will be in close agreement with the continuum solution. It must be understood, however, that this is a numerical solution to the mathematical model, not the physical problem itself. If the initial assumptions in the model are incorrect, than a finer mesh will still produce erroneous results.

The fingerpad geometry and material properties are modeled using the finite element method. The loading and boundary conditions are specified, the formulated equations are solved using a computer based iterative algorithm, and the resulting mechanical state of the finger can be evaluated. The stress-strain fields are continuous across each element, it is only at the boundaries where discontinuities occur. Therefore, the mesh is refined to a point where the fields are reasonably continuous.

Once confidence in the model is attained, simulations can be performed for a wide variety of input conditions. Complex contact mechanics between the finger and a rigid object can be evaluated. Objects can be indented into the skin using prescribed force or prescribed displacement conditions over time, enabling the ramp and hold neurophysiological experiments to be simulated fully. Surfaces can be stroked along the skin, stretching or slipping across depending on the contact force and frictional parameters. With the use of the finite element model of the finger, the neurophysiological experiments can be simulated using the same prescribed conditions, and the mechanics of touch can be studied and understood.

Previous FE models of the fingerpad have been developed with encouraging results. (Dandekar and Srinivasan, 1996; Raju and Srinivasan, 1998) Dandekar and Srinivasan developed a three dimensional model of the finger pad, with realistic external geometry, incorporating multiple internal layers for the epidermis, dermis, and bone. Elastic material properties for the layers were determined and static indentation studies were conducted. A goal of this thesis was to develop a model that further improved upon the existing models. The internal and external geometry of the fingerpad is modeled more realistically and accurately. Using a finer mesh, the accuracy of the results in the major

regions of interest is improved. Viscoelasticity is incorporated into the material properties of the various layers to allow for time dependent analysis to occur. One alteration, which at first glance may appear to be a negative change, is that the new model is only two-dimensional. In many of the neurophysiological experiments of interest, the indented or stroked objects were surfaces varying only in two-dimensions, such as a cylinder indenting the surface or a wide, wavy surface stroking the skin. In these cases, plane strain assumptions are valid, and the problem can be modeled using only a cross section of the finger, and the contact *surface* is now only a line. Therefore, the two-dimensional model can give as reliable information in the regions of interest as the three-dimensional model can, while offering the advantage of having a much faster computation time. This allows for a finer mesh to be used in the areas under the skin where the mechanoreceptors are located. Also, time dependent loading conditions, such as stroking across the skin, can be analyzed in a reasonable amount of time, while including the additional complexities of friction and viscoelasticity. With the previous 3-D model, even on a supercomputer, these computations could not be performed in a reasonable manner that would allow for wide variety of stroking or indentation analyses to be completed.

The first step of creating the finite element model is to create the element mesh. Previously obtained images of the external and internal geometry of the fingerpad, using Magnetic Resonance Imaging (MRI) techniques, provided the basis for the development of the two-dimensional model of the fingerpad.

3.3 Generating the FE Mesh

MRI is capable of imaging a two-dimensional slice of the fingerpad *in vivo* with high enough resolution and contrast in a reasonable time. This technique can differentiate between all the soft tissues of the fingerpad, and therefore, gives a precise picture of the tissue boundaries both while the finger is free or is in static contact with an object. Voss and Srinivasan used MRI to image the fingerpad of different subjects undeformed and deformed (Voss and Srinivasan, 1998). Cylinders, bars, and line loads were indented

Axial section of the fingerpad with no load applied

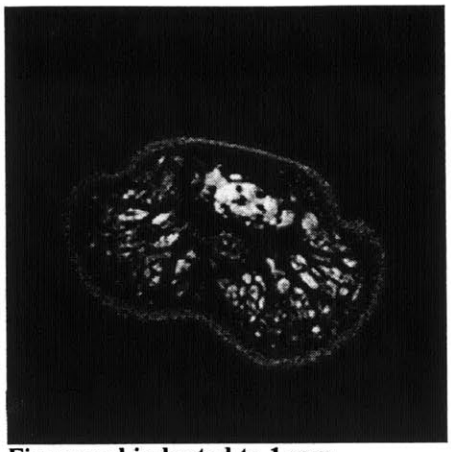

Fingerpad indented to 1 mm with a 1/8" diameter cylinder

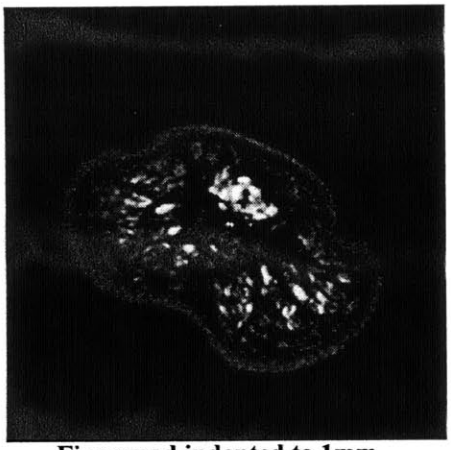

Fingerpad indented to 1mm with a 1/4" diameter cylinder

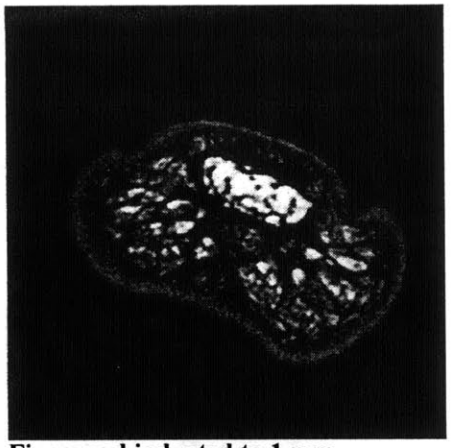

Fingerpad indented to 1 mm with a 1" diameter cylinder

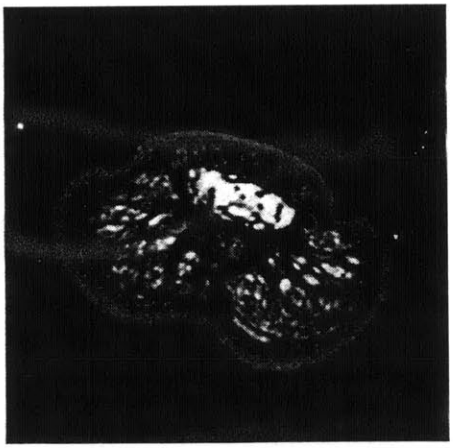

Fingerpad indented to 1 mm with a 1/16" wide rectangular bar.

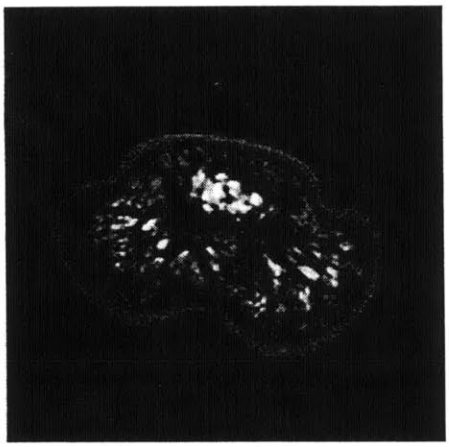

Fingerpad indented to 2 mm with a 1/16" wide rectangular bar.

Figure 3-1. MRI images of the human fingerpad (adapted from Voss and Srinivasan, 1998)

into the subjects fingers to various depths and held for imaging. This imaging does not provide a time evolution of the ramp and hold, only a static image of the end load condition. Figure 3-1 provides some examples of the images from one subject. Each layer is distinguished by the amount of water present, the more water the lighter the color; this is the simplified essence behind the MRI images of the fingertip. The layers were identified by their characteristics, as seen in Figure 3-2.

These images provide a basis for developing a finite element model. However, some care must go in to processing these images. There was a wide discrepancy between the different subjects' images. The goal of the model is to accurately describe the *average* person's fingerpad, not the specific irregularities that one person has and another one does not. In the neurophysiological recordings, there were discrepancies even between nerve fibers innervating the same fingerpad. Understanding these small nuances is not the objective; understanding the general patterns that occur during touch is. For this reason, the images were taken into as tools to assist in creating an *ideal* model of the fingerpad, that would represent all the essential characteristics.

Further investigation by Voss and Srinivasan found that a layer of the fingerpad was not imaged properly. The stratum corneum is the outer layer of the finger that consists of dead cells and little moisture, which is why it appears dark and not visible in the image. When the subject's finger was coated with Agrose to provide a watertight seal and placed under water, the *missing layer* became visible between the water and the rest of the fingerpad (Figure 3-3). Between the subjects the average thickness of this *missed* layer is around 350 μm. The average thickness of the next inner layer (the outermost light layer) is 400 – 500 μm. These two layers comprise the entire epidermis, giving a total thickness of 750-850 μm. This is in good agreement with the epidermis thickness of 700 to 900 μm given in previous publications. (Lockhart *et. al.*, 1965; Lanir *et. al.*, 1990) The image in Figure 3-3 was used as the general guideline for the model, with the addition of the strateum corneum layer.

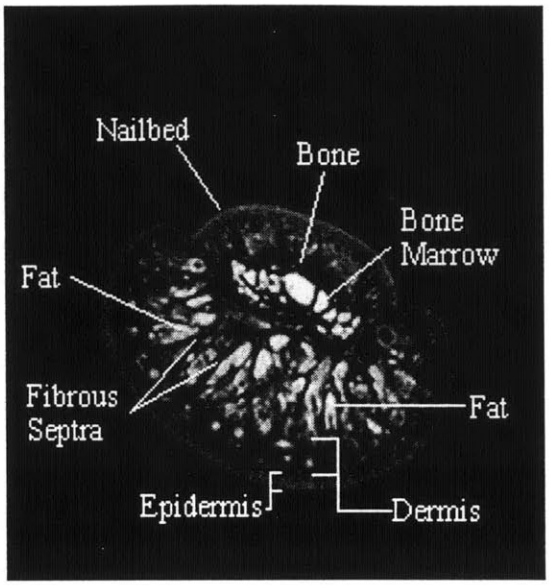

Figure 3-2. MRI image of the fingerpad, labeling the important features (adapted from Voss and Srinivasan, 1998)

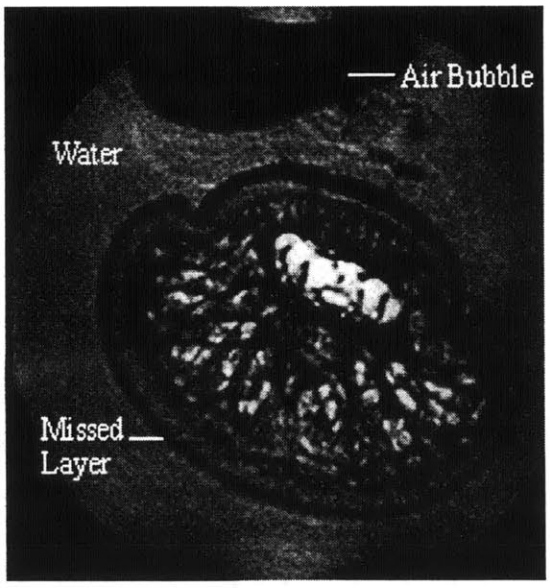

Figure 3-3. MRI image of the fingerpad coated with Agrose, showing the strateum corneum layer that was missed in the previous images. (adapted from Voss and Srinivasan, 1998)

The first step is to define the boundaries within which the mesh will be created. From the MRI images it can be seen that there are no clear cut boundaries that surround any layer, and especially the boundary between the dermis and the cutaneous fat layer is very fuzzy. Figure 3-4 shows the boundaries created around the MRI model that will eventually become the FE mesh. The white area at the bottom of the fingerpad is the bone marrow, around which is a thin black area before the fat layer begins. This region is the bone. The boundary between the bone and the fat layers is very ill-defined, but because this region will be rigid, and the relevant forces will be filtered down before then, the exact placement of the bone is not crucial for our purpose. The boundaries shown in Figure 3-4a are asymmetric. Previous FE models of the fingerpad that have been used were asymmetric. Results from these models often contained irregularities that were just inherent artifacts due to the asymmetry. In order to eliminate the unwanted artifacts, the model was intentionally made perfectly symmetric, with smooth boundaries. The original image with the ideal boundaries superimposed is shown in Figure 3-4b, and as can be seen there is good agreement between the two. The layer that was missed during the MRI is added at a uniform thickness around the image, to give the boundaries that will be used to create the FE mesh. (Figure 3-4c)

The finite element mesh is shown in Figure 3-5. About 10,000 nodes and elements are used. The outer two layers were combined to form the epidermis layer (850 μm thick); the second layer is the dermis (850 μm thick), and the third layer is the cutaneous fat layer. Because the bone is to be modeled as a rigid layer, much more stiff than the skin layers, the bone marrow layer will have no effect on the simulations. For that reason, the two inner layers were combined to form one rigid bone layer. In all the soft tissue layers, for sufficient spatial resolution a high mesh density is needed. If the entire model were meshed with a large mesh density, the simulations would be extremely computer intensive. However, the main region of interest is only a few millimeters below the skin surface, where the receptors lie. Therefore, the region near the surface has the highest mesh density, with a minimum element size of 120 μm. Away from this area the element size gradually increases until reaching the fingernail where there are only a few elements.

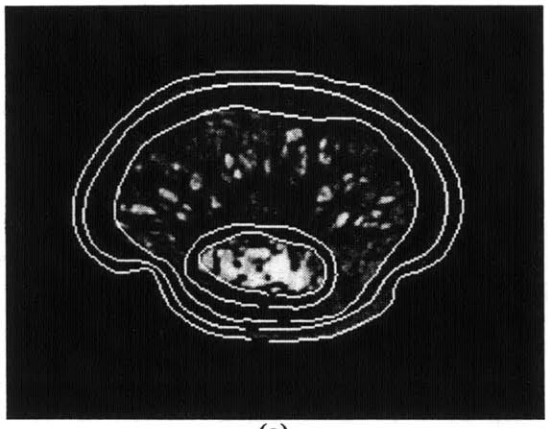

(a)

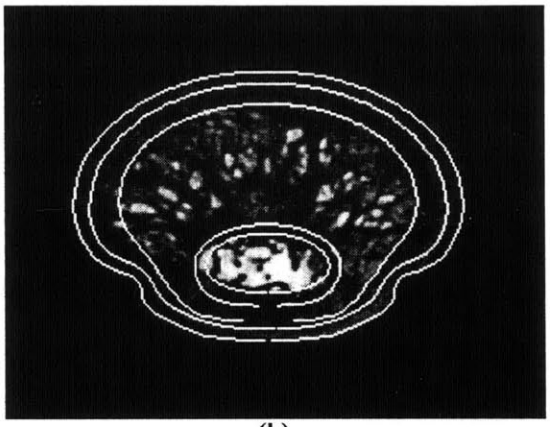

(b)

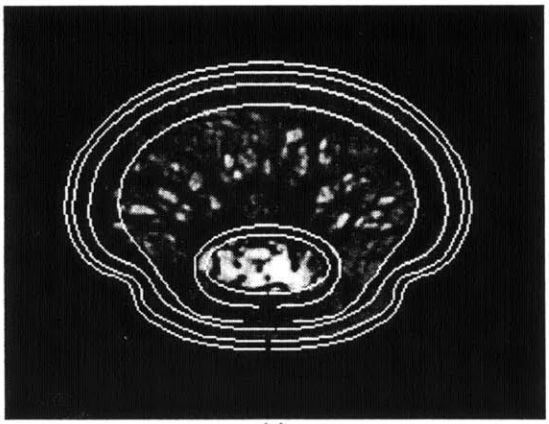

(c)

Figure 3-4. Generation of the boundaries for the FE model from the MRI undeformed image. (a) Boundaries are defined around the epidermis, dermis, cutaneuos fat, bone, and bone marrow layers. (b) The boundaries are smoothed and made symmetrical to remove any artifacts. (c) The strateum corneum layer that was not visible in the MRI imaging, is included as a uniform boundary around the existing model.

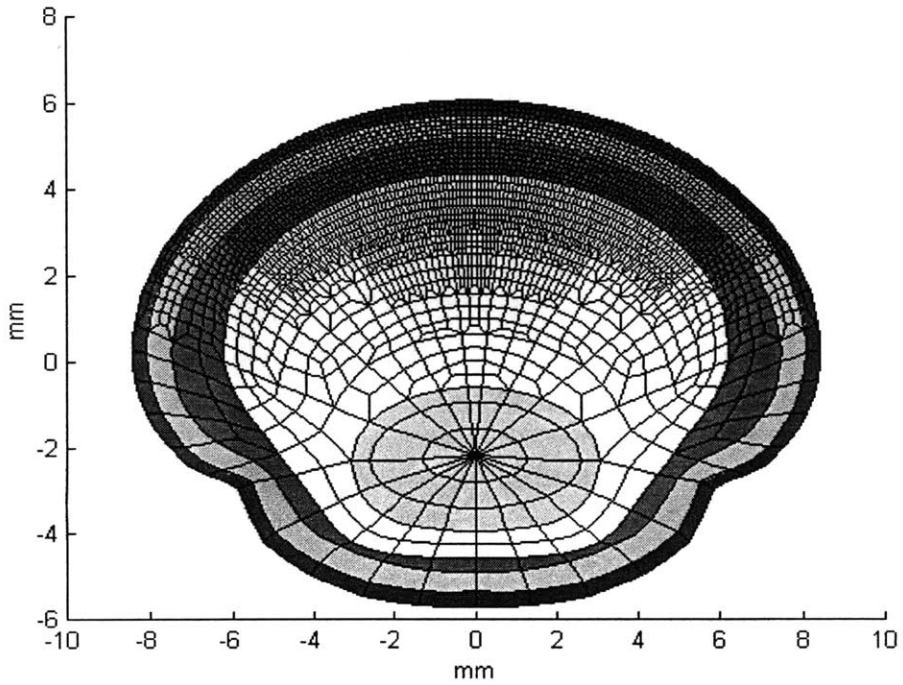

Figure 3-5. Finite element model of the fingerpad used for simulations. 10,000 nodes and elements are incorporated. In the main region of interest, the element size is 120 microns. The shaded layers are, from outside to inside, the strateum corneum, epidermis, dermis, cutaneous fat, and bone.

3.4 Material Properties

The skin is a composite of many fibrous, cellular, vascular and granular components, which make it clearly inhomogeneous, anisotropic, and non-linear. Modeling the skin properties exactly would be an immense task, and experimental data is not available to model the complexity of the skin. The components within the skin, however, are much smaller than the global size of the finger. Therefore, the finger can be modeled as a succession of layers through the skin, each layer treated as a homogeneous, linear, isotropic material. While this may seem to be a broad simplification, the attempt is to model the global characteristics of each skin layer, not the minute structures that are present. Experimental data is available on the global properties of skin, such as force response data and deformation profiles for the primate fingertip. If the simplified,

layered model can fit the experimental data, then the material properties incorporated are closest to the actual properties of skin that is achievable at this time, until further experimental data is available. Using this model, in order to completely describe the mechanical properties of each layer the Young's modulus and Poisson's ratio must be determined, along with the relevant viscoelastic parameters.

No experimental data exists on the Poisson's ratio of *in vivo* skin. Most scientists in the field agree that the skin is nearly incompressible, $\nu \cong 0.5$. In the finite element simulations, numerical instabilities occurred as ν approached this value. Therefore, $\nu = 0.48$, is used as the Poisson's ratio for the finite element analysis. Dandekar and Srinivasan (1996), using a hybrid element formulation, was able to check their model using $\nu = 0.499$ in the finite element analysis (Dandekar and Srinivasan, 1996). However, they found no significant difference in the results attained from either value.

To fully specify the fingertip model, the Young's modulus for each layer must be estimated. For stimuli prescribed as displacements in the analysis in a homogenous finite element model, it can be shown that the strains are independent of the Young's modulus (Dandekar and Srinivasan, 1996). Because the model is comprised of a series of homogenous layers, only the ratio of the Young's moduli for the layers needs to be determined. The stresses are related to the strains by a multiplicative constant, and therefore, for the purposes of determining data trends, the exact value of Young's modulus is not needed. Based on numerical experiments with a variety of Young's modulus ratios and the corresponding matches with experimental data, Dandekar and Srinivasan (1996) proposed the ratio between the layers as $10^4:10^3:10^3:10^8$ for the epidermis, dermis, fat, and bone layers, respectively (referred to as the 4:3:3:8 model). The bone is made many orders of magnitude stiffer than the skin, in effect making it a rigid body. Experimental data provided the surface deformation profiles for different indentation depths. The 4:3:3:8 ratio is incorporated into the new model, and the simulated surface deformation profiles are compared to the experimental data from three subjects, as seen in Figure 3-6. There is good agreement between the simulated profiles and the experimental.

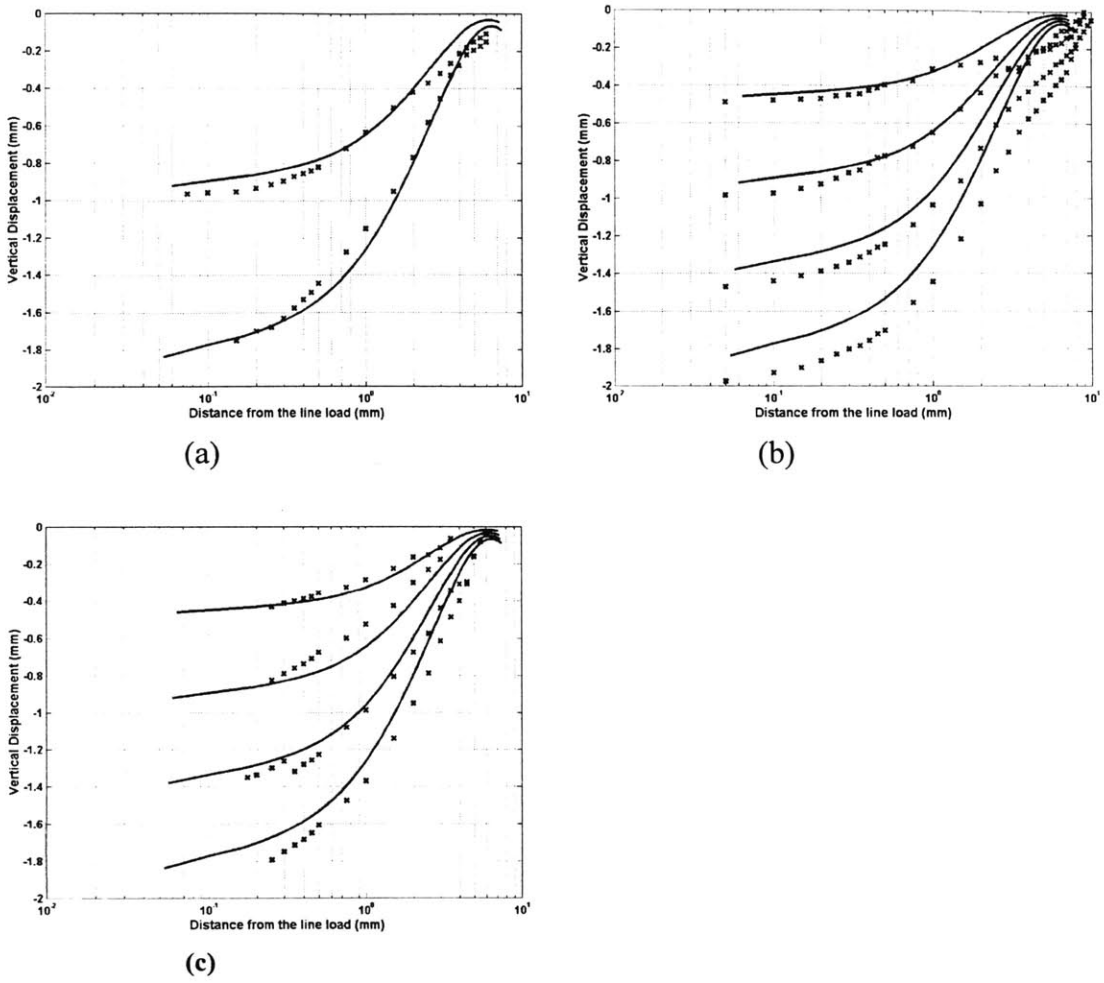

Figure 3-6. Surface deformation profiles of the model (solid line) compared to experimental data from three subjects (data points in a,b,c). The experimental data was obtained *in vivo* by indenting the finger with a line load in a steps of 0.5 mm (Srinivasan, 1989). The computed skin surface profiles under the line loads are from a FE model incorporating the 10^4:10^3:10^3:10^8 ratio of the Young's modulus for each layer.

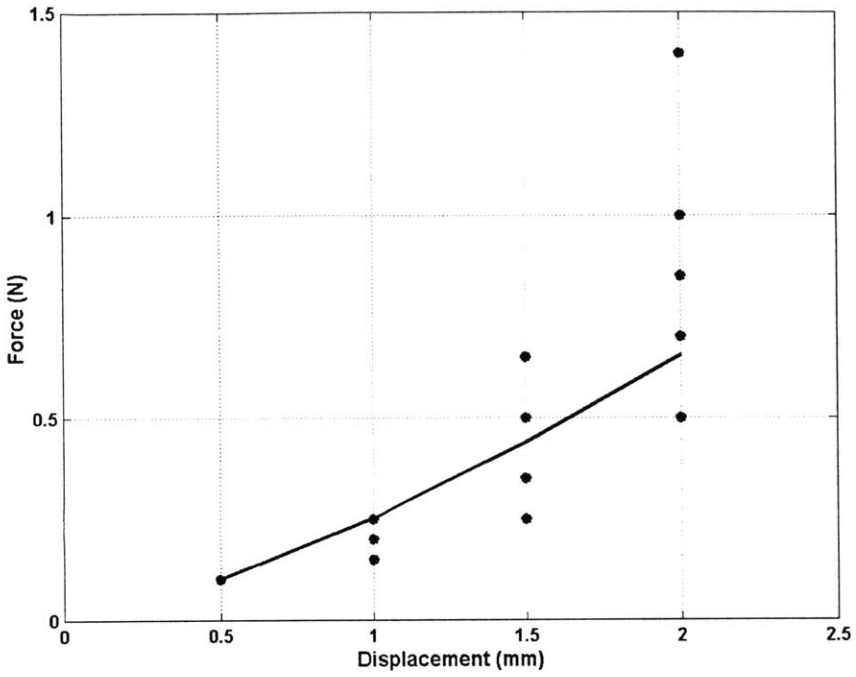

Figure 3-7. Steady state force response from the FE model (solid line) compared to experimental data from 5 subjects. A flat plate is indented into the subjects' fingerpads, to indentations depths of 0.5, 1.0, 1.5, and 2.0 mm. (Gulati and Srinivasan, 1996) At some of the depths the subjects' force response coincide, and less than five data points are seen.

Although the exact Young's modulus is not needed for stimuli prescribed in terms of displacements, many of the shaped stimuli used in the neurophysiological experiments were indented to a constant force. To simulate these experiments, an estimated value of the Young's modulus is needed. Since the 4:3:3:8 model is adopted based on precious success, only a single multiplicative constant needs to be determined. Gulati and Srinivasan indented the human fingerpad with a plate to a constant depth, and measured the force characteristics over time (Gulati and Srinivasan, 1996). The steady-state values, after the viscoelastic effects subsided, from these experiments were correlated with results obtained using the elastic finite element model (Figure 3-7). The contact mechanics involved in a plate indenting the skin surface introduces many non-linearities into the problem. From Figure 3-7 it can be seen that as the depth of indentation increases the results from each subject diverge. By correlating the experimental data with

the force response computed using the finite element model, the multiplicative constant of the Young's modulus ratio can be estimated. Using this multiplicative constant, the Young's modulus for each layer can be estimated as 0.15, 0.015, and 0.015 MPa, for the epidermis, dermis, and fat layers (the bone was made several orders of magnitude larger to approximate a rigid body). In Figure 3-7 the predicted response using the finite element model (solid line) can be seen to be in good agreement with the experimental data for small depths of indentation. At larger indentation depths the experimental data scatters, and the finite element model predicts the average response across the subjects.

De and Srinivasan (1999) formulated the viscoelasticity of the fingerpad from the force response data obtained from ramp and hold experiments using a point indenter (Gulati and Srinivasan, 1996). The viscoelastic parameters were incorporated into a finite element model of the fingerpad, and verified against experimental data for different shaped indenters (De and Srinivasan, 1999). In the formulation, the bulk modulus was assumed to be independent of time, which is a reasonable assumption for almost incompressible tissues. The modulus of rigidity, normalized with respect to its initial value, can be expressed as a Prony series:

$$g_r(t) = 1 - \sum_{1}^{2} \overline{g}_i^p (1 - e^{-t/\tau_i}) \qquad \textbf{[3-1]}$$

where $g_1^p = 0.055$, $g_2^p = 0.3691$, $\tau_1 = 3.25$, and $\tau_2 = 0.3414$.

The experiments conducted by Gulati and Srinivasan (1996) were simulated using the new FE model with the incorporation of the viscoelastic parameters formulated by De and Srinivasan. A plate was indented into the skin at a prescribed depth and velocity, and then held until steady-state was reached. Figure 3-8 shows the results from the simulation compared to the experimental data for four depths of indentation, indenting at 2 mm/sec. The force response profiles show a large variation between subjects, and the model represents an average value from all the subjects. The decay time from the peak of the force response to steady state is in good agreement between the simulated and experimental results. Therefore, the viscoelastic properties incorporated into the model are justified. Figure 3-9 shows the simulated and experimental results for different

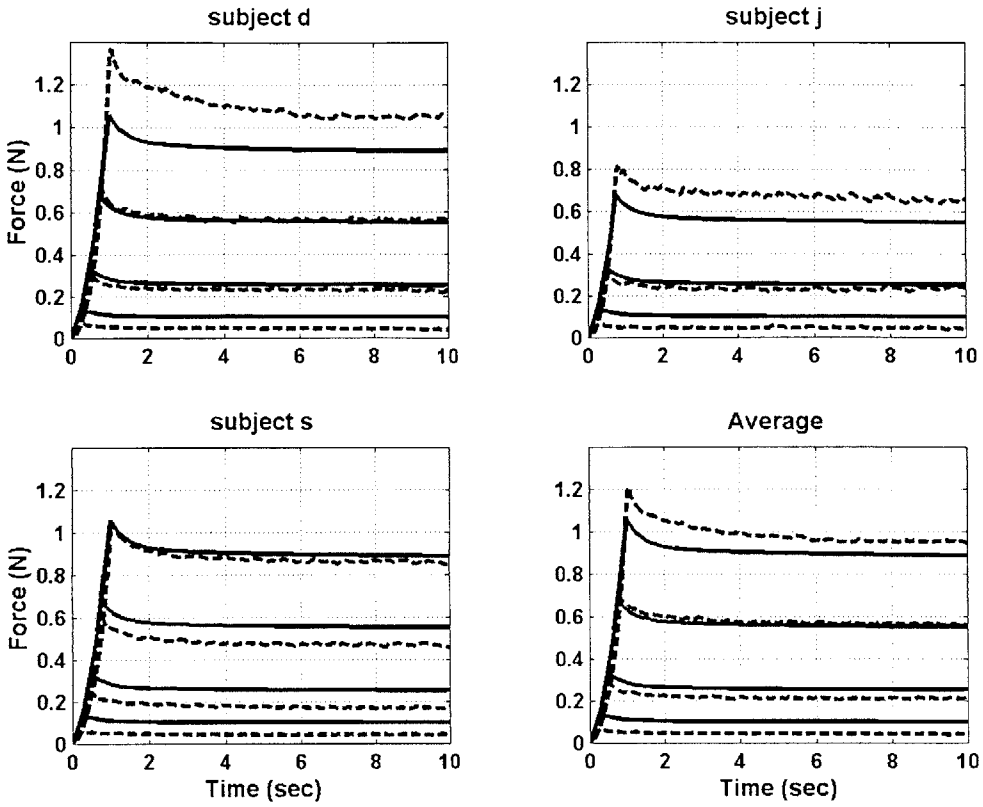

Figure 3-8 Ramp and hold force profile from the FE model (solid lines) compared to experimental data (dashed lines). A flat plate is indented into the skin at 2 mm/sec, to final depths of 0.5, 1.0, 1.5, and 2.0 mm. (Gulati and Srinivasan, 1996) The profiles from 3 subjects and the average is compared to the FE model. (Subject j only has data for depths of 0.5, 1.0, and 1.5 mm)

velocities. The force response of the model for different velocities of indentation match well the global aspects of the experimental data. A close examination of the rise and fall characteristics of the force response data reveal further non-linearities not captured in the model. Modeling these secondary effects is beyond the scope of the current research. The simplified viscoelastic parameters used in the model describe the primary time constants of the human fingerpad to sufficient accuracy.

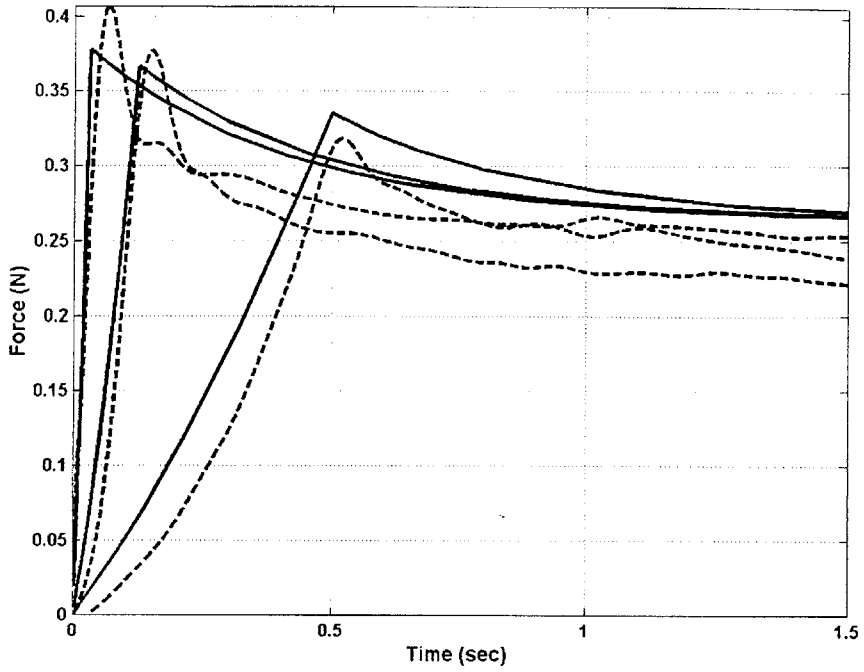

subject d

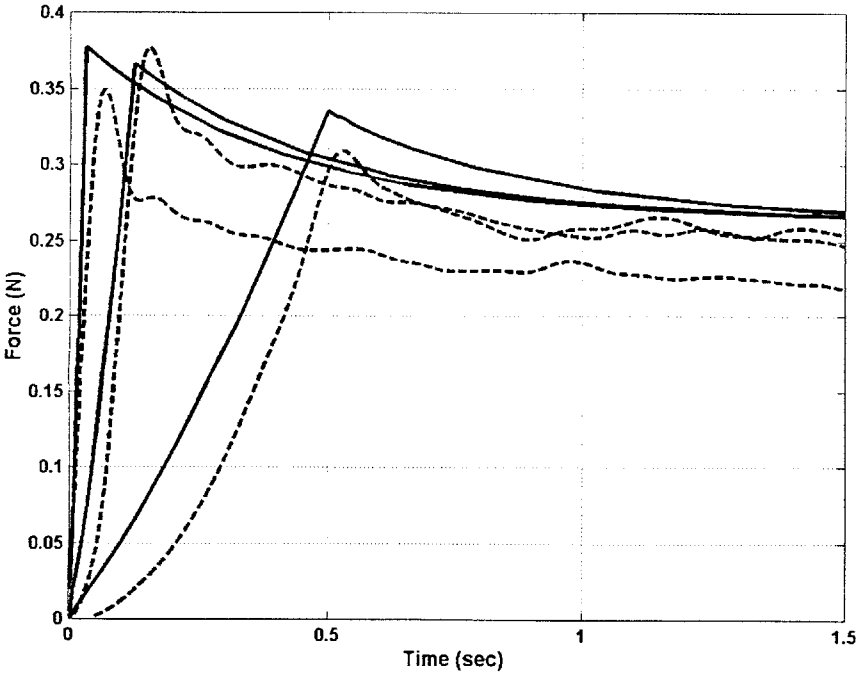

subject j

Figure 3-9. Force response of the FE model (solid lines) compared to experimental data (dashed lines) from two subjects. A flat plate is indented into the skin to a depth of 1.0 mm, using ramp velocities of 2, 8, and 32 mm/sec.

3.5 Verification using MRI

To validate the spatial response characteristics of the model, the subsurface deformation profiles simulated by the model under shaped stimuli can be compared to the corresponding images obtained through MRI. This will ultimately determine the validity of the proposed material properties. While the force response results match experimental data on a global scale, if the inner layer deformations are not accurate then the simulated strains at the mechanoreceptor locations cannot be trusted. Although determining the precise displacements of each particle in the finger is not possible from the images, the deformed shape of each tissue layer can be used to validate the spatial characteristics of the model

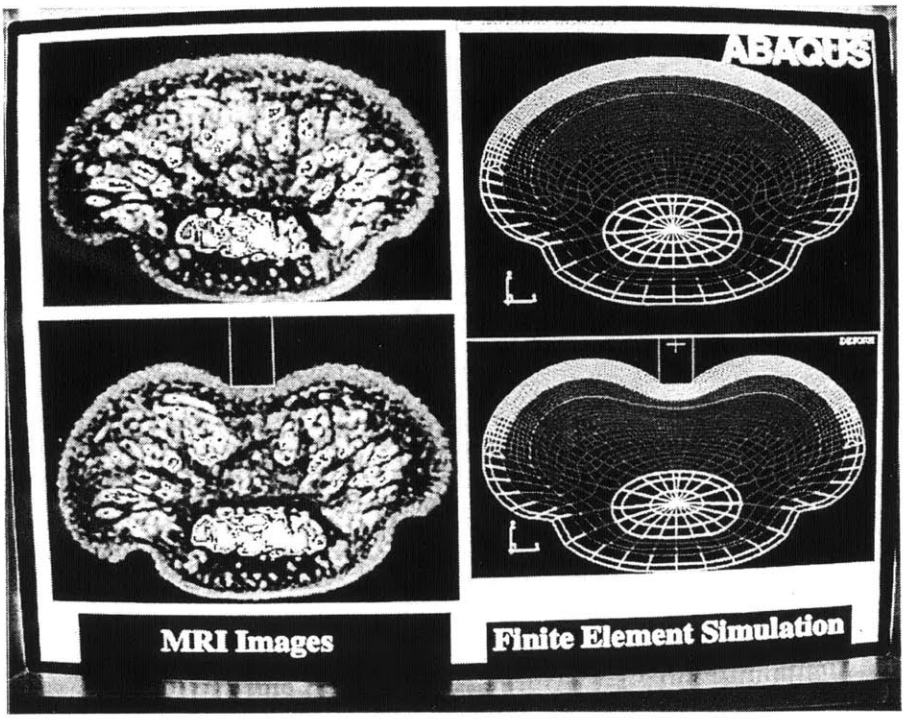

Figure 3-10. MRI deformation profiles compared to FE simulation results. The images show the undeformed MRI and FE model, and the deformation from a 1/16 inch rectangular bar indenting the finger to a depth of 2 mm. (Note: the strateum corneum layer is not shown in the MRI images, and in the FE model it is included in the outermost layer of the model)

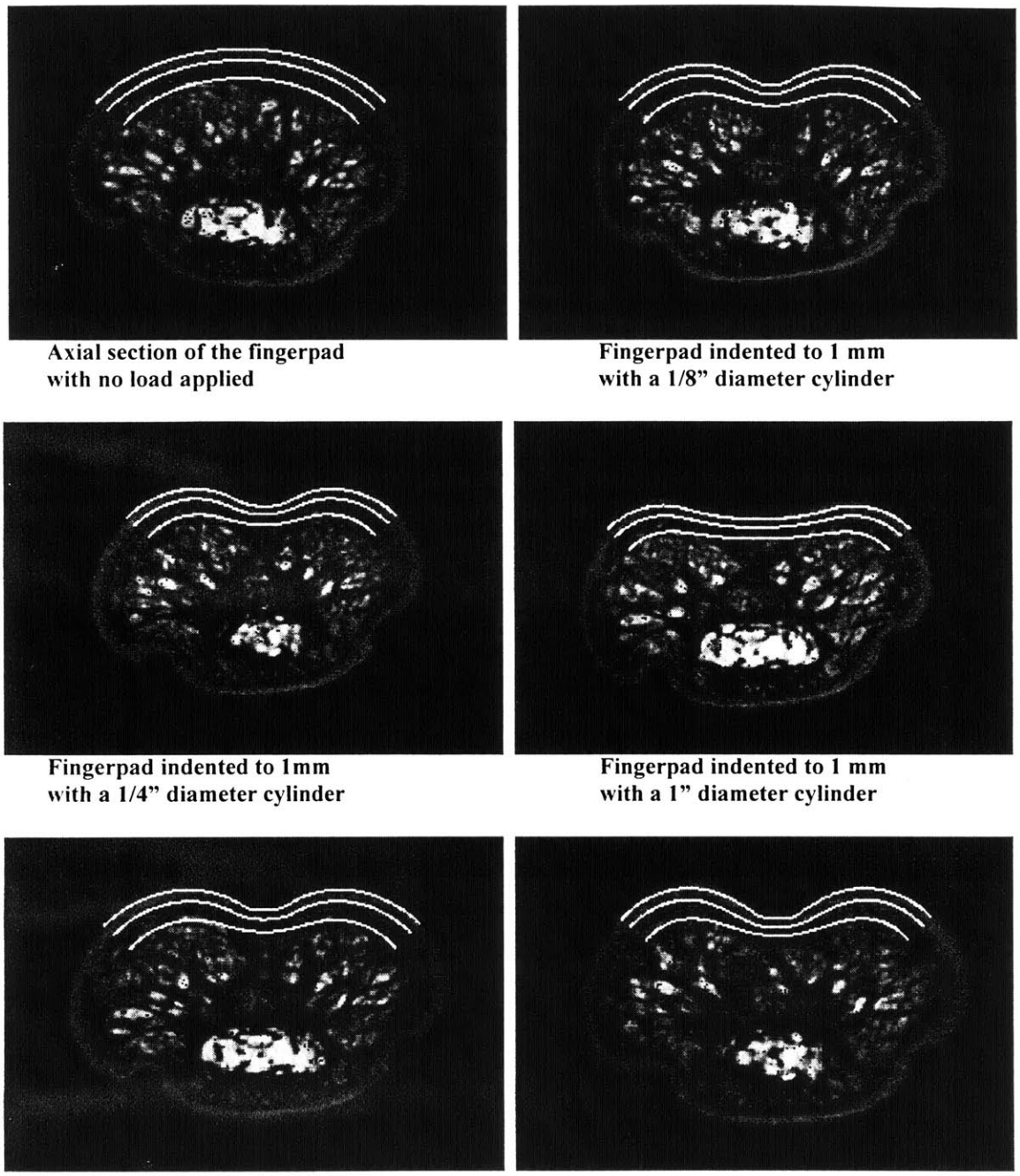

Figure 3-11. MRI images (shown in Figure 3-1), with the deformation profiles obtained from the FE simulations superimposed. The lines shown in white are the boundaries between the epidermis, dermis, and cutaneous fat layers. (The strateum corneum layer is not shown)

Figure 3-10 shows the finite element analysis results of a 1/16 inch rectangular bar indenting the finger to a depth of 2 mm, compared to the actual finger deformation. The image of the rectangular bar is superimposed on the MRI image to indicate its location, and is not a true part of the image. The *missing* outer layer of the MRI image is included in the finite element model, which is why the thickness of the epidermis layer is higher in the model. Taking this into account it can be seen that there is good agreement in the boundary deformations of the model and the experimental data. Further simulated profiles are superimposed on the experimental data in Figure 3-11. Here the deformations for the *missing* layer are not included in the FE profiles. It can be seen that the finite element model predictions are correlate well with the experimental data, further validating the model. (Note: these images are at steady-state conditions, and therefore, the viscoelastic parameters have no effect on the results)

The finite element model has been created to match the profiles of the inner layers of actual fingerpads. This model has a high mesh density in the areas of significance. The static and viscoelastic material properties have been validated, and the inner deformations correlate well with experimental results. With full confidence in the validity of the model, investigation into the mechanics of touch can be proceed.

4

Tactile Encoding of Shape during Indentation

4.1 Motivation

The determination of object shape is an essential component of tactile exploration. In order to effectively understand the world around us, we must be able to identify and discriminate shape. The fingerpad is the primary tool for this task. When an object is pressed onto the fingerpad, only features within the contact region can be transferred to the mechanoreceptors located beneath the skin surface. This region of skin can be viewed as a black box system that passes an encoded tactile image of the object to the brain, where shape deciphering occurs. The tactile image is encoded by a series of neural impulses. These impulses are all of the same magnitude, and therefore, all information is represented in the time interval between impulses, which can also be measured in terms of the neural discharge frequency.

When discussing the shape of an object, a frame of reference must be determined in order for shape to have any meaning (Figure 4-1). One representation could be the cartesian or polar coordinates of each point of the surface of the object. Another could measure the slope at the point of contact on the surface. If the object were rotated, then both of these representations would be altered, because they depend on a coordinate reference. In haptic exploration, however, the shape of an object does not depend on its absolute location. In other words, a coffee cup feels the same irrespective of how we touch it. Curvature is one feature which is invariant to rotation or translation (Gauss, 1827). From differential geometry it is known that the local curvature of each point along a surface describes that surface uniquely. For this reason, the local curvature of an object in the

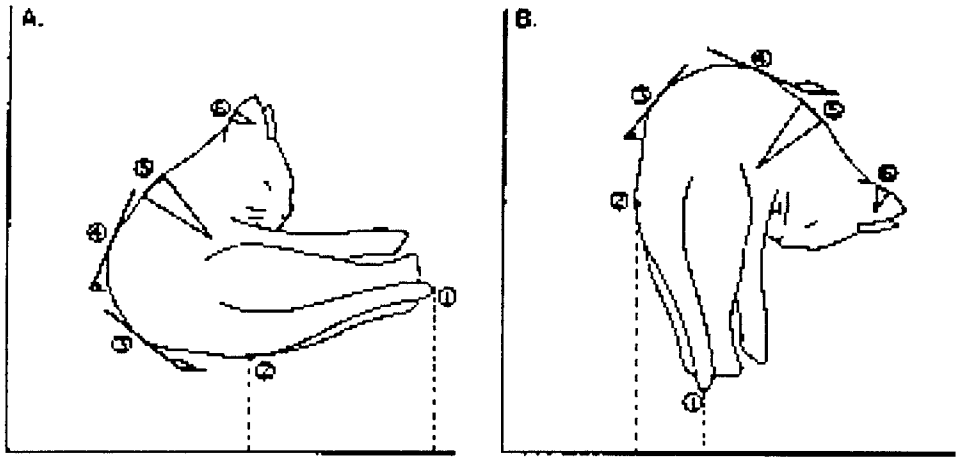

Figure 4–1. Representation of object geometry: cartesian coordinates of points 1 and 2; slope of the tangent at points 3 and 4; local curvature of points 5 and 6. Figure B is the object in figure A rotated by 90 degrees (adapted from Srinivasan and LaMotte, 1991).

region of contact is taken as the relevant feature to tactile encoding. Neurophysiological experiments support this hypothesis. (Srinivasan and LaMotte, 1991)

4.2 Neurophysiological Recordings

Srinivasan and LaMotte (1991) performed neurophysiological experiments on the passive monkey fingerpad, in order to understand shape encoding. Cylindrical bars of various curvatures and a flat plate were indented into the fingerpad, and the neural impulses were recorded for various SA and RA type mechanoreceptors. The center of the indention field was placed in the Most Sensitive Spot (MSS) of each receptor. An electromechanical stimulator was used to vertically indent the curved surfaces through constant force ramp, and then maintain the surfaces at a constant force during the hold phase.

The actual neurophysiological data used in this thesis research came from earlier experiments by Srinivasan and LaMotte (1991), in which a constant force of 20g, a ramp time of 0.5 sec., and a hold time of 2 sec. was employed. 9 surfaces of varying curvature were used as stimuli. Figure 4-2 shows the neural response from one SA fiber, where

each tick mark represents a neural impulse. Some observations about the SA response mechanism can be made from this data. (1) As the surface curvature increases the discharge rate increases, both during the ramp phase and the hold phase. (2) The impulse frequency increases rapidly during the ramp phase, peaks at the top of the ramp, and then decays during the hold phase. (3) There is a delay between the start of the ramp and the first neural impulse recorded. From these observations, the following hypothesis can be made on the firing mechanism of the SA mechanoreceptors. The neural impulse rate is a function of the surface curvature, the vertical indention depth, and the velocity of indentation. There is also a settling (adaptation) mechanism, either mechanical or electrophysiological, that causes the impulse rate to decay for a constant force. Finally, for each stimulus parameter there is a threshold which must be crossed before an impulse can fire.

From the RAs recorded, impulses were fired only during the beginning of the ramp phase or not at all. None were sensitive to variations in surface curvature. This supports the hypothesis that the RA firing mechanism is responsive to the rate of change of curvature, since the skin surface curvature rate is only nonzero at the beginning of the indention when the skin conforms to the indentation surface (Srinivasan and LaMotte, 1991).

Using SA neural impulse response data, the instantaneous frequency was computed. Figure-4-3 shows the neural frequency ramp and hold response from the flat plate and 8 cylinders indenting the skin. The neural response during both the ramp phase and the hold phase increases as the surface curvature increases.

The steady state neural response is linearly related to the peak neural response at the top of the ramp (Figure-4-4). The implication is that during the hold phase, the adapting mechanism, whether it be mechanical or electrophysiological, is the same for all curvatures. If a function of the characteristics of the indenting surface can model the peak neural response, then this function can also model the steady state response and possibly the entire neural response mechanism.

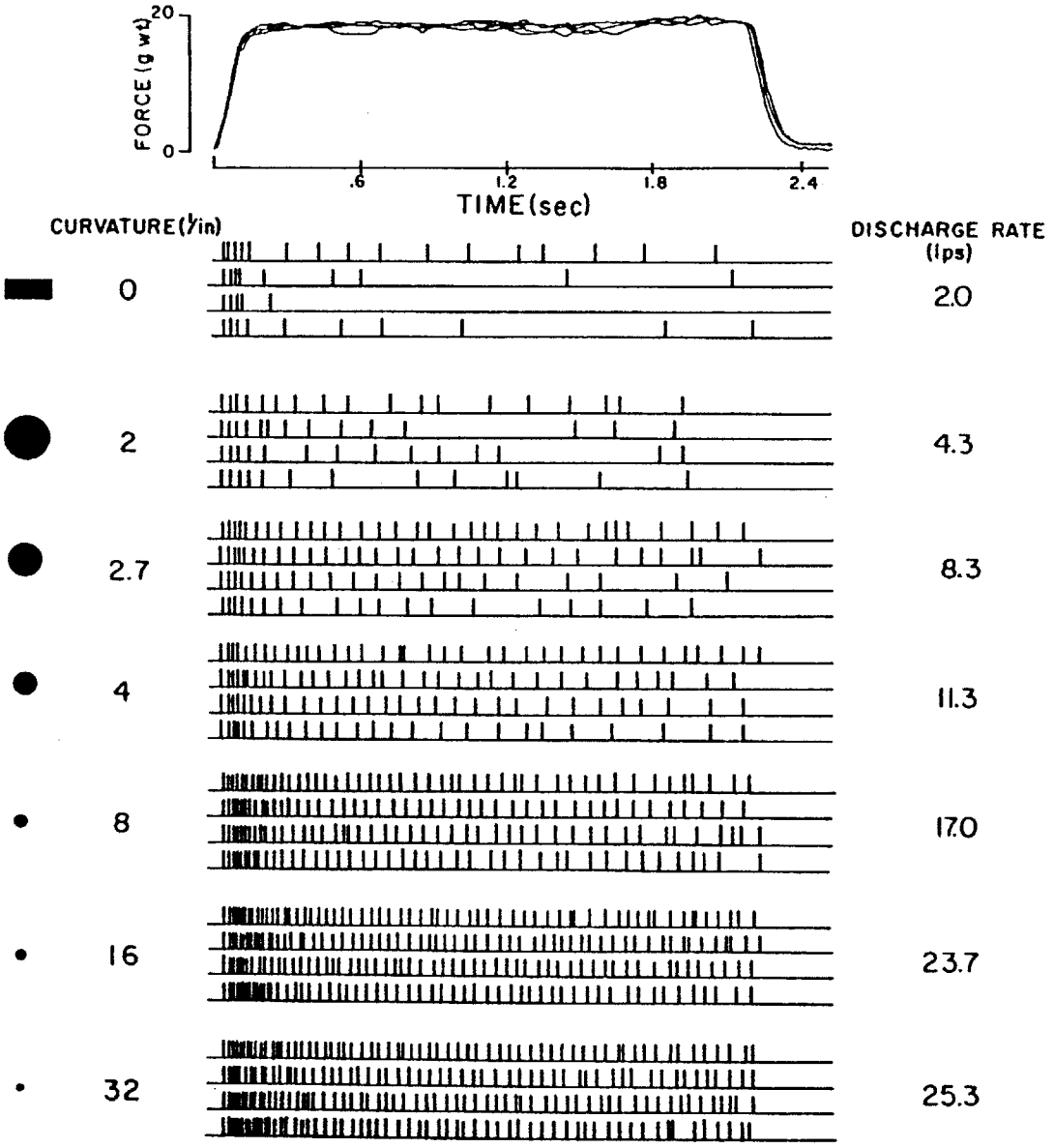

Figure 4-2. SA Neural impulse response from ramp and hold indentations of the MSS by surfaces of various curvature. The stimulus force trace is shown at the top. The curvature of each surface is on the left. Four trials for each surface are shown. Each tick mark represents one neural impulse, and the average neural impulse response during the hold phase is shown on the left. Force control using 150 g wt/sec ramp, 20g wt steady force for 2 sec. (adapted from Srinivasan and LaMotte, 1991).

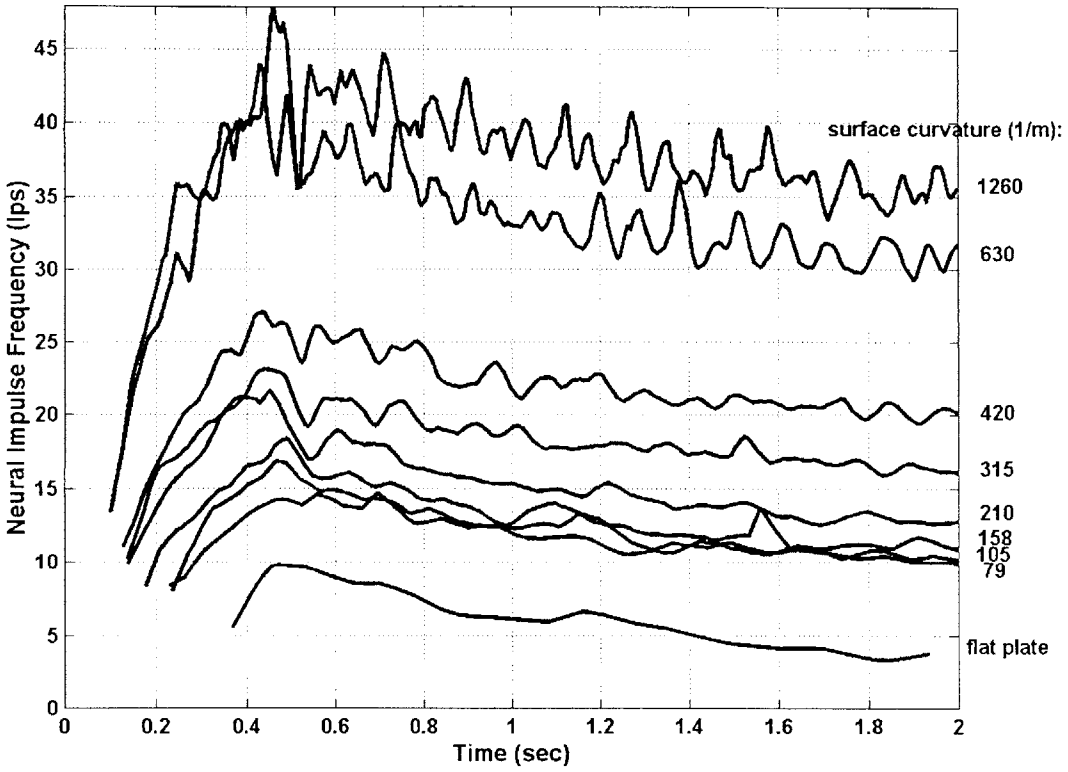

Figure 4-3. Instantaneous neural impulse frequency computed from the SA neural recordings during ramp and hold experiments (40 g wt/sec ramp, 20g wt steady force for 2 sec).

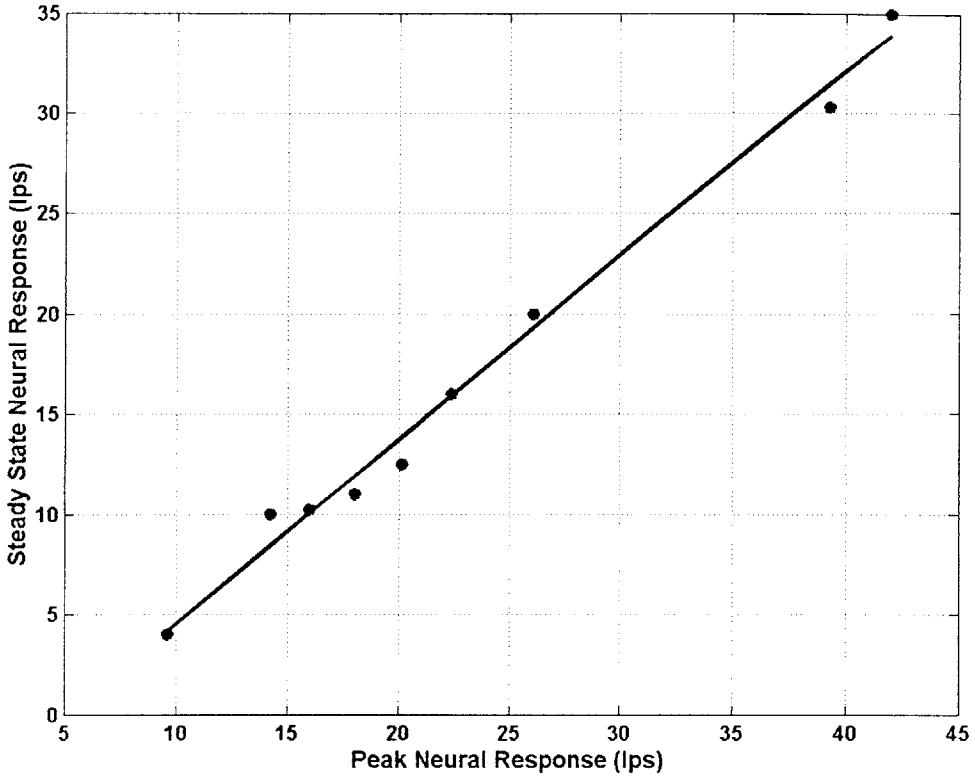

Figure 4-4. Peak neural response versus steady state neural response from ramp and hold neurophysiological experiments. A flat plate and 8 curved surfaces of varying curvature were used as stimuli.

Surface curvature has been shown to be a contributing factor in the steady state neural response (Srinivasan and LaMotte, 1991). Figure 4-5 is a plot of the surface curvature versus the peak neural response and the steady state response. The neural responses increase approximately linearly with curvature, and then the response saturates for the highest curvature. Even when the highest curvature is included, the linear fit does not deviate too much from the data points.

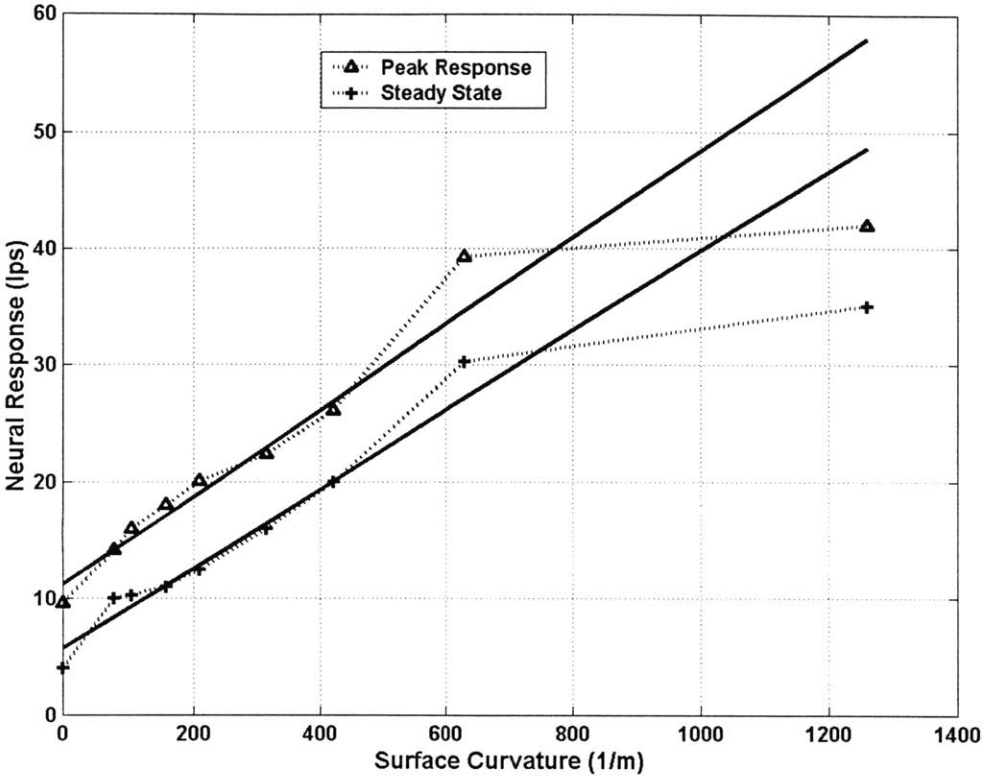

Figure 4-5. Peak and steady state neural response for the ramp and hold experiments using a flat plate and surfaces of varying curvature (dotted lines). The solid lines are a linear fit between curvature and neural response. Note that the linear fit would have been even better if the response by the highest curvature was not included.

4.3 Biomechanical Simulations

The biomechanics of the fingerpad cannot be accurately and completely measured during indentation experiments. The global displacement and force of the indenting surface can be reliably measured, but the local displacement and pressure across the contact region cannot be measured at a fine enough scale. No technique is currently available to determine the stresses and strains at mechanoreceptor depths below the skin surface. Therefore, simulations must be performed to determine the relevant forces, stresses, and strains at locations of interest. The finite element technique provides an accurate method

of calculating the mechanical state of the finger over time during indention. Previous work has shown that the modeling the fingerpad using this technique provides useful results (Dandekar and Srinivasan, 1996; Raju and Srinivasan, 1999). The previous models, however, did not accurately model the inner layers of the fingerpad, which is vital to understanding the mechanics at the receptor level. These models also were comprised of only elastic layers; viscoelasticity was not incorporated, and therefore, the time evolution of the indentation could not be studied. The two dimensional finite element model created for this project incorporates the internal geometry of the fingerpad, and models the inherent viscoelasticity. The model was verified by comparing the prediction with experimental deformation and force response data, and therefore can be used as an accurate model of the biomechanics during touch.

The ramp and hold simulations were performed using the same criteria as in the neurophysiological experiments (40 g/s ramp; and 20 g steady force for 2 s). The model is a two-dimensional cross section of the fingerpad. The indenters can be assumed to be infinitely long, and therefore, plane strain conditions hold. A flat plate and 8 curved surfaces (Curvatures, K: 79, 105, 158, 210, 315, 420, 630, and 1260 (m^{-1}).) were used as the stimuli. Figure 4-6 shows the surface deformation profiles of the 9 simulations at the peak of the ramp and at the end of the hold phase. Figure 4-7 shows the displacement of the indented surface for the ramp and hold simulations. As can be seen, as the curvature increases, the depth of indention increases as well. This makes intuitive sense, because as the curve becomes flatter the area of the contact region with the skin increases. This enables more points on the skin surface to provide a resisting force to the indenting surface. Each point on the skin exerts a smaller force than if the contact region were smaller, and therefore, the corresponding vertical displacement need not be as large.

The instantaneous frequency of the SA neural impulse recordings is shown in Figure 4-3 for the ramp and hold experiments. Comparing the displacement profiles to the SA neural recordings, the following initial observations are supported. The impulse frequency is a function of indentation depth. The impulse rate during the ramp phase is greater than that predicted by the depth of indentation alone. Although the velocity of

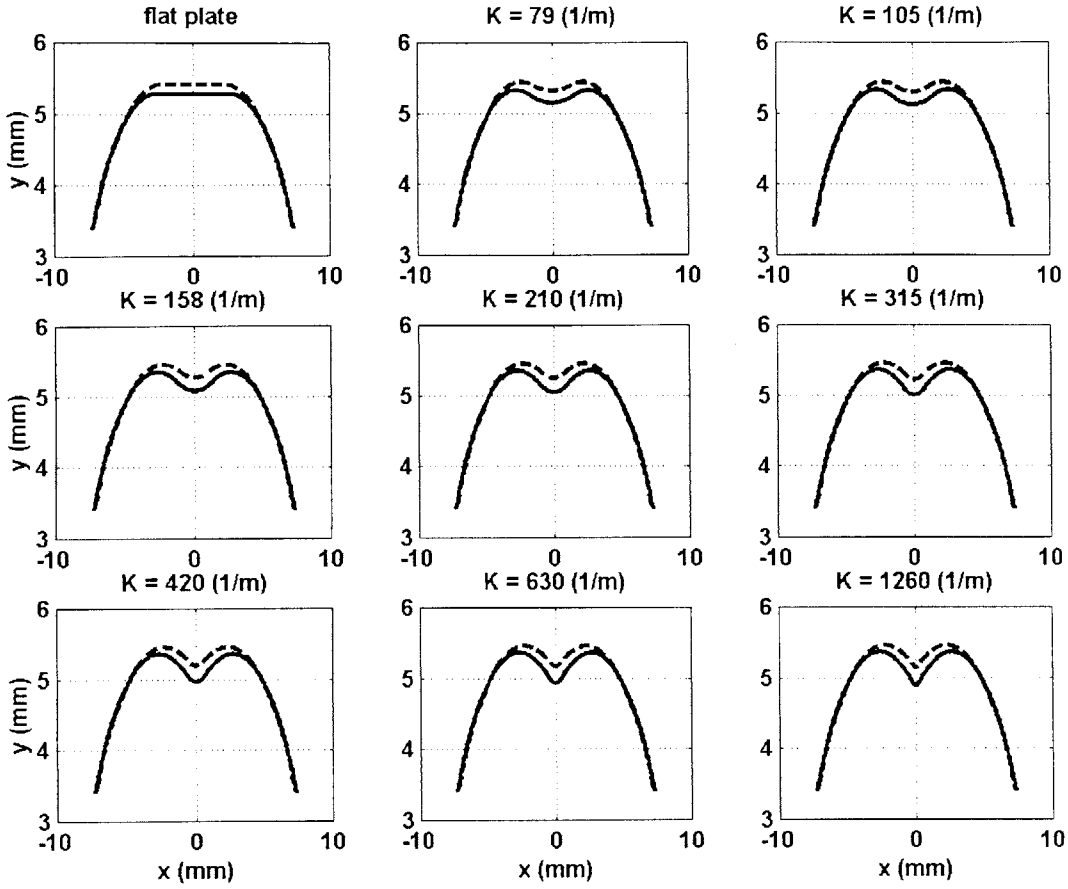

Figure 4-6. Surface deformation profile for the nine indenting surfaces. Dashed lines represent profile at the top of the ramp phase, and the solid lines are the steady state profiles.

indentation is a plausible candidate stimulus for the response during the ramp phase, during the hold phase, the impulse rate decays while the depth of indention continues to increase slowly. Therefore, another adaptation mechanism must be responsible for the neural firing over time.

As the curvature of the indenting surface increases, the size of the contact region decreases (Figure 4-8). The surface indents the skin and the contact region grows rapidly during the ramp phase, and then slowly expands in the hold phase. The neural response decreases during the ramp phase, and a relationship between the contact width

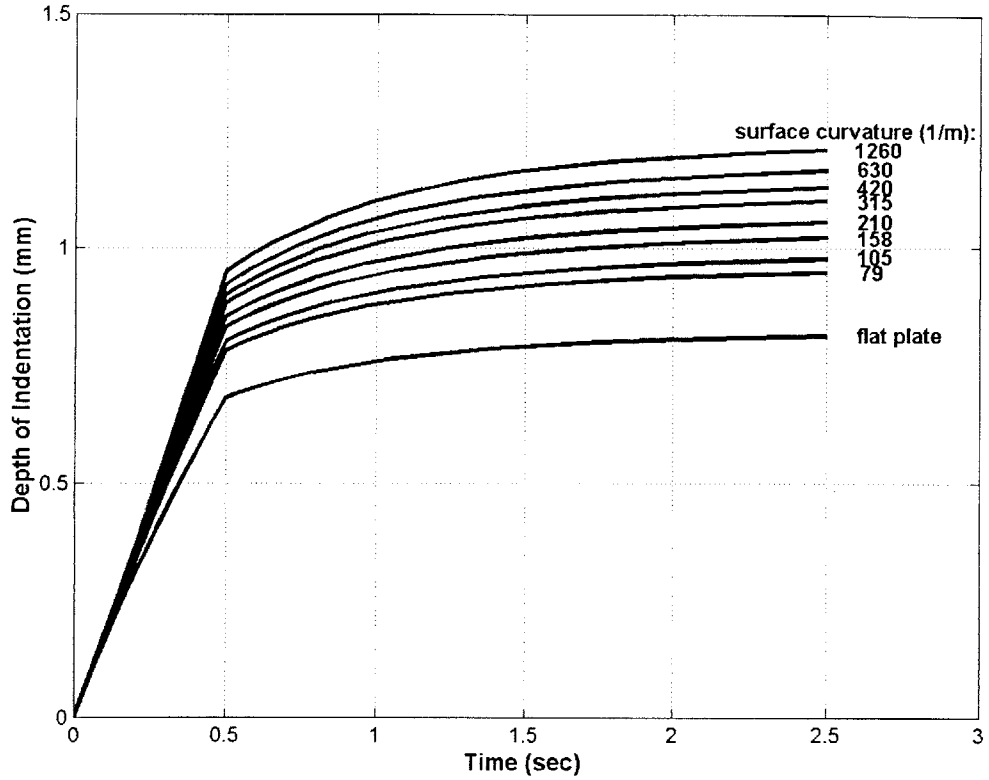

Figure 4-7. Depth of indentation of the flat plate and curved surfaces during the ramp and hold simulations.

expansion and the neural frequency decay can be inferred. Figure 4–9 is a plot of the neural frequency response versus the inverse of the contact width, during the hold phase. A linear relationship is evident for the surfaces with small curvature. The contact region is only measured over discrete points in the simulations, and in order for the increase in contact region to be measurable another node on the finger model must come in contact with the surface. For the surface with the highest curvature, K = 1260 m^{-1}, the finite element spatial resolution is not fine enough to resolve the entire contact profile, and hence, the linear relationship can only be hypothesized.

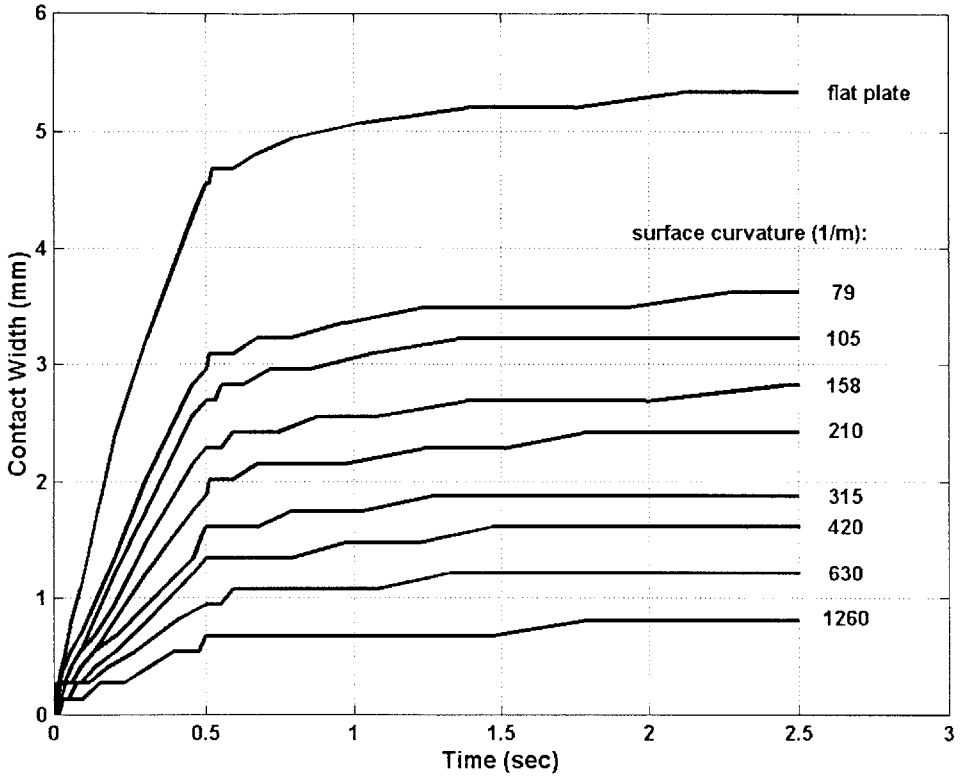

Figure 4-8. Width of the contact region during the ramp and hold simulations of the flat plate and curved surfaces.

For a surface of given curvature, the SA neural firing mechanism during ramp and hold can now be understood to have two components. As the surface indents the skin, the neural impulse frequency increases rapidly in response to the rapid increase in depth of indentation. The velocity of indentation influences the impulse frequency. During the hold phase, the skin begins to relax, and the area of the contact region spreads, and the neural impulse frequency decays to its steady state value.

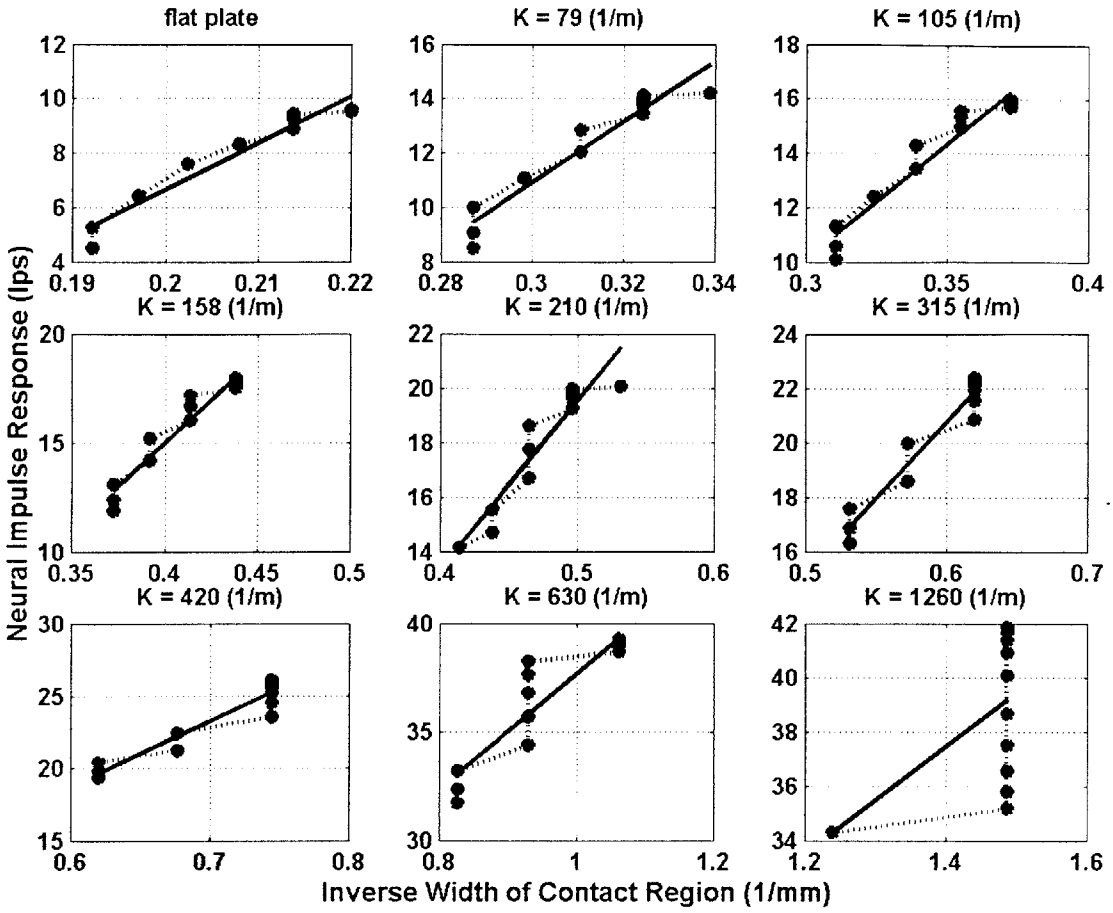

Figure 4-9. SA neural impulse response versus the inverse width of the contact region during the constant force hold phase. A flat plate and 8 curved surfaces were used as stimuli.

4.4 Contact Pressure

The fingerpad can be viewed as a black box where, as a surface indents, complex mechanical filtering occurs, and the SAs process this data and emit the neural impulses. The input to this system is the pressure on the skin within the contact region. Understanding the contact pressure during touch is essential to understanding the neural firing mechanism. Figure 4-10 shows the contact pressure at the center node over time for the different contact surfaces. During the ramp phase, the pressure increases to a

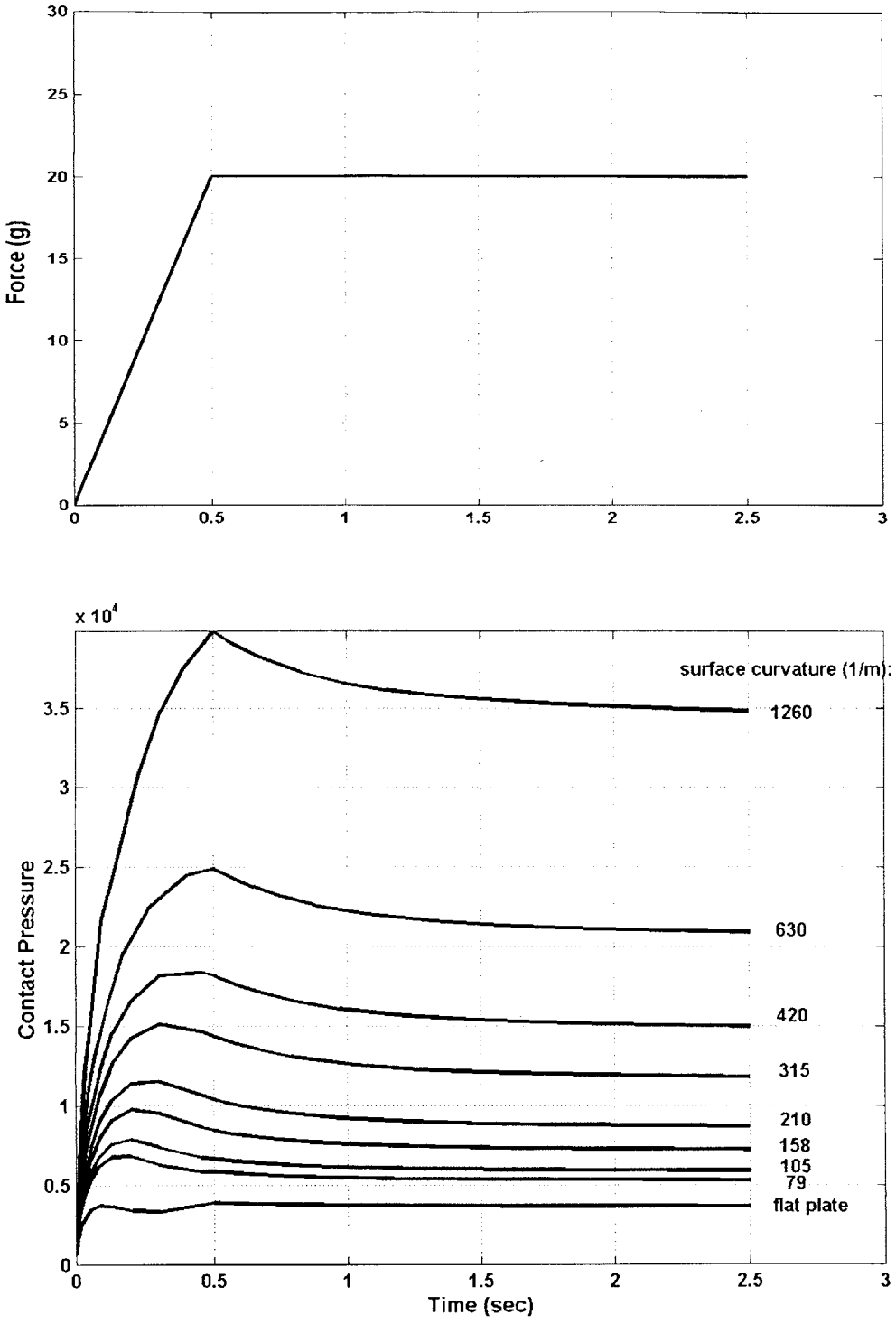

Figure 4-10. Contact pressure at the center of the fingerpad over time, during the ramp and hold simulations of the flat plate and curved surfaces. The top trace is the indentation force, showing the ramp phase and hold phase of the indentation simulation.

peak, and then decays to a steady state value during the hold phase. Although this is true for all the curved surfaces, the contact pressure from the flat plate behaves differently: there is a first peak, followed by a dip and a second peak at the end of the ramp, and then decay occurs. Except for the two highest curvatures, the contact pressure peak, however, does not fall at the peak of the ramp phase; it occurs some time during the ramp depending on the surface curvature. The peaks occur sooner for surfaces with smaller curvatures. By examining the spatial distributions of contact pressure over time, the peak shift can be explained (Figure 4-11). As the surface indents the skin, at first only a small region of the skin is in contact with the surface, and the pressure on each point increases as the force ramps. During this time, the width of the contact region increases, and the indention force spreads over more points. At some point the contact region expansion has a greater effect than the increase in overall force due to the ramp, and the pressure at the center node begins to decay. During the hold phase, the pressure decay continues. The contact region for the broader curves spreads out faster, and hence the peak in the contact pressure occurs sooner. For the sharpest curve ($K = 1260\ m^{-1}$), the spreading never dominates and subsequently the contact pressure does not begin to decay until the hold phase. It should be noted that the model was intentionally made symmetrical and the center of the surface indents vertically on the center of the fingerpad; therefore, the contact pressure distribution is symmetrical as seen in the profiles.

The peculiar shape of the contact pressure profile is due to the multiple material layers composing the fingerpad. Figure-4-12 shows the contact pressure distribution for a flat plate indenting the multiple layer fingerpad model, and a model comprised of only one homogeneous material. For the same indentation depth and contact area, the contact pressure profiles are vastly different. The homogeneous model displays none of the peak pressure spreading phenomena that occurs in the multi-layered model.

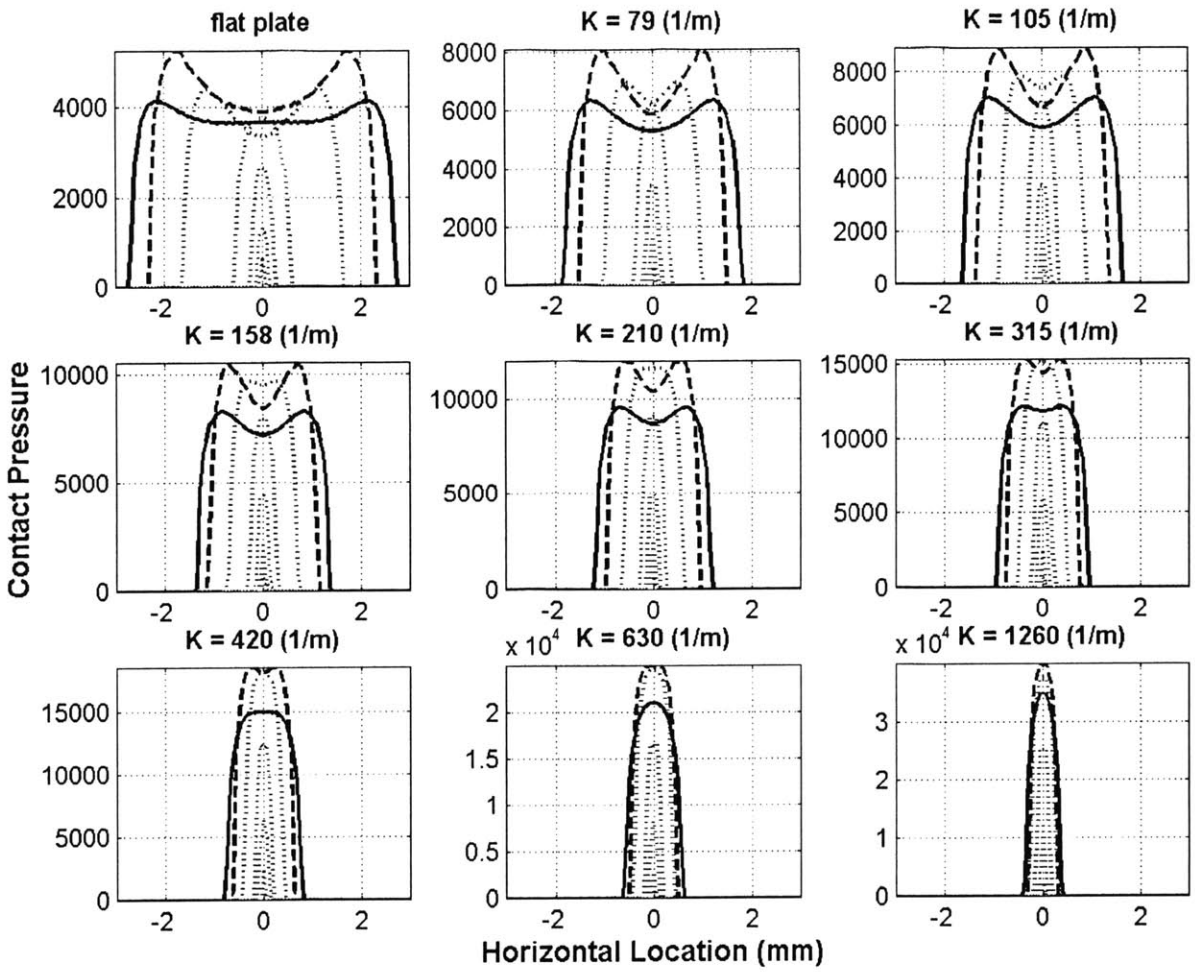

Figure 4-11. Spatial distribution of contact pressure for the ramp and hold simulations. Illustrating the contact pressure profile during the ramp phase (dotted line plots), the peak of the ramp (thick dashed line), and at steady state (solid line).

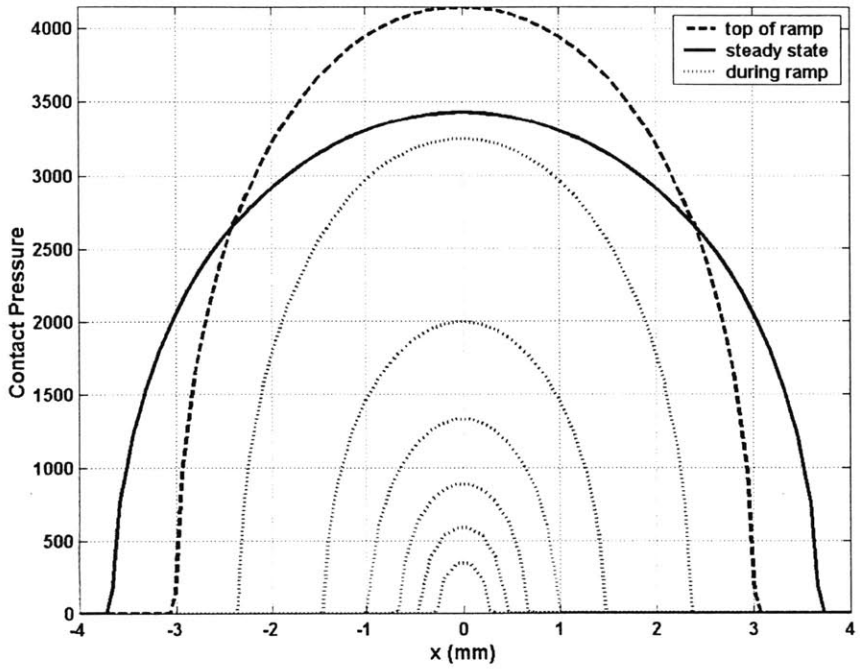

(a)

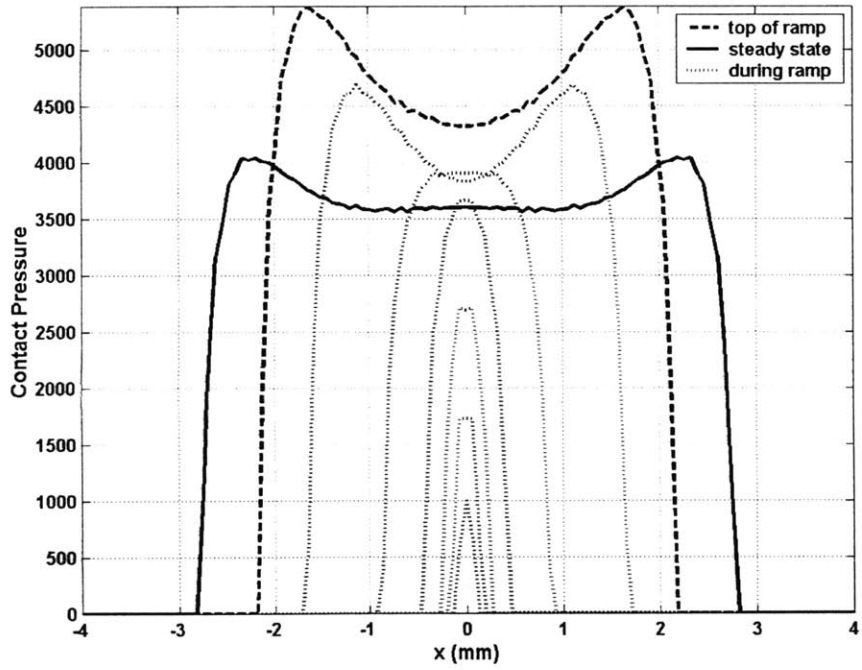

(b)

Figure 4-12. Spatial distribution of contact pressure for the ramp and hold simulations with a flat plate indenter. (a) using homogeneous model; (b) using layered model developed from MRI images.

By comparing the displacement profiles in Fig 4-7 with the contact pressure profiles in Fig 4-10 is can be seen that as the contacting surface indents the finger, initially the contact pressure increases as a function of indentation depth and indentation velocity. As the indentation increases further, a point is reached where the contact pressure decreases for higher indentation depths. Figure 4-13 shows traces of the contact pressure versus depth of indentation for every point in the contact region for several depths of indentation by each stimulus shape. The contact pressure during the beginning of the indentation ramp is linearly related (almost vertical in the figure) to the vertical displacement, but is offset by the displacement of the node at the edge of the contact region.

From Figure 4-11 it is evident that the contact pressure peak does not occur always at the center node. When the size of the contact region is small, the peak is in the center, but as the contact area expands the peak moves away from the center and closer to the edges of the contact region. This occurs symmetrically of course, with two equal peaks at the same distance from the center. For the sharpest curvature, the width of the contact region never exceeds the critical value, and subsequently, the peak always remains at the center node.

Figure 4-14 is a plot of the contact pressure spatial distribution over time, for the K = 210 m^{-1} indenting the skin surface. Due to symmetry, only half of the distribution is shown. As the surface indents the skin, the contact region increases, and the contact pressure at all points increases, while the peak of the contact pressure is at the center node. As the contact region expands, a critical width is reached, at which point the peak shifts away from the center. The contact region continues to increase and the peak pressure shifts further away from the center node, and the pressure at points near the center decreases. Figure 4-15 compares the contact pressure at the center node, to the maximum contact pressure across the surface. Both curves exhibit the same decay properties, only the time and magnitude of the pressure peak differs. Examining the pressure profiles for each point in the contacting region, similar features can be extracted (Figure 4-16). Once a node comes in contact with the surface, the contact pressure increases rapidly to a peak as a function of the local displacement, and then decays

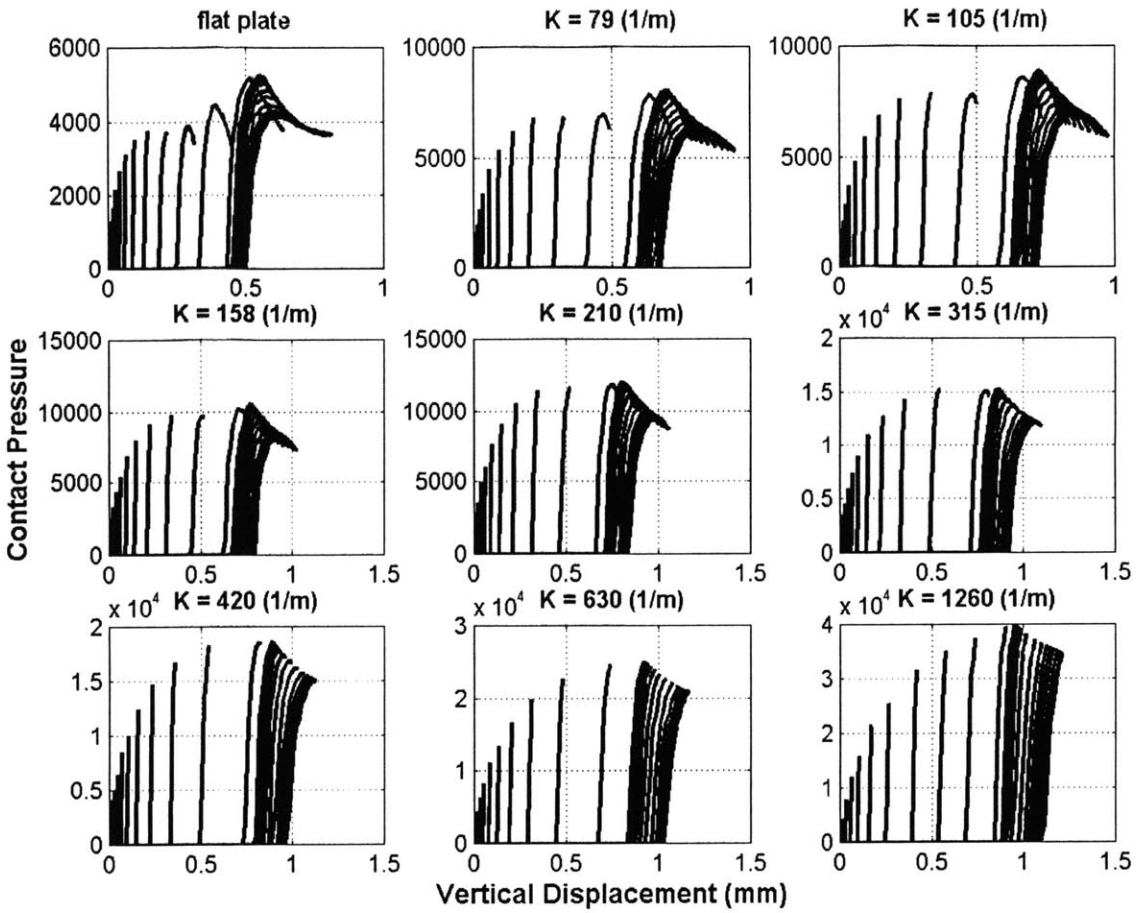

Figure 4-13. Contact pressure versus vertical displacement for each node in the contact region, for all time during the ramp and hold simulations. Each trace represents, for a given depth of indentation, the pressure distribution within the contact region as a function of vertical displacement of the corresponding point within the contact region. A flat plate and eight surfaces of varying curvature were used as stimuli.

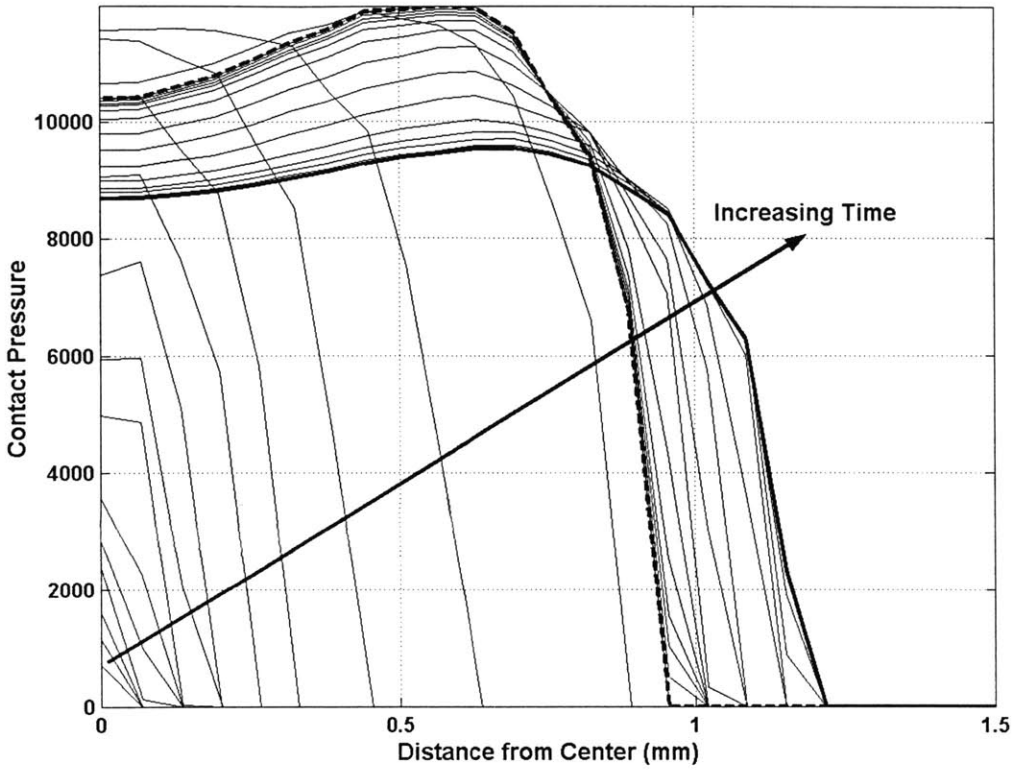

Figure 4-14. Spatial distribution of contact pressure over time for a surface with a curvature of 210 m^{-1}. (40 g wt/sec ramp, 20g wt steady force for 2 sec) dashed line: profile at top of ramp, solid line: steady state profile. Due to symmetry only half of the profile is shown.

slowly. The time constant of the decay profile is the same for each point on the surface. The peak for each profile occurs at a critical distance from the edge of the contact region (about 0.5 mm in Fig. 4-14). This distance is the same for each point on the contacting surface. At each node, the contact pressure increases until the critical distance is reached, after which the pressure decays as a function of the distance between the node and the edge of the contacting region.

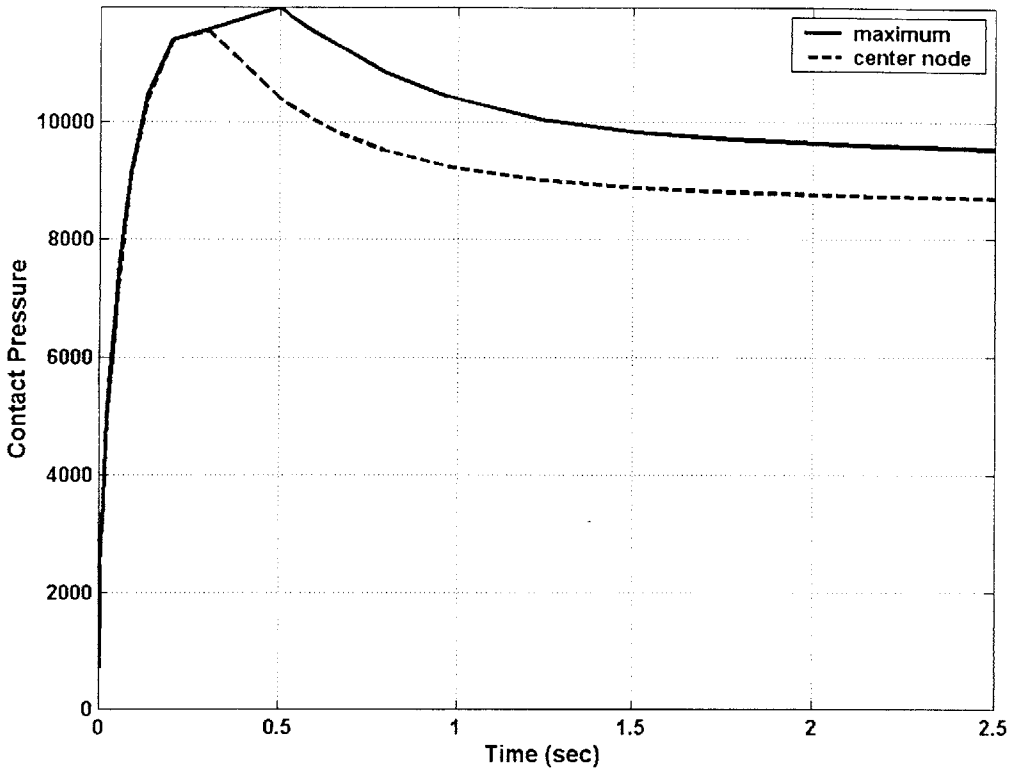

Figure 4-15. Maximum contact pressure (solid line) and contact pressure at the center of the fingerpad (dashed line) during a ramp and hold simulation with a surface of curvature of 210 m^{-1}. (40 g wt/sec ramp, 20g wt steady force for 2 sec)

For the curvature, K = 210 m^{-1}, the following relationship holds for the contact pressure decay across the contact region

$$p(x) = A1*(x_{edge} - x)^{-1} + A2*(d(x) - d_0) + A3 \qquad [4\text{-}1]$$

Where $p(x)$ is the contact pressure at each point, $d(x)$ is the local displacement, d_0 is the threshold displacement defined as the displacement at the edge of the contact region, and x_{edge} is half the contact width. Figure 4-17 shows the contact pressure decay, predicted using Eq. 4-1 for 12 points across the contact region.

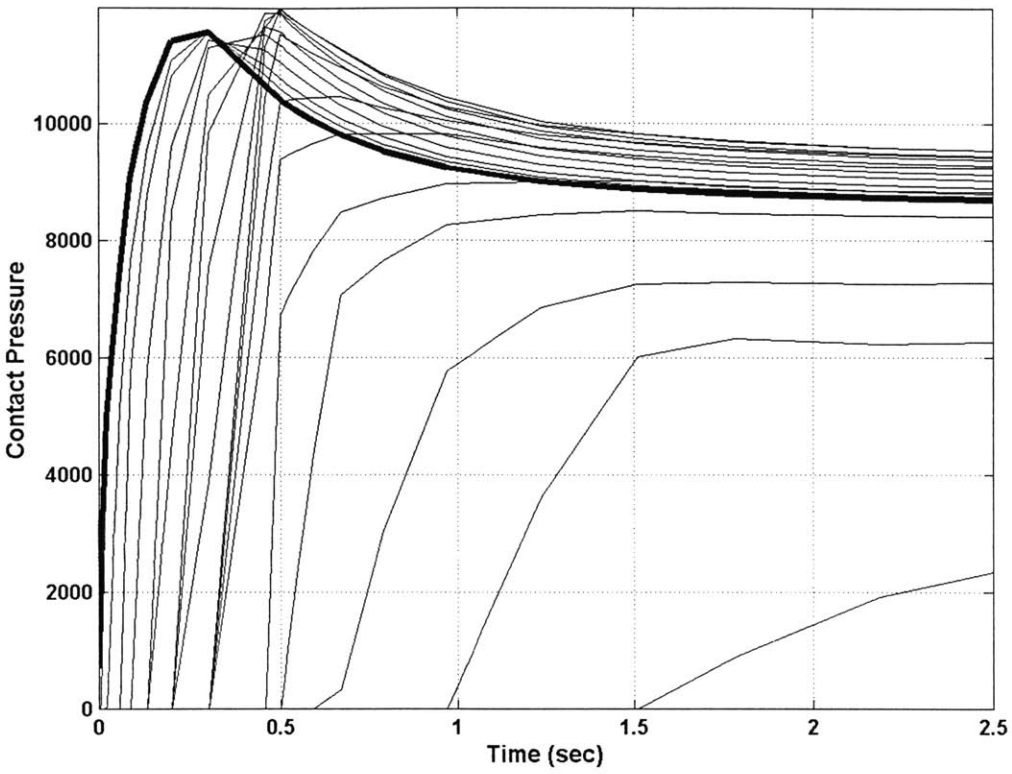

Figure 4-16. Contact pressure over time for each point in the contact region is shown as a trace, during a ramp and hold simulation with a surface of curvature of 210 m^{-1} (40 g wt/sec ramp, 20g wt steady force for 2 sec). As time increases, the contact region expands and more nodes come in contact with the surface. Solid line is the contact pressure at the center of the fingerpad.

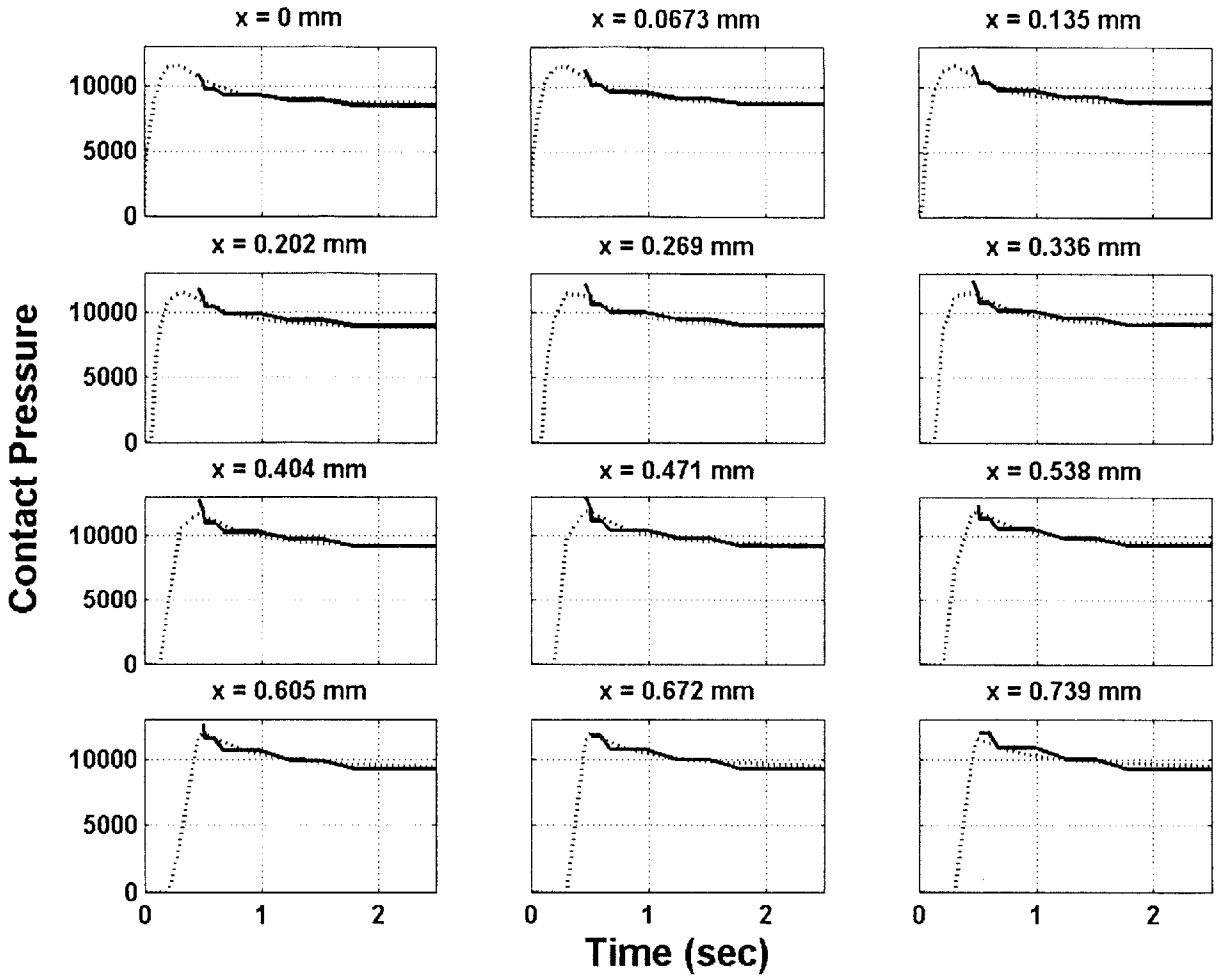

Figure 4-17. Contact pressure (dotted lines) during ramp and hold simulation with a surface of curvature 210 m^{-1} (40 g wt/sec ramp, 20g wt steady force for 2 sec). Profiles are shown for 12 points across the contact region. The solid line is the predicted decay of the contact pressure using Eq. 4-1 in the text.

The complete contact pressure profile during the ramp and hold simulations can be described by the depth of indentation and the width of the contact region. As the surface indents the fingerpad, the pressure increases at each point as the total force applied is increasing. This pressure is proportional to the local relative displacement and the surface curvature at each point. Because the displacement is increasing with a high velocity, the nodal pressure is also increasing rapidly. Once the critical distance from the edge is surpassed the local pressure decays. During the ramp phase, the peak of the contact pressure increases, and moves further away from the center node. During the hold phase, the peak continues to move further from the center node. Because the applied force is held at a constant, the velocity of indentation is much less and the contact width spreading dominates; subsequently, the contact pressure at almost every point except near the contact boundary decreases. The contact region continues to increase during the hold phase, and new points come in contact with the surface. The rise time and peak of the contact pressure decreases for each new node in the contact region, due to the decrease in the velocity of indentation (Fig. 4-16).

A relationship between the contact parameters can be developed to explain the contact pressure profile of each point, for the ramp and hold simulations, by extending the previous argument to surfaces of variable curvature. During the ramp phase, as the total force is increasing

$$p(x) = A1*(d(x) - d_0) + A2*V_y(x) + A3*K + A4 \qquad [4\text{-}2]$$

Where $p(x)$ is the contact pressure at each point, $d(x)$ is the local displacement, $V_y(x)$ is the local velocity of indentation, d_0 is the threshold displacement defined as the displacement at the edge of the contact region, and K is the surface curvature. Once each point is sufficiently far from the edge of the contact region, or the total force is held constant, the local pressure decays proportional to the inverse of the contact width.

During the hold phase, the contact pressure decay can be described using Eq. 4-1, with the inclusion of surface curvature:

$$p(x) = B1*(x_{edge} - x)^{-1} + B2*(d(x) - d_0) + B3*K + B4 \qquad [4\text{-}3]$$

The velocity of indentation in the hold phase is much smaller than the ramp velocity, and hence, it is not a factor in Eq. 4-3.

Comparing the center node contact pressure to the neural impulse response, similar features exist (Fig. 4-3 and Fig. 4-10). The contact pressure at each point increases as a function of curvature. The rate of increase in the contact pressure during the ramp phase is comparable to the rate of increase in the neural response frequency, for each surface. And the contact pressure during the hold phase decays in a similar manner as the neural impulse decay. Figure 4-18 compares the peak contact pressure for each ramp and hold simulation, to the peak neural response for the corresponding surface curvatures, and a linear relationship can be seen. During the hold phase, the average neural frequency can be predicted by the average contact pressure. This is shown in Figure 4-19, where the predicted neural response is obtained from a linear function of the contact pressure. As can be seen, the contact pressure at the center node is a good indication of the neural response. However, a discrepancy between the two does exist. From Figure 4-10 and the previous discussion, it can be seen that the peak contact pressure at the center node arrives before the end of the ramp phase. The arrival time is proportional to the curvature of the surface. The peak of the neural impulse response (Fig. 4-3), however, occurs at the top of the ramp phase, regardless of surface curvature. Therefore, it can be inferred that the relevant stimulus to the mechanoreceptors must be a filtered version of the contact pressure distribution on the surface of the fingerpad.

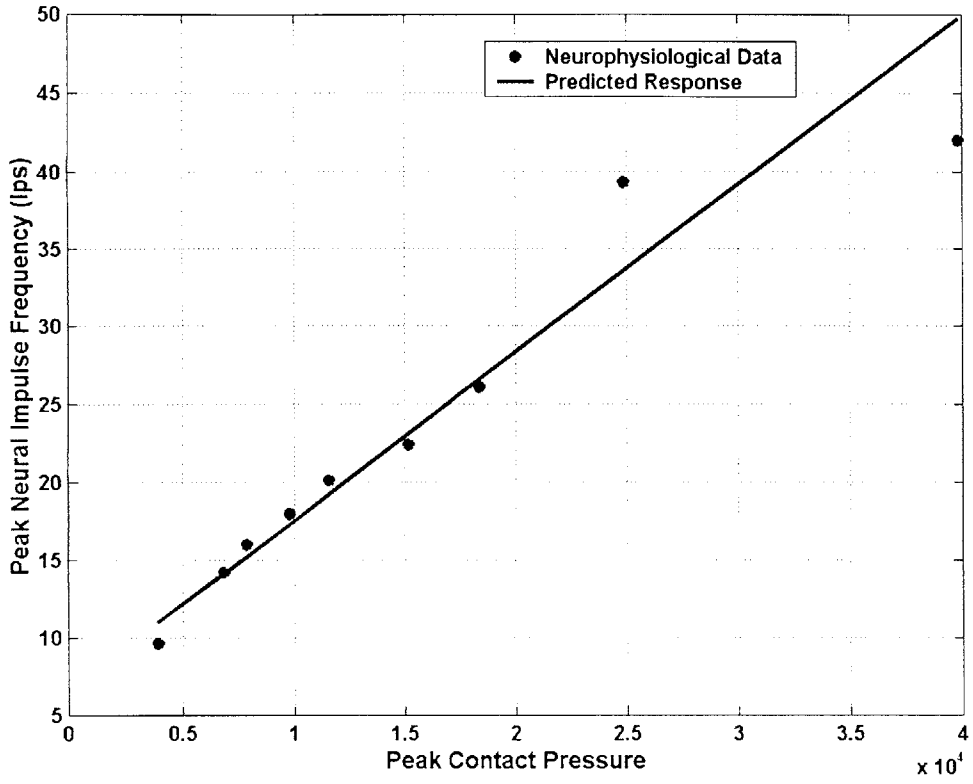

Figure 4-18. Peak neural impulse frequency (using data in Figure 4-3) versus the peak contact pressure obtained from finite element simulations. A flat plate and 8 surfaces of varying curvature were indented into the fingerpad. Neurophysiological data is same as that used for Fig. 4-3 (40 g wt/sec ramp, 20g wt steady force for 2 sec).

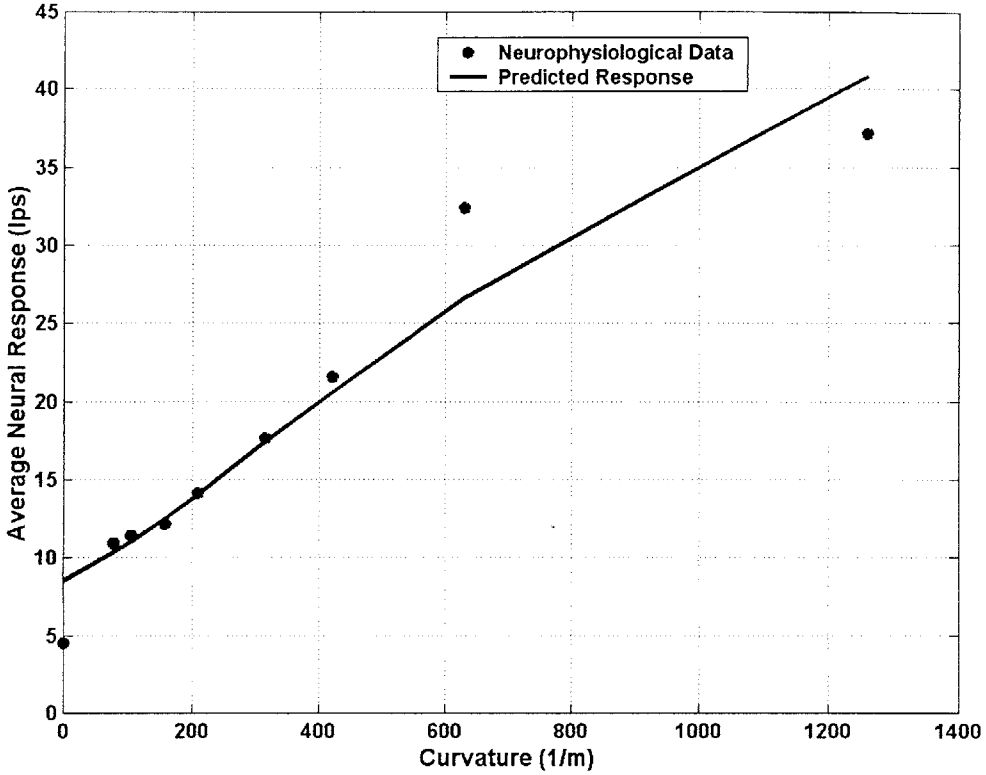

Figure 4-19. Average neural response during the hold phase predicted by the average contact pressure during the decay period compared with the neurophysiological data. A flat plate and 8 surfaces of varying curvature were indented into the fingerpad. Neurophysiological data is same as that used for Fig. 4-3 (40 g wt/sec ramp, 20g wt steady force for 2 sec).

4.5 Relevant Stimulus

The contact pressure on the surface of the skin is only the input to the tactile system. These forces deform the fingerpad and cause stresses and strains at the site of the mechanoreceptors. The goal is to determine the relevant stimulus for each mechanoreceptor. Previous work has shown that strain energy density is a good candidate as the relevant stimulus for SA type mechanoreceptors (Dandekar and Srinivasan, 1996; Raju and Srinivasan, 1999). Neurobiological experiments on receptors found elsewhere in the body, have found that many mechanoreceptors contain *stretch activated ion-channels* (Akoev, 1988). These channels, as the name suggests, allow a current into the cell depending on the stretch across the channel. This increases the voltage potential across the cell membrane, and neural impulses are fired. The impulse rate is proportional to the stretch (i.e. strain) on the cell. Strain energy density is a measure of distortion that involves stretching. Therefore, the possibility of stretch activated ion-channels existing on SA type receptors supports the strain energy density as a plausible stimulus candidate.

The skin acts as a spatial low pass filter to the contact pressure at its surface (Raju and Srinivasan, 1999). The strain energy density profile at the mechanoreceptor depth is a smoothed version of the contact pressure profile at the surface (Figure 4-20). The peak of the strain energy is always at the center point for all indenting surfaces, because the twin off-center peaks of the contact pressure are filtered down in the strain energy profiles, and there is no sharp cut-off at the edges of the contact region.

In addition to the strain energy being a spatially filtered version of the contact pressure, it is time filtered as well. Figure 4-21 is a plot of the strain energy density versus time, at a depth of 915 microns below the surface in the center of the contacting region. The strain energy rate during the ramp phase is much different than the increase rate of the contact pressure. The peak of the strain energy occurs at the top of the ramp, regardless of the surface curvature. As the surface curvature increases, the difference in the magnitudes of the contact pressure and strain energy increases.

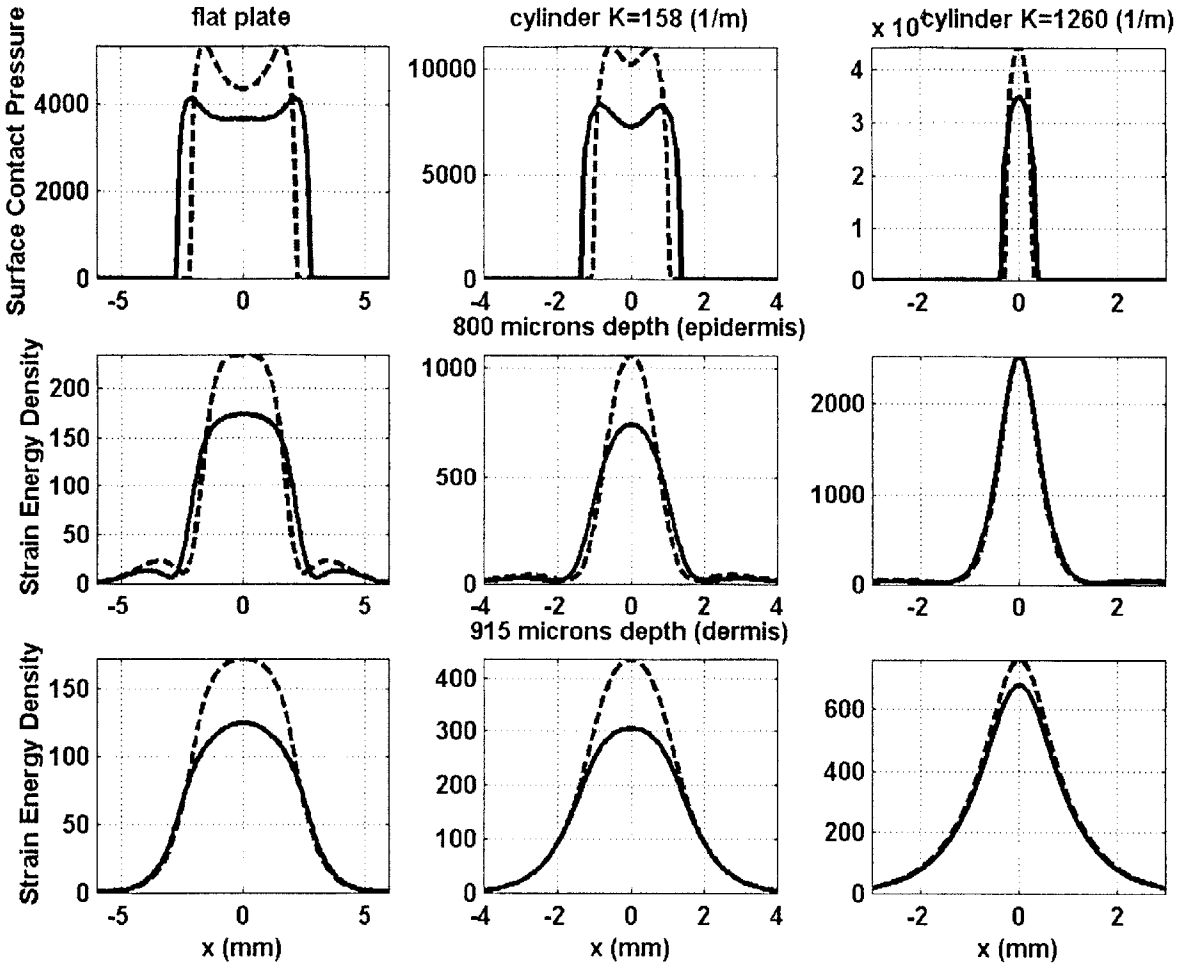

Figure 4-20. Contact pressure profile versus the strain energy density profile at depths of 800 and 915 microns. A flat plate and two curved surfaces were indented into the finger under force control (150 g wt/sec ramp, 20g wt steady force for 2 sec.). dashed line: top of ramp, solid line: steady state profile.

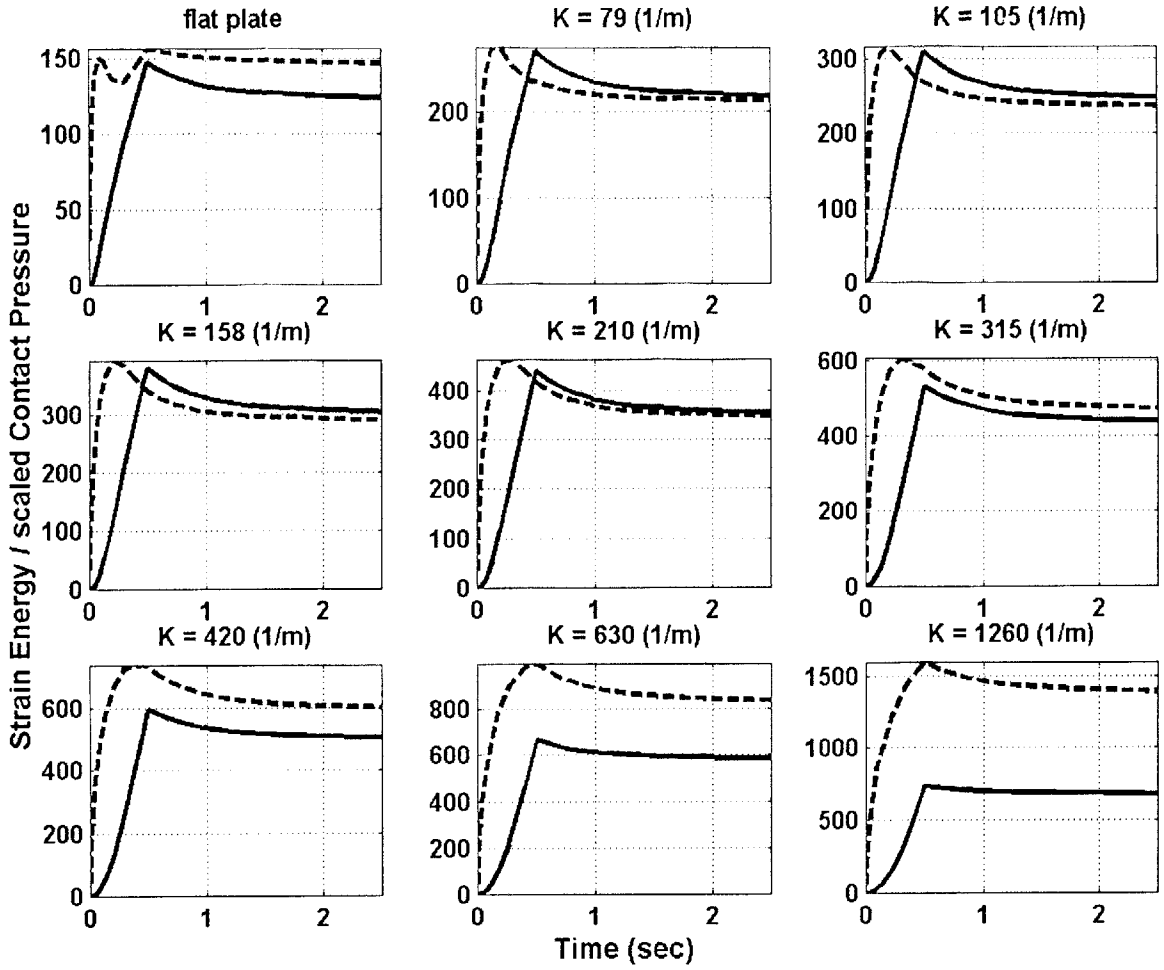

Figure 4-21. Strain energy density at a depth of 915 microns (solid traces) compared to the contact pressure (dashed traces) at the center of the fingerpad, during the ramp and hold simulations of the flat plate and curved surfaces. The contact pressure is scaled by 0.04 in all plots, to fit the axis.

The strain energy density at a given time can be interpreted as a weighted sum of the contact pressure at each point on the surface. The relative contribution from each point decays as the distance from the center line increases. An approximate relationship can be worked out between contact pressure and strain energy density:

$$SE(x_{ref},t) \cong \left[\sum_{x} p(x,t)\cdot e^{-\left|x-x_{ref}\right|/\tau}\right]^2 \cdot \left[A_1 DOI(t) + A_2\right] \qquad \textbf{[4-4]}$$

$SE(x_{ref},t)$ is the strain energy at a location, x_{ref}, and a time, t. $p(x,t)$ is the contact pressure distribution across the finger surface, and τ is the spatial constant that is dependent on the depth at which the strain energy is computed. $DOI(t)$, is the depth of indention of the rigid surface at each point in time; A_1 and A_2 are contacts. The addition of this parameter can be viewed as a scaling factor between spatial distribution of the contact pressure and the strain energy density. The contribution of this factor is because as the depth of indentation increases, the vertical distance between the surface and the point at which the strain energy is computed decreases. Therefore, the magnitude of the strain energy should scale appropriately. The strain energy computed by Eq. 4-4 and the actual strain energy are compared in Figure 4-22, and the results are in good agreement.

The strain energy for ramp and hold simulations, at a center line depth of 915 microns is shown in Figure 4-23. Comparing these plots to the neural response data in Figure 4-2, the strain energy appears to be a good candidate as the relevant stimulus for the SA type receptors. The overall characteristics are the same: a rapid rise during the ramp phase; a slow decay during the hold phase; and the overall magnitude of the response increases as curvature increases.

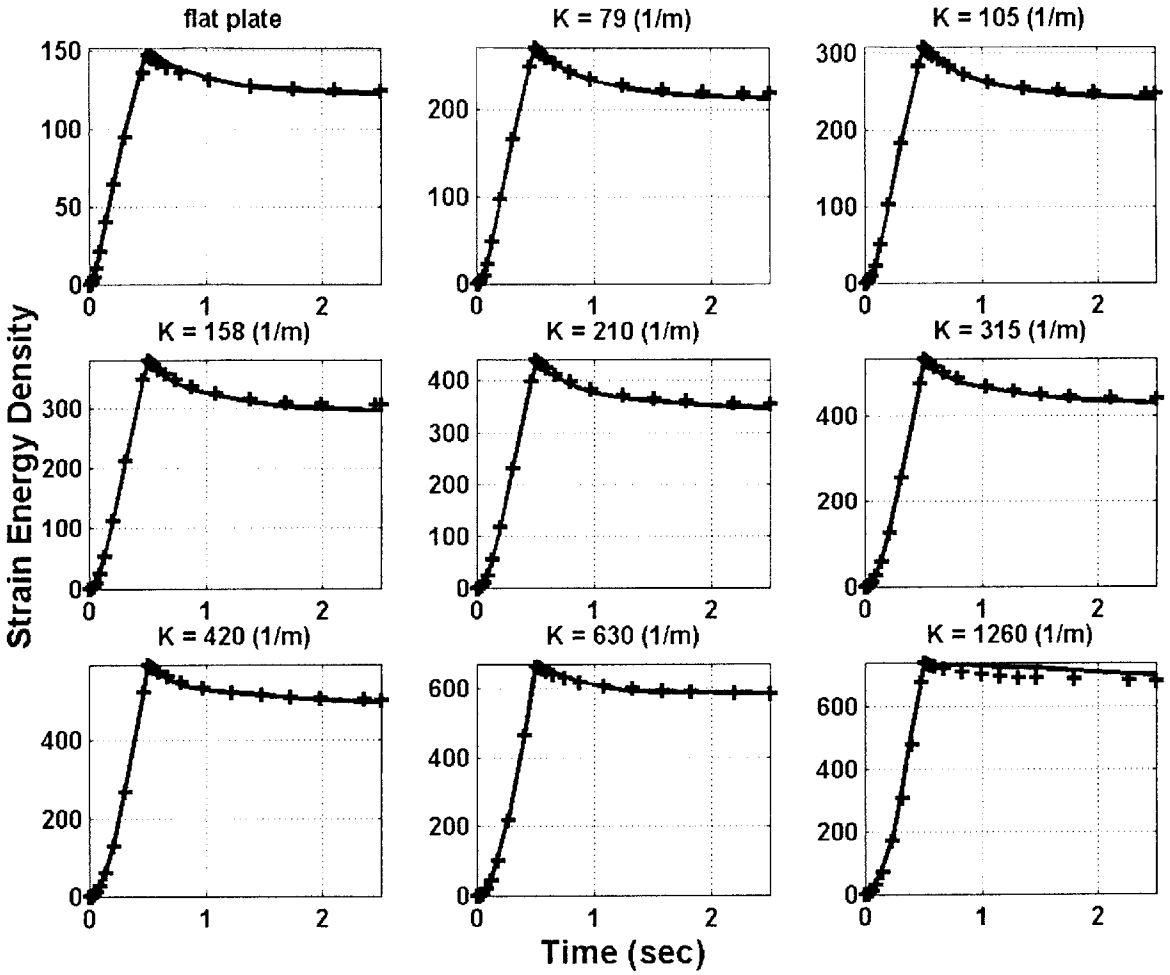

Figure 4-22. Strain energy at a depth of 915 (data points) microns for the ramp and hold simulations. The solid line is the strain energy predicted by the convolution sum of the contact pressure given as Eq. 4-4 in the text.

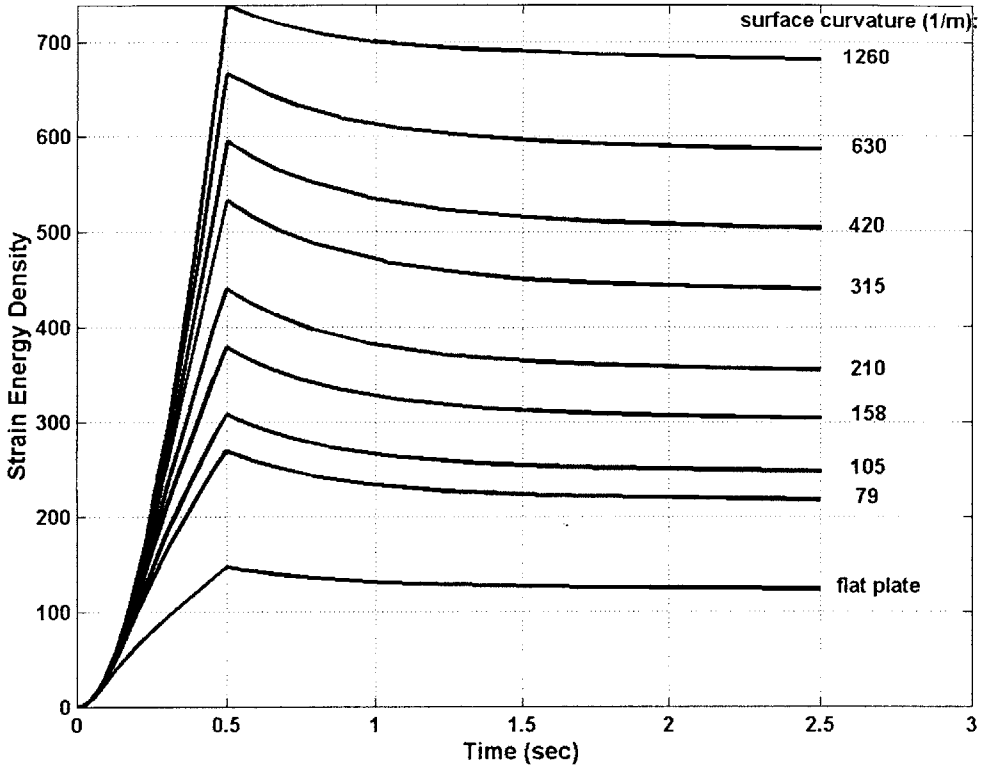

Figure 4-23. Strain energy density over time during the ramp and hold simulations of the flat plate and curved surfaces. Data obtained at a depth of 915 microns, in the center of the fingerpad.

The depth of the mechanoreceptor used in the neurophysiological experiments is not known. SA type receptors are found at a variety of depths, both in the epidermis and the dermis layers. The 915 micron depth is in the dermis layer, and was chosen as an approximate value of the depth. Figure 4-24 shows the strain energy density for the ramp and hold simulations, at other depths both in the dermis and epidermis. While the SE magnitudes differ at the various depths, the same characteristics are evident in each curve set.

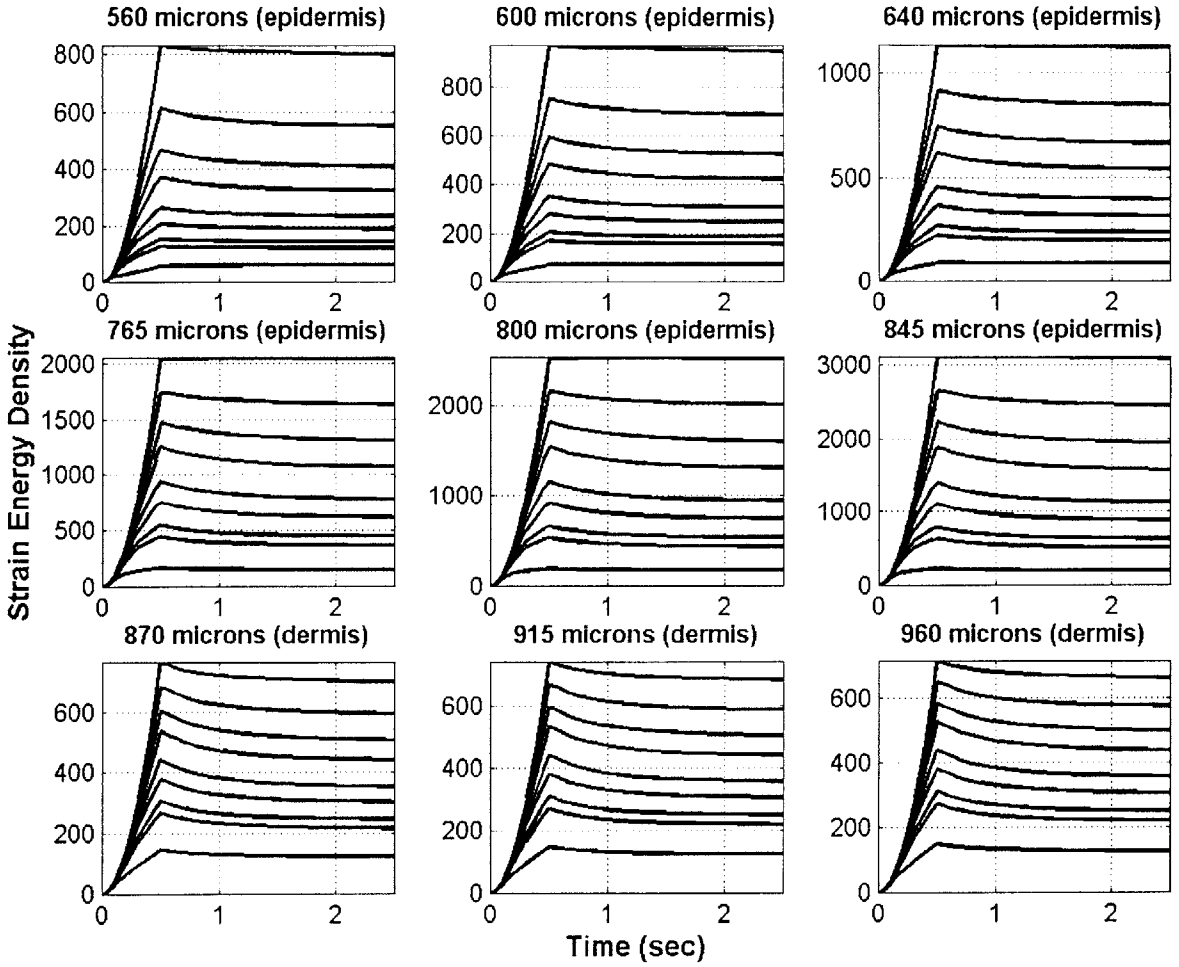

Figure 4-24. Strain energy density at various depths during the ramp and hold simulations of the flat plate and curved surfaces.

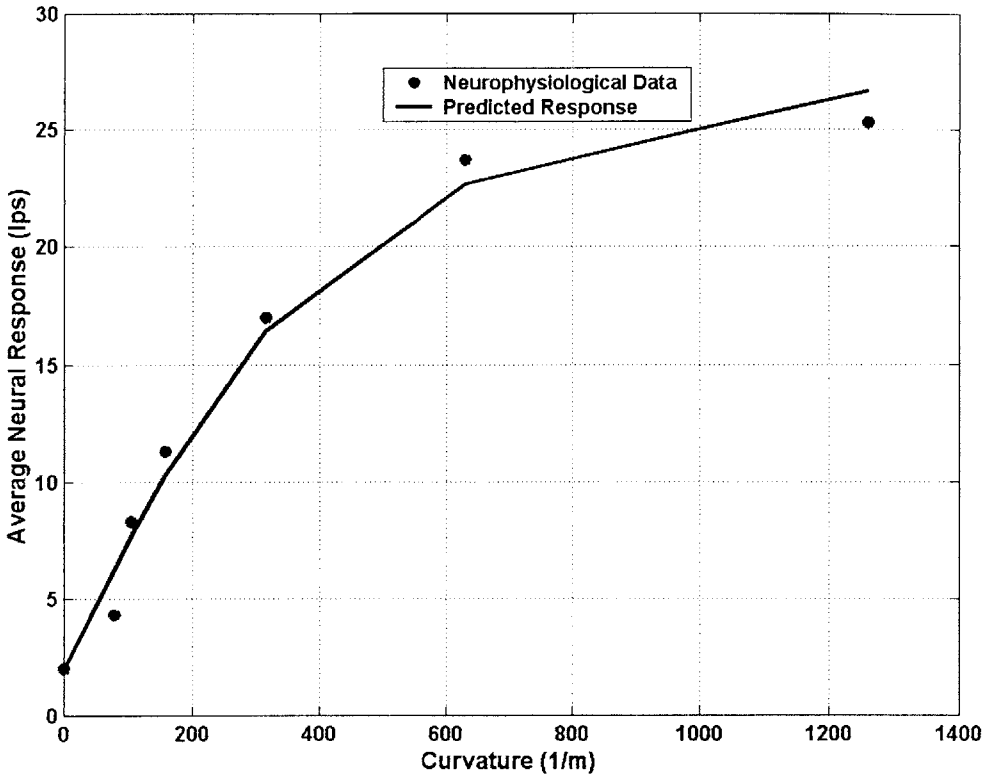

Figure 4-25. Average neural response during the hold phase predicted by the average strain energy at a depth of 915 microns during the decay period compared to the neurophysiological data. A flat plate and 8 surfaces of varying curvature were indented into the fingerpad. Neurophysiological data is taken from Fig. 4-2 (150 g wt/sec ramp, 20g wt steady force for 2 sec).

To verify the strain energy density as a candidate for the relevant stimulus, the average neural impulse frequency during the hold phase is compared to the average strain energy. By examining the hold phase, and averaging the data, any possibly dynamic effects are eliminated. Figure 4-25 shows the average neural response during the hold phase of the data in Figure 4-2, compared to the response predicted by the corresponding average strain energy at a depth of 915 microns. The predicted response is in good agreement with the experimental data, and the strain energy density appears to be a good candidate as the relevant stimulus. Figure 4-26 shows the response predicted by the strain energy compared to the neural response data from Figure 4-3. While the predicted response is

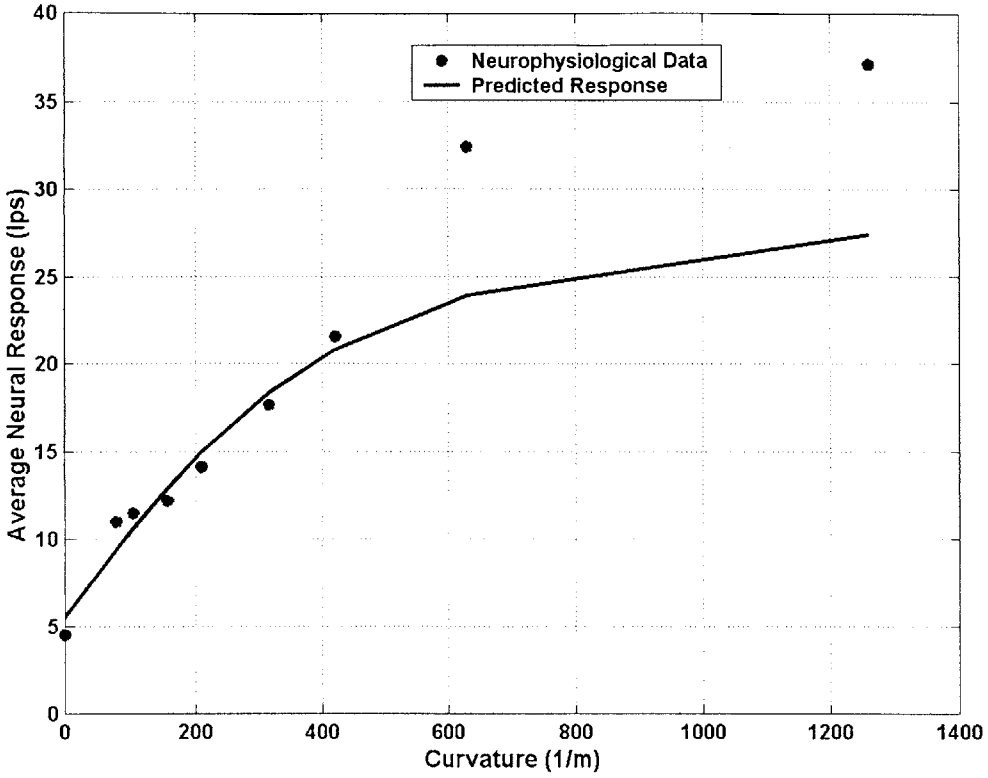

Figure 4-26. Average neural response during the hold phase predicted by the average strain energy at a depth of 915 microns during the decay period compared to the neurophysiological data. A flat plate and 8 surfaces of varying curvature were indented into the fingerpad. Neurophysiological data is same as that used for Fig. 4-3 (40 g wt/sec ramp, 20g wt steady force for 2 sec).

comparable to the actual response for the smaller curvatures, the results diverge as the curvature increases. This is a result of the filtering that occurs in the strain energy as the depth is increased. The high curvature surfaces cause large peaks in pressure at the surface that are filtered away at the depth of 915 microns. The neural data used in Figure 4-25, show that the impulse response due to the highest curvatures was filtered as well. But the data used for Figure 4-26 show reduced effects of the filtering, the sharp curvatures cause a much larger neural response. It is possible that the SA fiber recorded during those experiments was at a lower point closer to the skin surface, where the

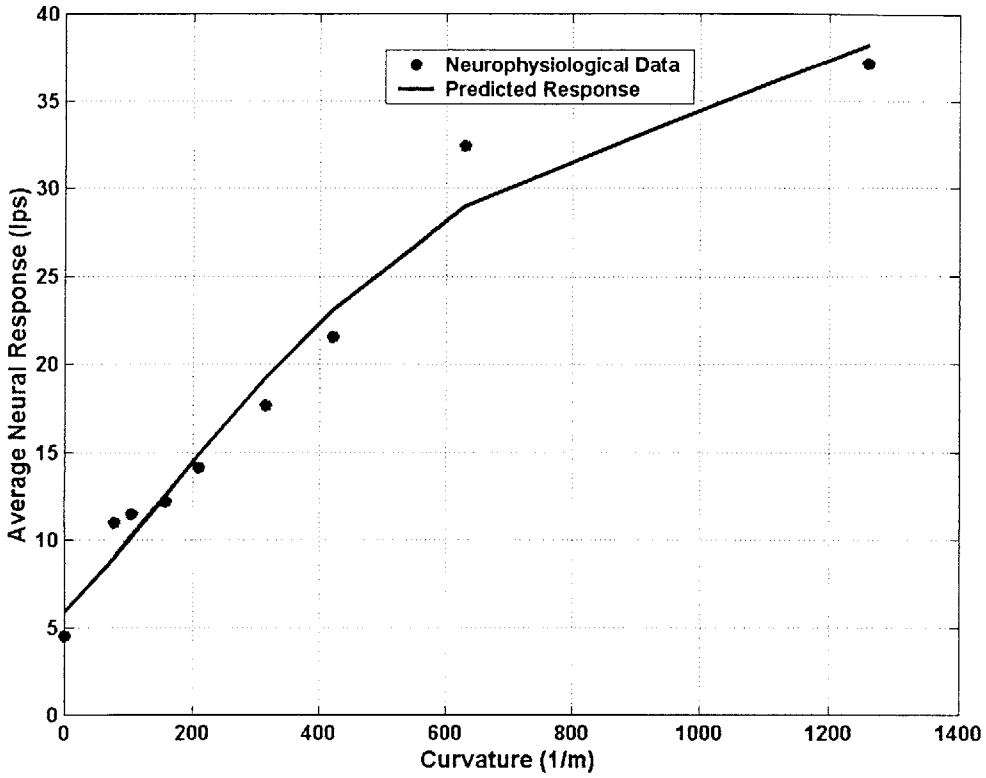

Figure 4-27. Average neural response during the hold phase predicted by the average strain energy at a depth of 600 microns during the hold period compared to the neurophysiological data. A flat plate and 8 surfaces of varying curvature were indented into the fingerpad. Neurophysiological data is same as that used for Fig. 4-3 (40 g wt/sec ramp, 20g wt steady force for 2 sec).

filtering effects are less severe. Figure 4-24 illustrates the filtering effect on the strain energy due to the sharpest curvature, as depth is increased. Using the strain energy at a depth of 600 microns, the neural data in Figure 4-26 can be predicted much more adequately (Fig. 4-27).

While the strain energy can be used to predict the neural response during the hold phase, the shape of the rise portion neural impulse frequency plots is quite different from the strain energy plots (Compare Fig. 4-3 with Fig. 4-23 or Fig. 4-24). However, the strain

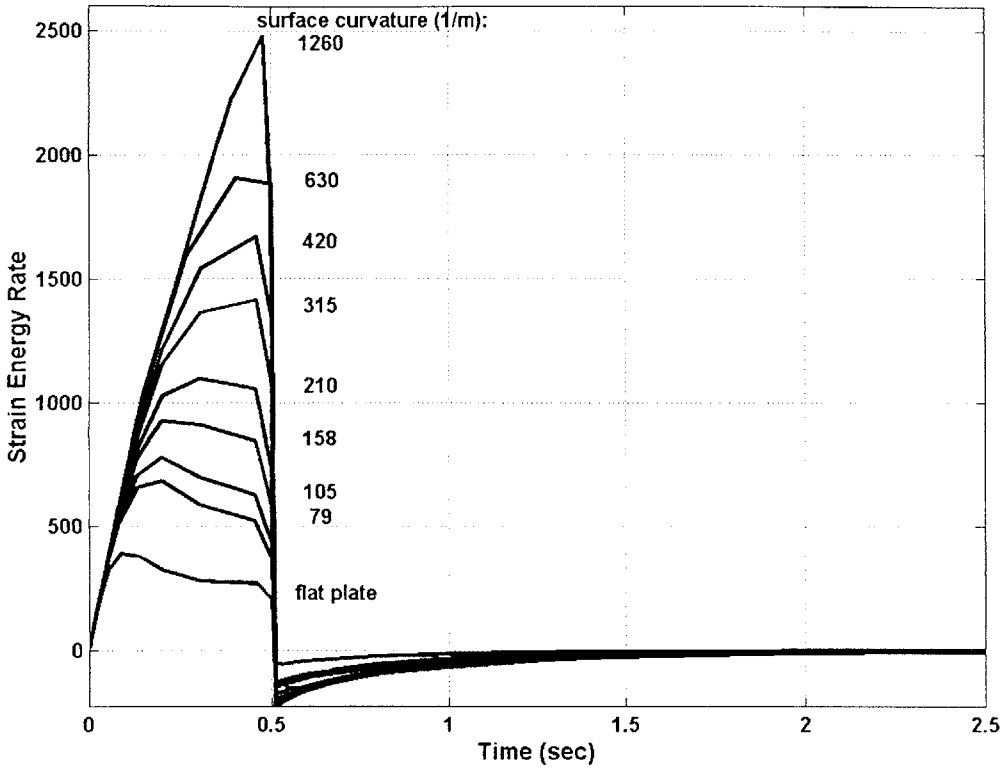

Figure 4-28. Strain energy rate during the ramp and hold simulations of the flat plate and curved surfaces. Data obtained at a depth of 915 microns, in the center of the fingerpad.

energy rate (Fig. 4-28) during the ramp is similar to the corresponding rise in the neural impulse frequency (Fig. 4-3). Previous studies with isolated stretch receptors have shown that the stretch rate as well as the stretch across the ion-channels determine the voltage potential, and subsequent action potentials, across the cell. (Fig. 2-4) Figure 4-29 compares the peak neural response from the experimental data to the peak response predicted by the strain energy rate, from depth of 600 and 915 microns. While both predictions are in good agreement with the experimental data, the strain energy rate at 600 microns (Fig. 4-29a) has a better correlation with the data. This supports the previous claim that the data in Figure 4-3 was obtained from a SA receptor located closer to the surface.

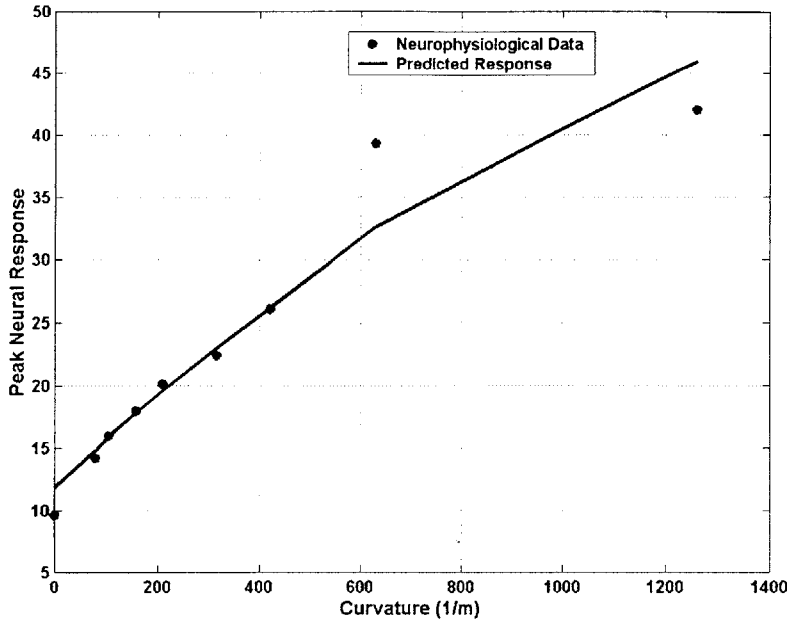

(a)

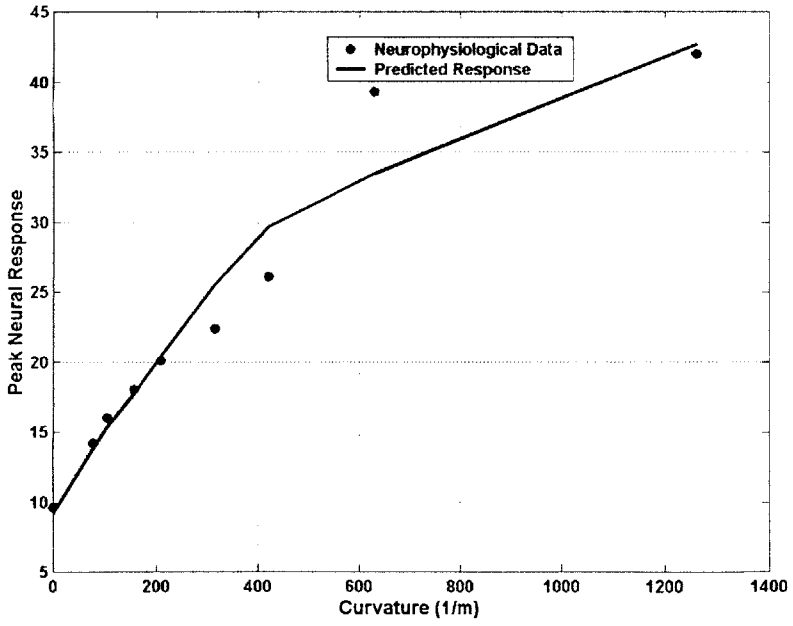

(b)

Figure 4-29a. Peak neural response during the hold phase predicted by the peak strain energy rate at depths of (a) 600 microns and (b) 915 microns, during the decay period compared to the neurophysiological data. A flat plate and 8 surfaces of varying curvature were indented into the fingerpad. Neurophysiological data is same as that used for Fig. 4-3 (40 g wt/sec ramp, 20g wt steady force for 2 sec).

A general relationship can therefore be developed to explain the neural impulse rate during the ramp and hold experiments:

$$IPS = A1*(SE - thresh_1) + A2*(SE_{rate} - thresh_2) + A3 \quad \textbf{[4-5]}$$

5

Tactile Encoding of Shape during Stroking

5.1 Motivation

During active tactile exploration of object shape, the finger is in constant movement over the unknown object. The surface of the object can be considered as a series of curvature segments. While the fingertip is probing the surface, each curvature segment indents and retracts from the skin surface over time. Each segment goes through a similar motion as in the ramp and hold experiments. However, the act of stroking introduces more complexities into the response. There is skin stretch in the contacting region, as well as lateral movement of the mechanoreceptor. The curve segment indentation never reaches a fully static, steady state condition. In order to understand the encoding of curvature during stroking, finite element simulations coupled with neurophysiological recordings from stroking experiments are required.

5.2 Neurophysiological Recordings

LaMotte and Srinivasan (1996) have recorded the neural responses from the monkey fingerpad during stroking experiments with a wavy surface. The surfaces had smooth, alternating convex and concave curve segments, with a succession of curvatures of 26, 39, 52, 79, 105, 157, 210, and 315 m^{-1}. Stroking velocities of 1, 5, 10, 20, and 40 mm/sec were used. Figure 5-1 shows the results from one SA fiber to stroking of this surface, with the 315 m^{-1} curvature segment excluded, at 10 mm/sec from right to left (i.e. from the broadest curve segment to the sharpest). The wavy surface is shown at the top of the figure. As the surface is stroked across the finger, the neural impulses are recorded as

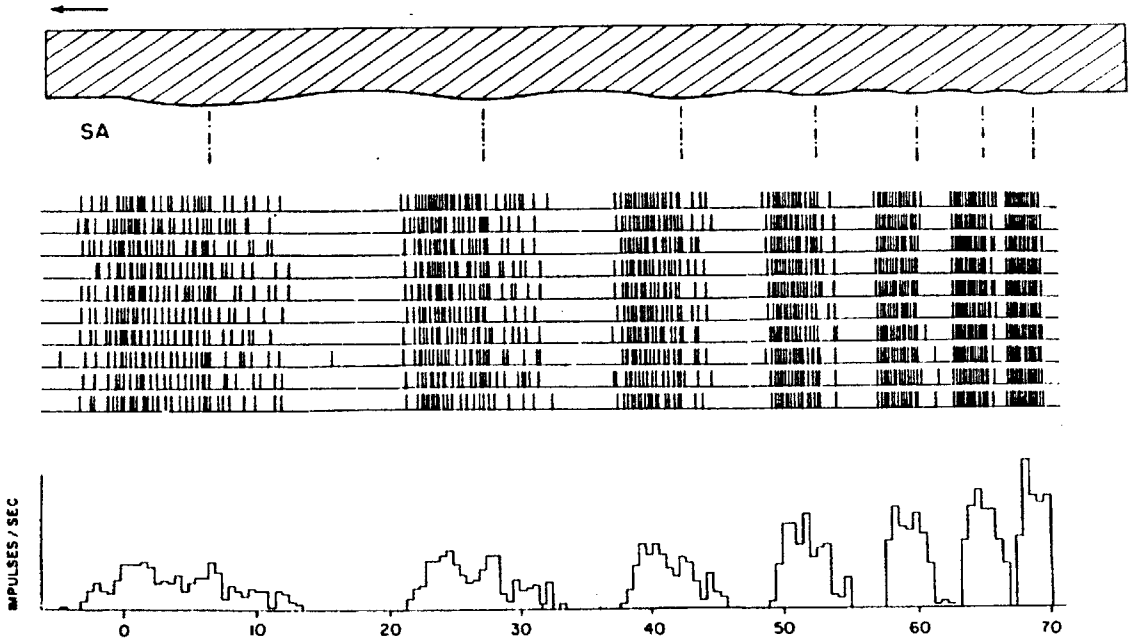

Figure 5-1. Neural response from a single SA mechanoreceptor to a surface of varying curvatures stroked across the monkey fingerpad at a velocity of 10 mm/sec. Ten recordings are shown, each tick mark represents one neural impulse. The x-coordinate of each tick mark represents the location of the most sensitive spot (MSS) in the fiber's receptive field on the skin surface, at the time the action potential occurred. The top trace is the surface used, with convex curvatures, in m^{-1}, of 26, 39, 52, 79, 105, 157, 210. Stroking was from the left part of the surface to the right. The histogram at the bottom represents the mean discharge rate in imp/s calculated with the use of 0.5-mm bins (adapted from LaMotte and Srinivasan, 1996).

tick marks. The middle trace shows the tick marks from one SA fiber for 10 separate strokes. The location of each tick mark corresponded to the location on the surface of the MSS in the fiber's receptive field. As can be seen in the figure, the neural impulses occur when the convex curvature is contacting the skin surface, and no impulses occur during contact with the concavities. Figure 5-2 shows the mean burst width and burst rate for each curvature segment for a SA fiber to the full wavy surface stroked across the finger at 10 mm/sec. The mean discharge rate increases with increasing curvature, while the burst width decreases with increasing curvature.

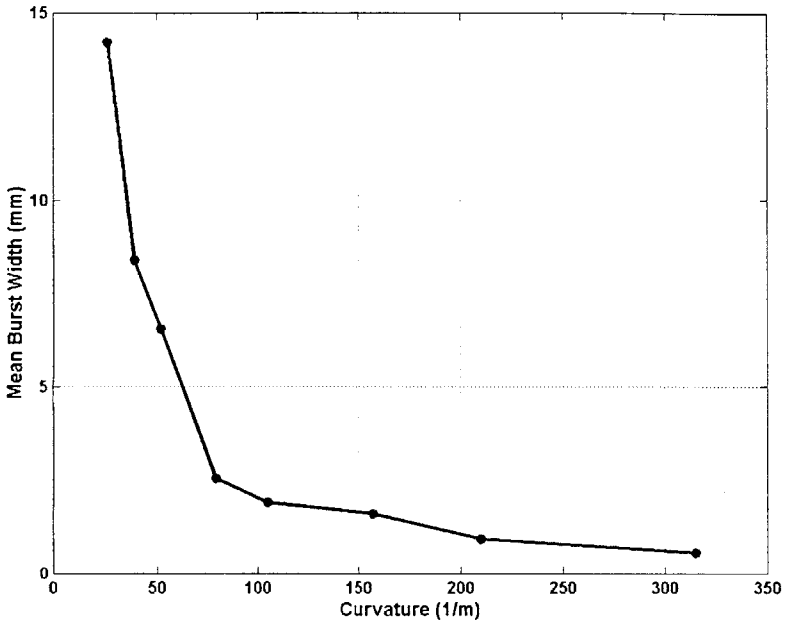

(a)

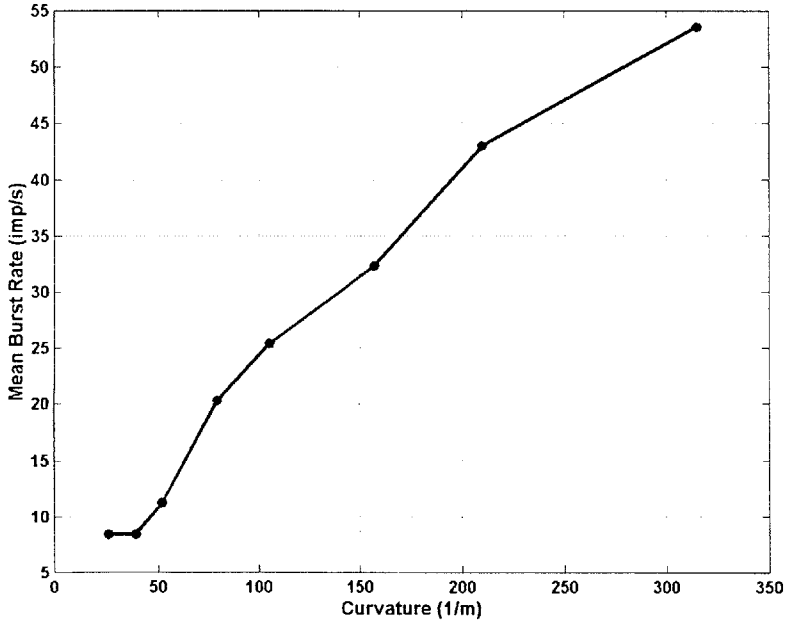

(b)

Figure 5-2. Effect of convex curvature on mean burst width (a) and mean burst rate (b) for a single SA fiber. A wavy surface of smooth, increasing curvature was stroked from the smallest curvature to the largest curvature at 10 mm/sec. Each data point represents the average over 12 strokes

The neural discharge during the ramp and hold experiments has a similar dependence on curvature as does the discharge rate from the stroking experiments (refer to Fig. 4-3). This strengthens the hypothesis that the SA neural response is directly dependent on curvature (Srinivasan and LaMotte, 1987c, 1991). Figure 5-3 shows the mean burst width and mean burst rate for each curvature as the velocity of stroking is changed (LaMotte and Srinivasan, 1996). For each curvature, the burst rate increases for increasing stroking velocity, while the burst width remains approximately the same. As the curve segments stroke across the fingerpad, the length of the surface segment that contacts the MSS of the SA fiber is the same regardless of the stroking velocity. This explains why the burst width is only a function of curvature and not velocity. Figure 5-4 shows the length of the surface that contacts the skin for each curvature segment determined from FE simulations, compared with the burst widths from stroking at 5, 10, 20, and 40 mm/sec. There is good agreement between the simulated results and the experimental data. The burst rate increases both for increasing curvature and increasing stroking velocity. While the curve segment is in contact with the skin, the local curvature on the skin surface is the same as that of the curve segment, regardless of stroking velocity. The increase in velocity results in an increase in the rate of change of the local curvature. This supports the initial hypothesis that the SA neural impulse frequency is proportional to both the local curvature and the time derivative of the local curvature in the MSS on the skin surface (Srinivasan and LaMotte, 1987c, 1991).

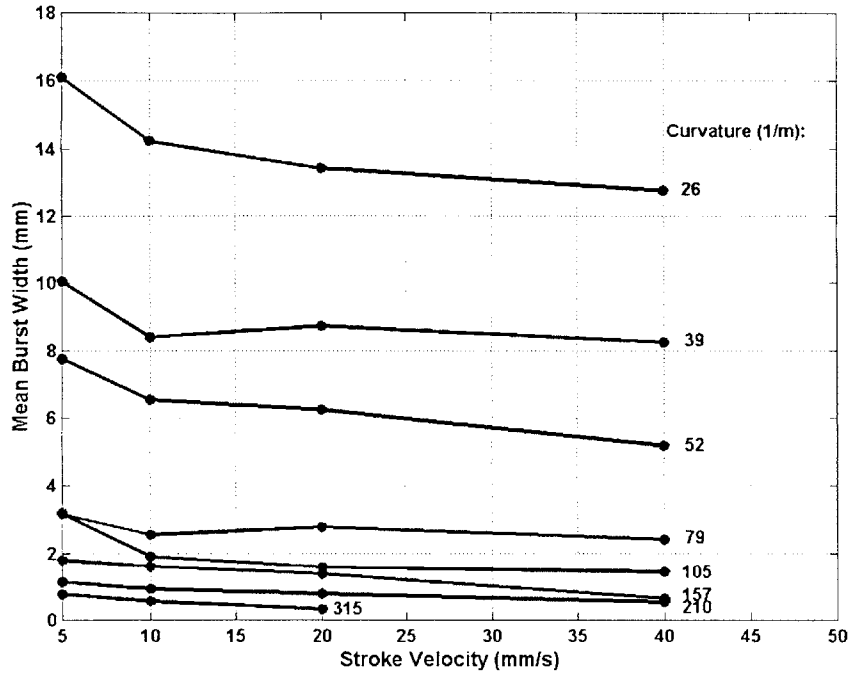

(a)

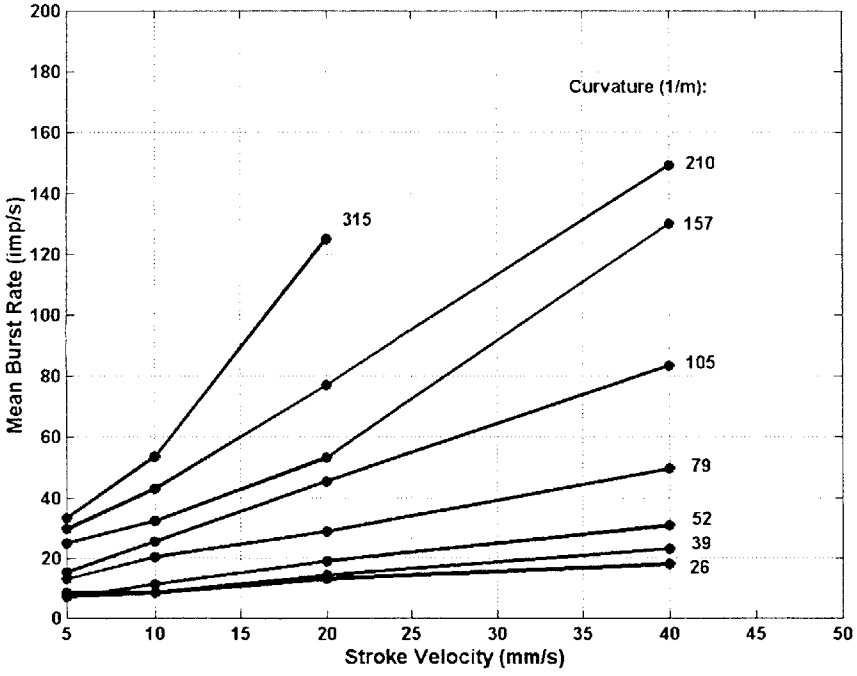

(b)

Figure 5-3. Effect of velocity on mean burst width (a) and mean burst rate (b) for a single SA fiber. A wavy surface of smooth, increasing curvature was stroked from the smallest curvature to the largest curvature, and the response from each convex curvature is shown. Each data point represents the average for 12 strokes.

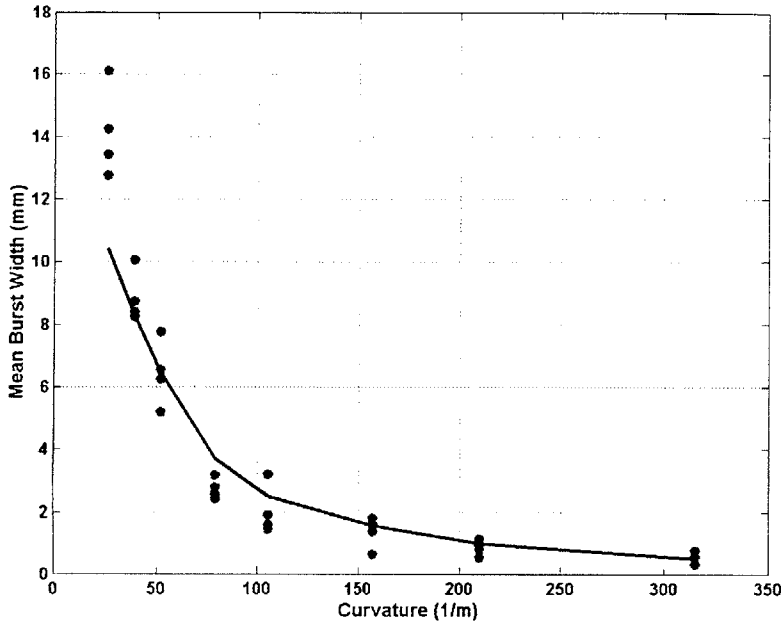

(a)

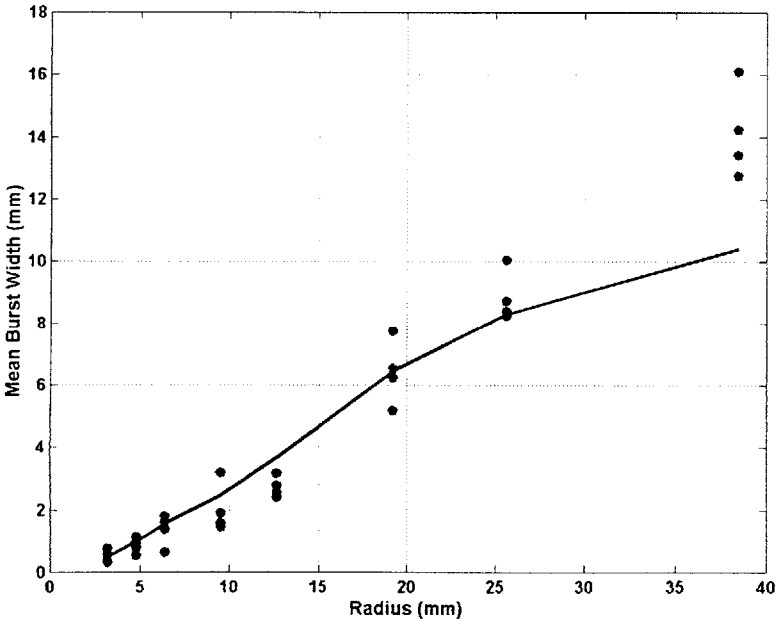

(b)

Figure 5-4. Mean burst width versus (a) curvature and radius (b) for stroking velocities of 5, 10, 20, and 40 mm/sec. Stroking is from the smallest curvature to the largest curvature. Each data point represents the average response from an SA fiber for 12 strokes. The mean burst width measures the distance the contacting surface traveled during the neural response. The solid line is the width of the curvature segment that is in contact with the MSS of the SA fiber, obtained from FE simulations.

5.3 Contact Mechanics

Finite element simulations were performed using the fingerpad model created and verified in Chapter 3. The same wavy surface used in the neurophysiological experiments was stroked across the fingerpad model at different velocities. At first, the effects of stroking and skin stretch were eliminated by stepping the surface across the fingerpad in increments of 1 mm. The surface was indented into the fingerpad until steady state conditions were reached. Then it was retracted, shifted by 1 mm, and indented into the fingerpad again. The surface deformation and contact pressure profiles are shown at three locations of the wavy surface, in Figure 5-5. A sharp corner separates the beginning flat plate portion of the surface and the first curve segment. At this point, as can be seen in the figure, the sharp corner does not contact the skin, and the contact pressure goes to zero. Once the curve segment comes in full contact with the skin, a similar contact pressure profile can be seen that is comparable to the steady state profile of the ramp and hold simulations (refer to Fig. 4-11). The contact pressure profile when the concave segment indents the skin is similar to the convex curvature profiles, except with a smaller magnitude. On the edge of the profile, where the next convex curvature contacts the skin, a sharp peak in the contact pressure can be seen. Figure 5-6 shows the contact pressure profiles at the same locations on the wavy surface, from stroking the surface at a velocity of 10 mm/sec. The skin stretch resulting from stroking is evident in the surface deformation profiles. The contact pressure profiles are very similar to the stepped profiles in Figure 5-5, except shifted to the left approximately 1mm due to the skin stretch.

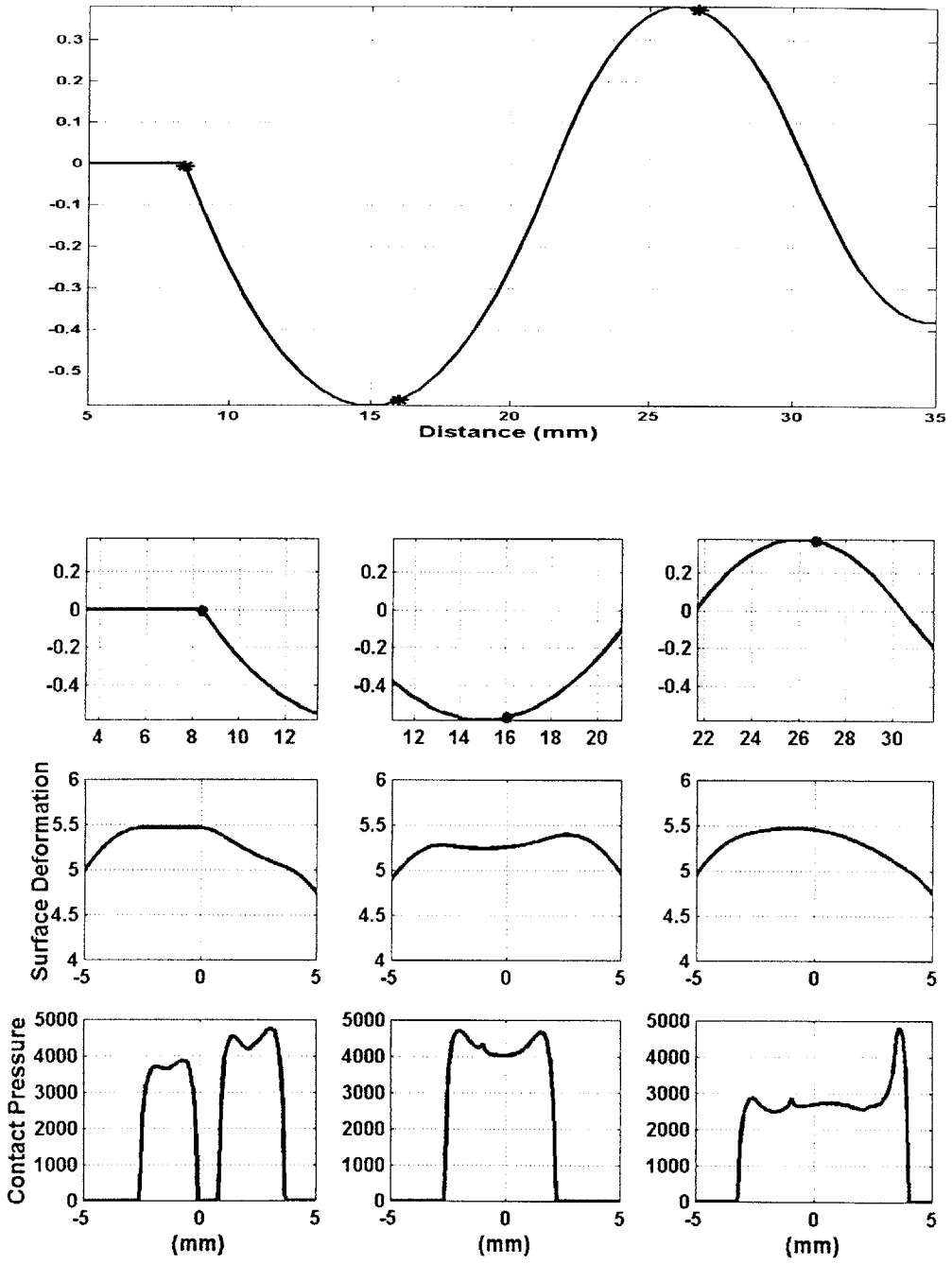

Figure 5-5. Contact pressure profiles from finite element simulations of wavy surface stepped across the fingerpad. The top trace is the stimulus shape and the 3 locations where the contact profile is plotted are shown as stars. The bottom traces are the surface deformation and contact pressure profiles at the 3 locations. The convex curvatures are, in m^{-1}, 26 and 39; the concave curvature is 39 m^{-1}. (Surface deformation is in mm)

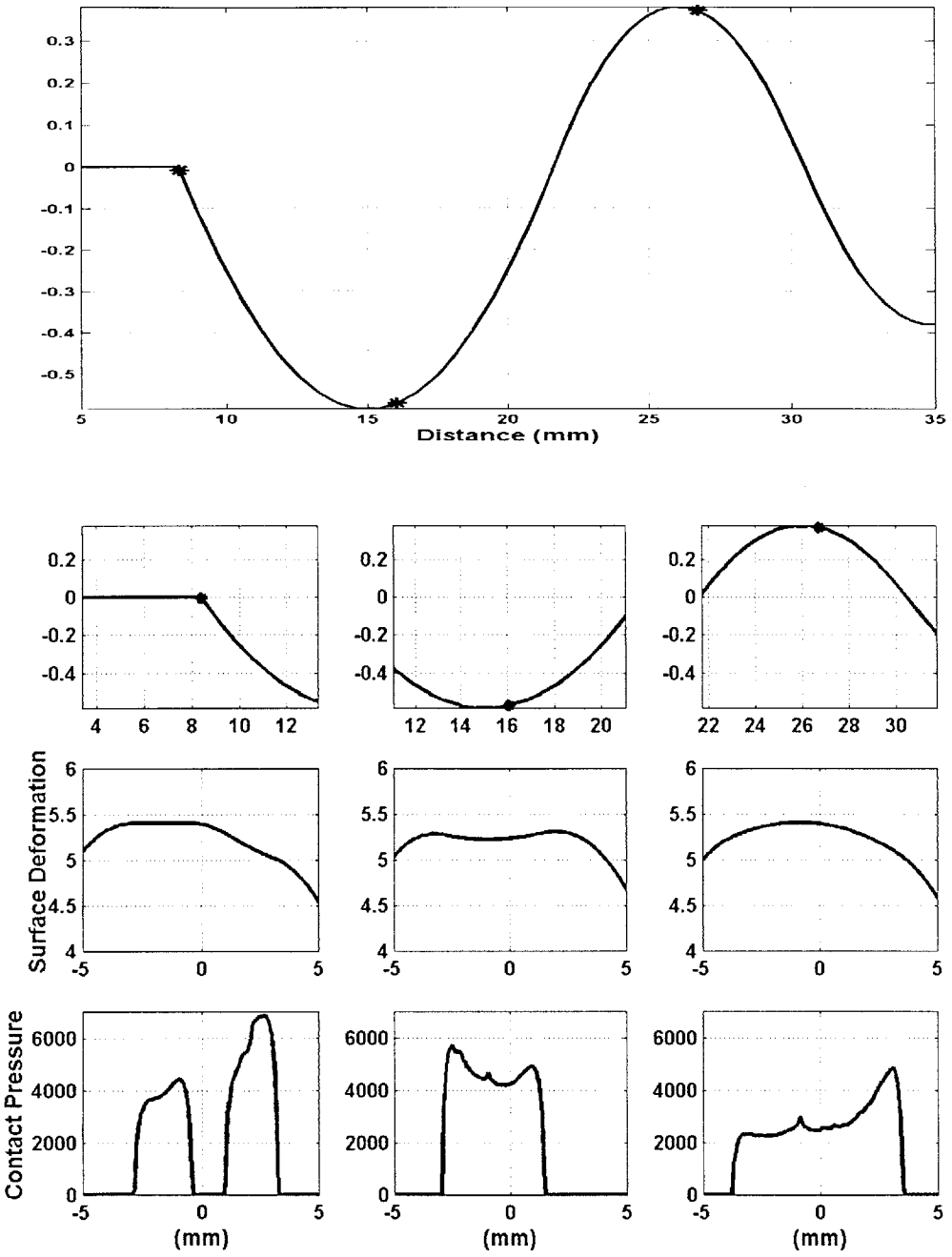

Figure 5-6. Contact pressure profiles from finite element simulations of wavy surface stroked across fingerpad at a velocity of 10 mm/sec. The top trace is the wavy surface stroked across the fingerpad and the 3 locations where the contact profile is plotted are shown as stars. The stroking was in a direction of the left part of the surface to the right. The bottom traces are the surface deformation and contact pressure profiles at the 3 locations. The convex curvatures are, in m^{-1}, 26 and 39; the concave curvature is 39 m^{-1}. (Surface deformation is in mm)

An important consideration while examining the contact pressure profiles is the location of the most sensitive spot (MSS) of the SA fiber being recorded. During ramp and hold experiments, the center of the fingerpad does not shift laterally, and therefore the MSS remains in the center. When the surface is stroked across the finger, there is significant lateral movement of the skin surface. Because the SA mechanoreceptor is located close to the skin surface, it can be assumed that the receptor shifts along with the skin surface. The difference in the receptor shift and the skin surface shift should be small, and can be neglected. While analyzing the contact pressure profiles due to stroking, it will be assumed that finite element nodes located in the MSS of the SA receptor remain the same regardless of skin stretch.

In order to compare the results from different stroking velocities, the time frame will be converted into distance. The distance refers to the lateral displacement of the stroking surface. The fingertip is fixed and the wavy surface strokes across it at a constant velocity. The distance traveled is equal to the time elapsed multiplied by the stroking velocity. The zero reference will be the point on the wavy surface that is in contact with the center of the fingertip at t=0. For instance, in Figure 5-1, the neural response at x=30 mm is the receptor response when the point on the wavy surface 30 mm from the zero reference is located at the center of the fingerpad. For the stroking experiments and simulations in this thesis, the stroking is from left to right: initially the left edge of the surface (the broadest curve segment) is in contact with the skin; the surface then strokes across the surface until the right edge is reached (the sharpest curve segment). This stroking description will be referred to as in a direction from left to right.

Figure 5-7 is a plot of the contact pressure from the center node of the fingerpad, while a segment of the wavy surface is stepped across the fingerpad as previously described. Also shown is the local curvature at the center of the fingerpad, linearly scaled to fit the contact pressure profile. As can be seen, the contact pressure is directly proportional to the skin curvature. The small differences can be explained by the depth of indentation and contact width arguments proposed in Chapter 4. However, these nuances are small; the main contribution to the contact pressure is the local curvature on the skin surface.

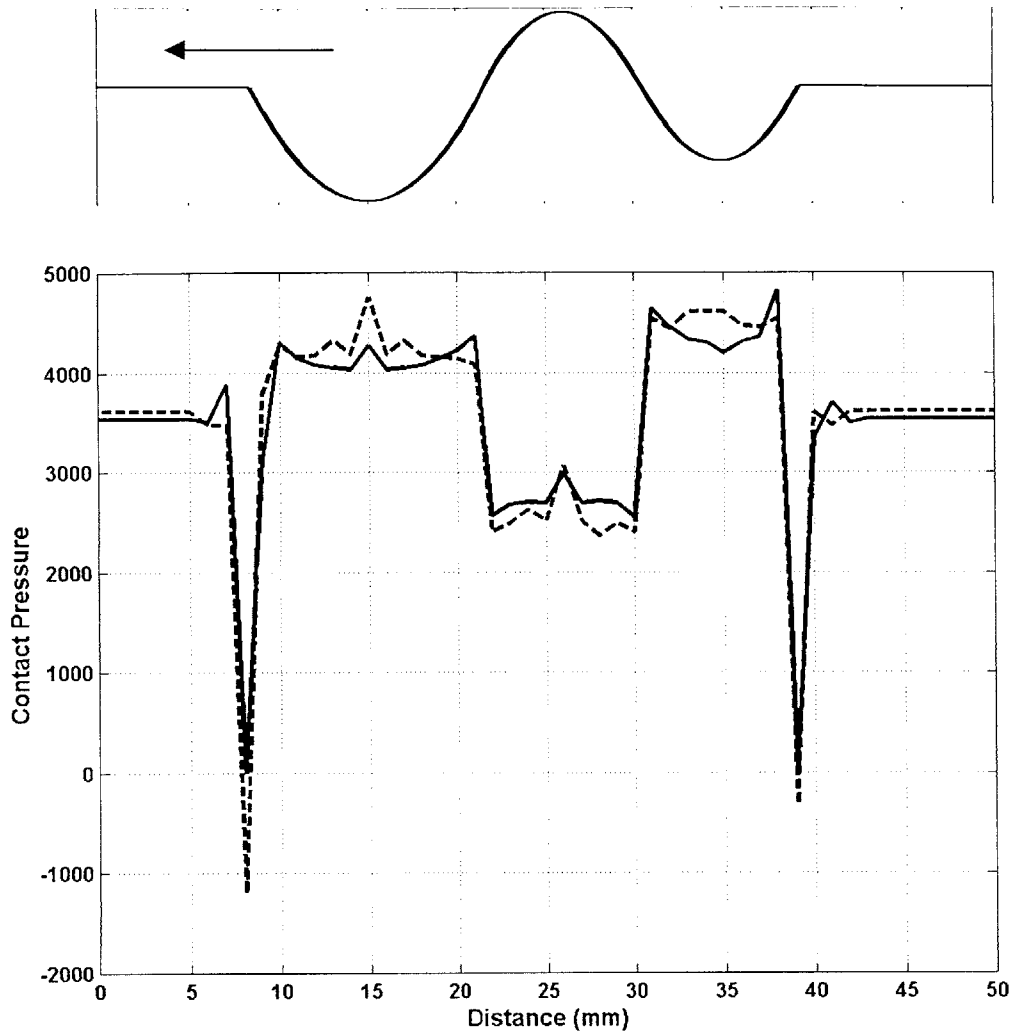

Figure 5-7. FE simulation results. Contact pressure (solid line) at the center node of the fingerpad as the surface shown in the top trace is stepped along the fingerpad in increments of 1 mm, from the left part of the surface to the right. The dashed line the curvature at the top of the skin, linearly scaled by A1*K + A2. The convex curvatures are, in m^{-1}, 26 and 39; the concave curvature is 39 m^{-1}.

During stroking, the center node of the finger model shifts in the direction the surface is moving. Assuming that the mechanoreceptor shifts approximately the same amount, then the center node should remain in the MSS of the receptor. Figure 5-8 compares the contact pressure at that point during stroking at 10 mm/sec, to the contact pressure obtained from stepping the surface across the finger. The lateral displacement of the

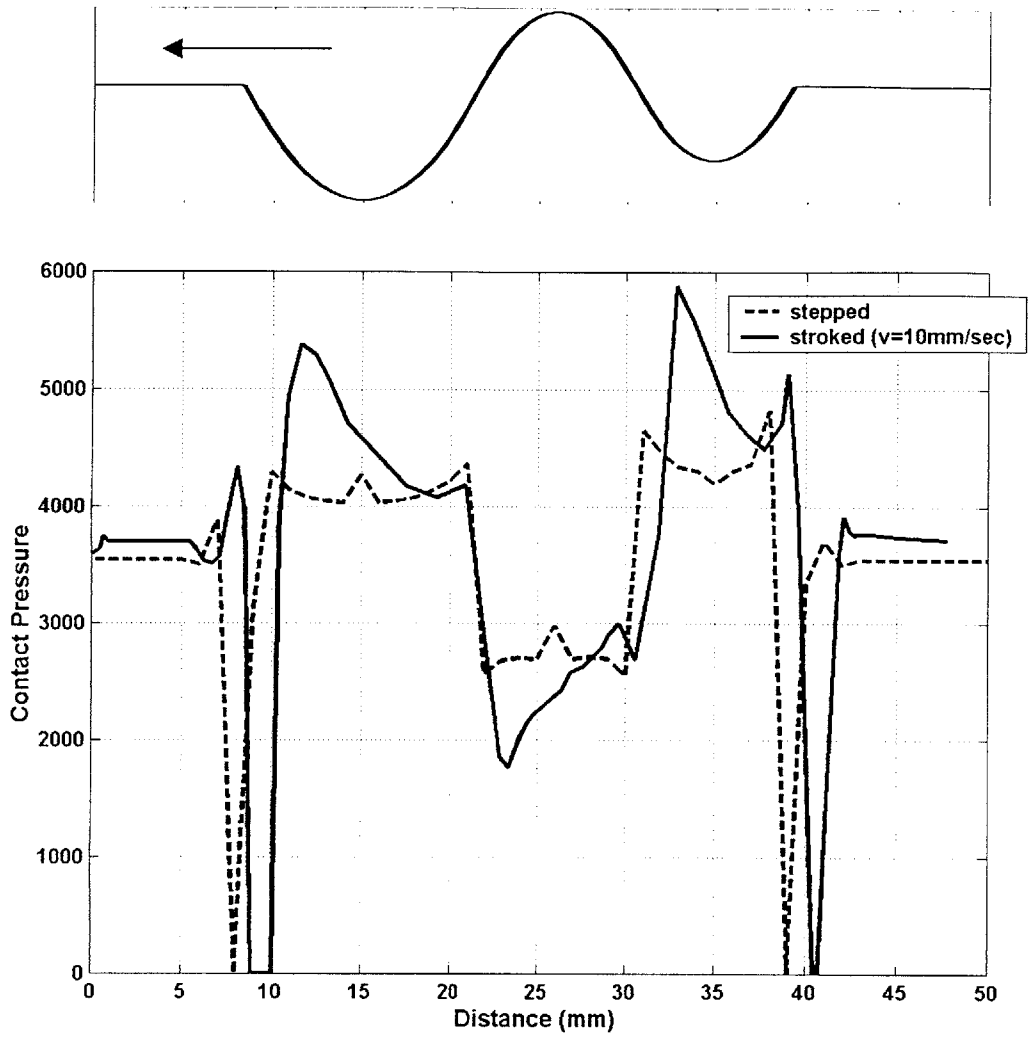

Figure 5-8. FE simulation results. Contact pressure at the center node of the fingerpad as the surface shown in the top trace is stepped along the fingerpad in increments of 1 mm, (dashed line), and stroked at v=10 mm/sec (solid line), from the left part of the surface to the right. The convex curvatures are, in m^{-1}, 26 and 39; the concave curvature is 39 m^{-1}.

center node is evident by examining the time that the node loses contact with the surface. Because the node is displacing to the left (for stroking from the left end of the surface to the right), there is a lag in time before the sharp corner contacts the node of interest. This can be seen as a lag in the contact pressure profile for the node. The overall contact pressure profile is similar in magnitude and shape for stroking and stepping simulations.

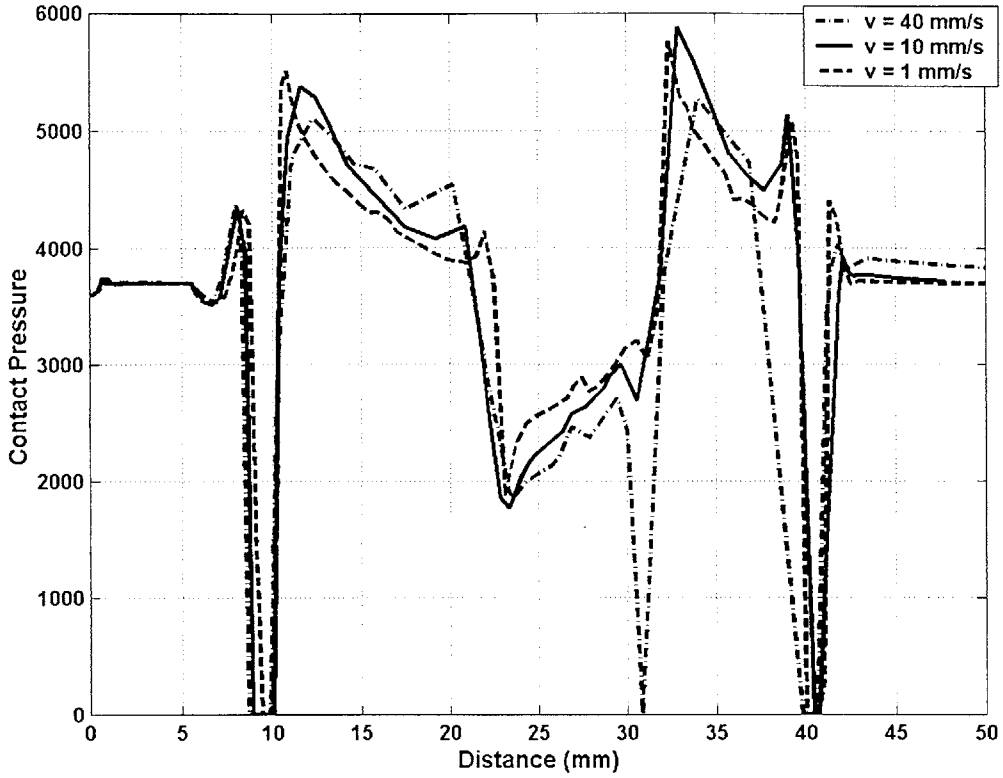

Figure 5-9. FE simulation results. Contact pressure at the center node of the fingerpad as the surface shown in the top trace is stroked across the fingerpad at v=1, 10 and 40 mm/sec, from the left part of the surface to the right. The convex curvatures are, in m^{-1}, 26 and 39; the concave curvature is 39 m^{-1}.

The major difference is in the dynamic peaks accompanying the beginning of the convex and concave curvature segments. The profiles obtained from stroking have a more pronounced peak at these stages. For different velocities of stroking, the contact pressure profiles remain approximately the same (Figure 5-9). The dynamic peaks and the lateral skin displacement change slightly depending on velocity, but the effect is small. The only major discrepancy is that for a stroking velocity of 40 mm/sec, the node of interest loses contact with the surface before both the first and second convexity. Overall, the contact pressure profile for the center node of the MSS is approximately indifferent to the stroking velocity. It can be concluded that the viscoelastic time constants associated with the dynamics of the skin are much faster than the stroking velocities simulated with the finite element model, and the response is approximately elastic for these cases.

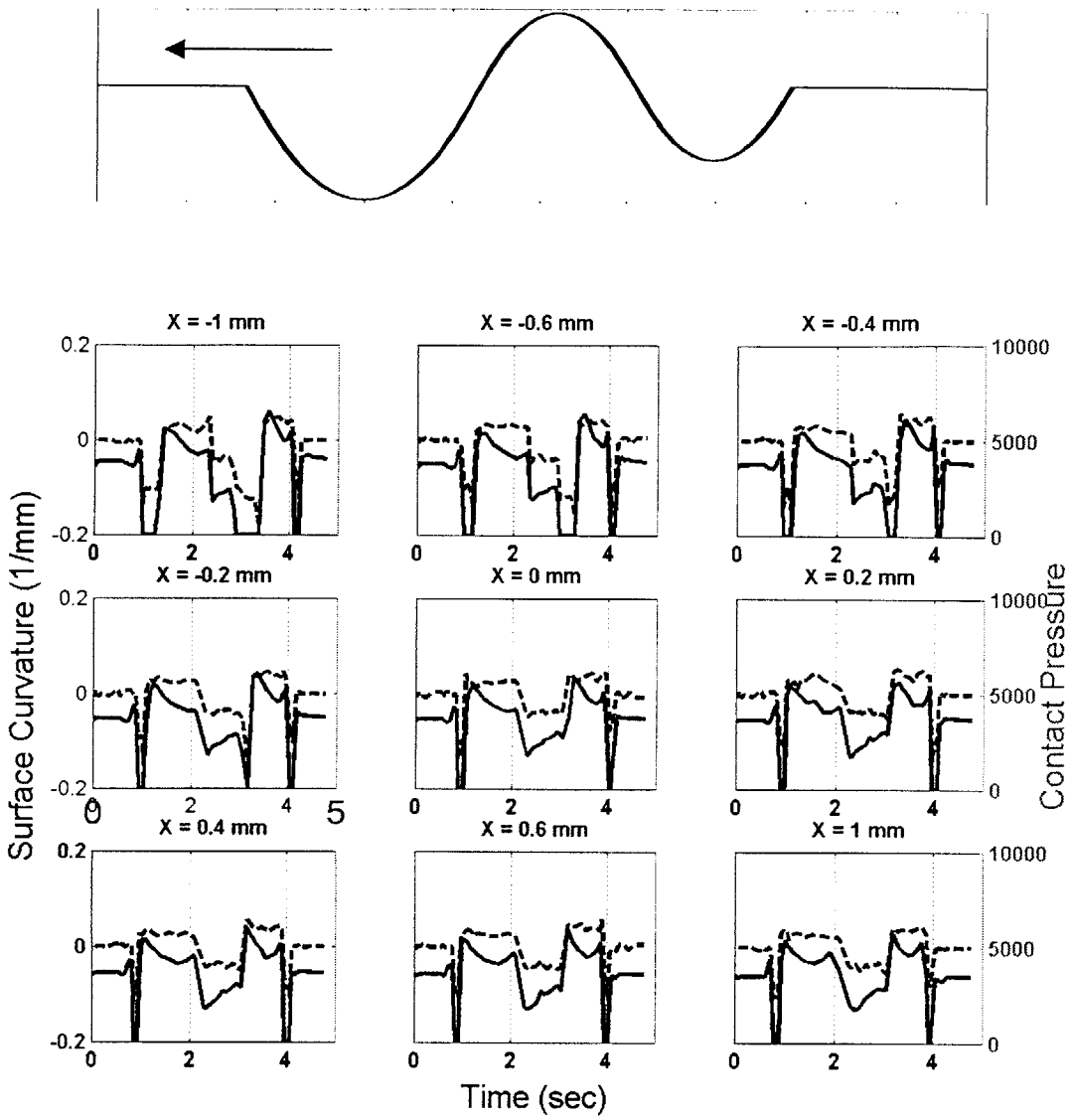

Figure 5-10. FE simulation results. Contact pressure (solid line) and skin curvature (dashed line) over time for 9 locations across the MSS of the fingerpad, as a surface with two convex curves is stroked at 10 mm/sec, from the left part of the surface to the right. The convex curvatures are, in m^{-1}, 26 and 39; the concave curvature is 39 m^{-1}.

In the stepping simulation, the contact pressure profile was found to be directly related to the local curvature. This is also true for the stroking simulations. Figure 5-10 shows the contact pressure profile at different locations in the MSS of the SA receptor. Also shown is the local curvature at that point. It can be seen that the contact pressure profile over

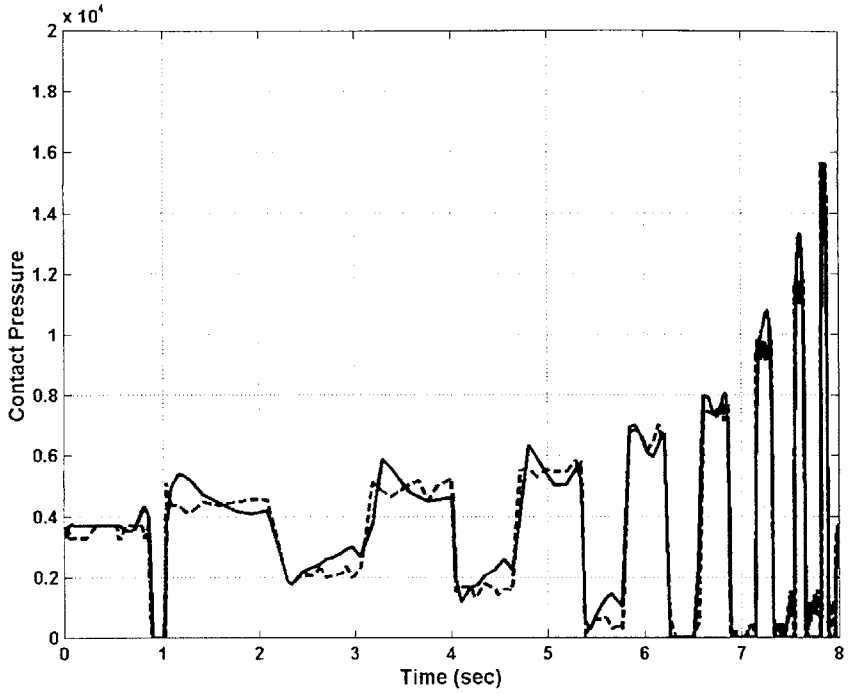

Figure 5-11. FE simulation results. Contact pressure (solid line) at the center node of the MSS as the wavy surface described in text is stroked across the fingerpad from the broadest curve segment to the sharpest. The dashed line is the curvature at the node, linearly scaled by A1*K + A2. The convex curvatures that comprise the wavy surface are, from left to right, 26, 39, 52, 79, 105, 157, 210, and 315 m^{-1}.

time approximately follows the curvature profile. The small differences can be explained by complex arguments given in Chapter 4, but the overall agreement between curvature and contact pressure is evident in the figure (The curvature and contact pressure is plotted on different scales, chosen to facilitate separation between the two traces). Using the entire wavy surface, the same curvature to contact pressure relationship can be seen. Figure 5-11 is the contact pressure at the center node of the MSS compared to a linear function of the skin curvature at that point. There is good agreement between the two for the full range of curvatures comprising the wavy surface. From both the ramp and hold simulations and the stroking simulation, it can be seen that the surface curvature is the primary factor in the contact pressure profiles.

5.4 Relevant Stimulus

In chapter 4 it was established that the strain energy density is a good candidate as the relevant stimulus for the SA mechanoreceptor. Figures 5-12 and 5-13 show the contact pressure profile at the center node and the strain energy density at a depth of 915 microns, respectively, from the finite element simulations. The full wavy surface was stroked across the fingerpad from the broadest curvature to the sharpest, at velocities of 1, 5, 10, 20, and 40 mm/sec. The previous notion that the contact pressure profile is approximately independent of velocity is supported from examination of Figure 5-12. The peak of the contact pressure for each curvature segment is directly related to the surface curvature. The variation due to stroking velocity is small and negligible. The strain energy density shows no significant dependence on stroking velocity either. For all velocities, the strain energy density is a smoothed function of the contact pressure, as stated in chapter 4. There is one notable exception, however. For the two largest curvatures, the strain energy decreases. This is inconsistent with the results from the ramp and hold section, where the strain energy increased as the surface curvature increased. Because the highest curvature segments are spaced close together, as they stroke across the fingerpad, multiple curvatures are in contact with the skin surface simultaneously. Therefore, the applied force is spread over each curvature, and the effect from the individual curvature is not as pronounced as in the ramp and hold simulations with a single curvature indenting the fingertip skin.

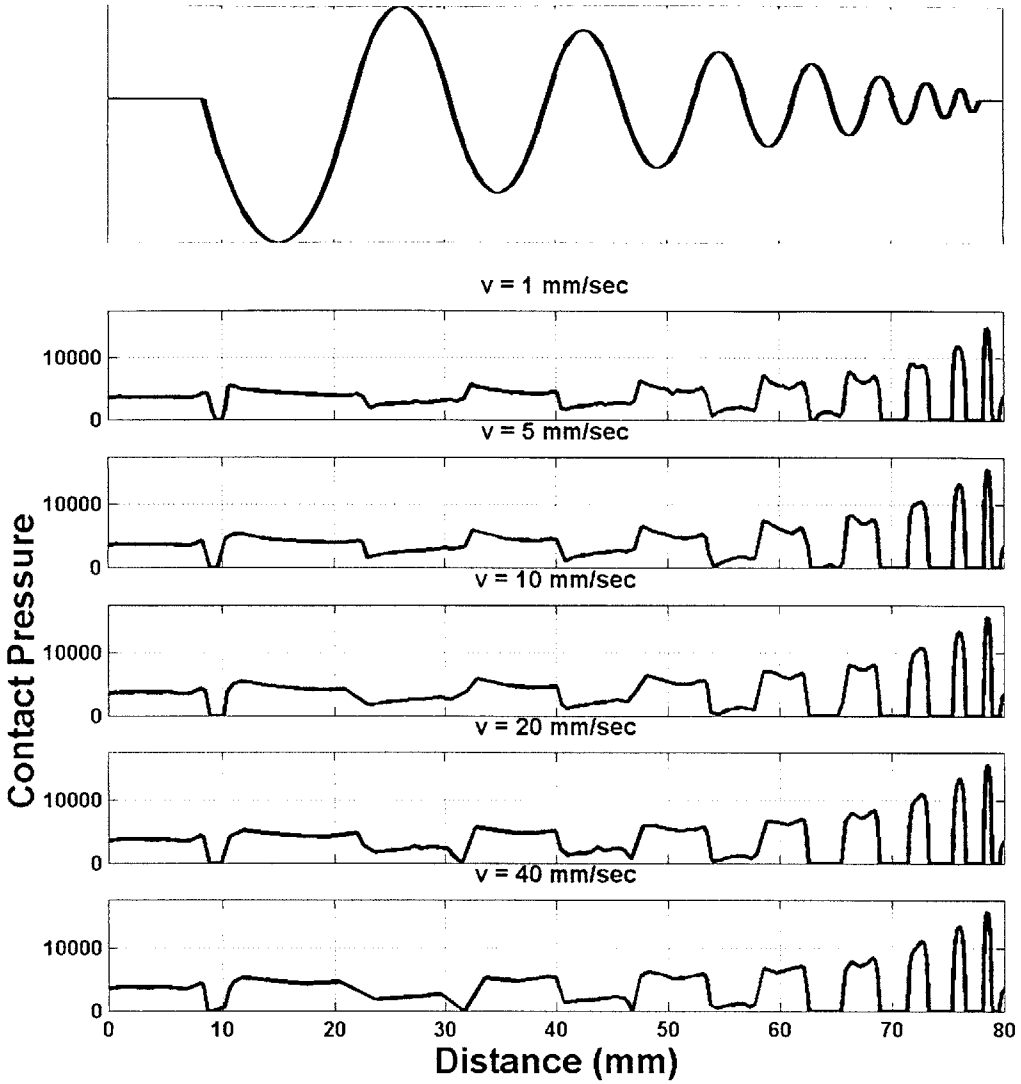

Figure 5-12. FE simulation results. Contact pressure at the center node of the MSS as the wavy surface described in text is stroked across the fingerpad from the broadest curve segment to the sharpest, at velocities of 1, 5, 10, 20, and 40 mm/sec. The convex curvatures that comprise the wavy surface are, from left to right, 26, 39, 52, 79, 105, 157, 210, and 315 m^{-1}.

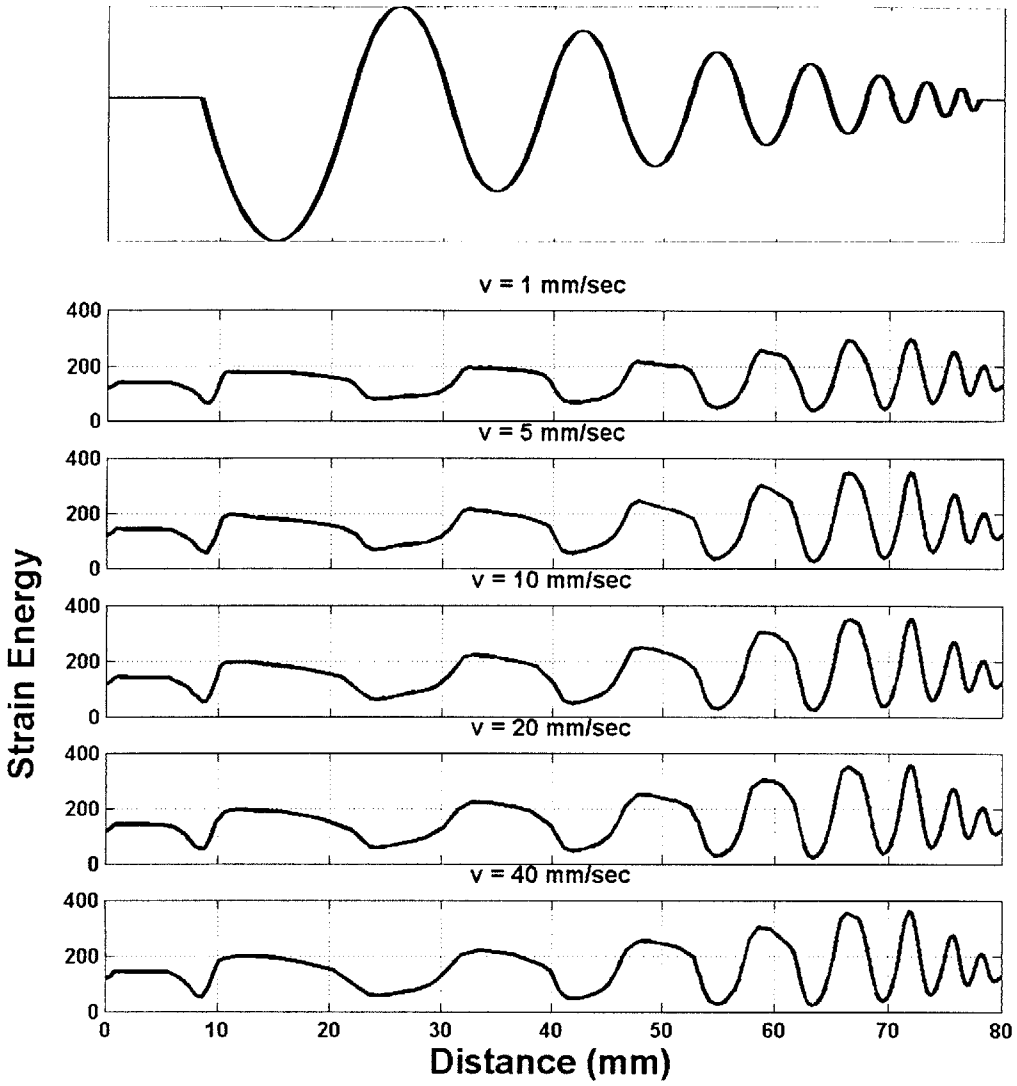

Figure 5-13. FE simulation results. Strain energy at a depth of 915 microns, as the wavy surface described in text is stroked across the fingerpad from the broadest curve segment to the sharpest, at velocities of 1, 5, 10, 20, and 40 mm/sec. The convex curvatures that comprise the wavy surface are, from left to right, 26, 39, 52, 79, 105, 157, 210, and 315 m^{-1}.

In the ramp and hold simulation, equation 4-4 was found to be able to relate the surface contact pressure to the strain energy density. Using this equation, the strain energy was predicted in the stroking simulations. A shift term was added to the equation to account for the lateral displacement of the SA mechanoreceptor. The predicted results are in good agreement with the computed strain energy density, as seen in Figure 5-14. As the stroking velocity increases, the deviation from the predicted strain energy and the computed strain energy increases. This is because the lateral shift was incorporated as a constant, independent of stroking velocity. In reality, the shift is a function of both surface curvature and stroking velocity. Figure 5-15 compares the lateral shift of the center node as the wavy surface is stroked across the surface at velocities of 1, 10, and 40 mm/sec. Clearly the displacement is a complex function that varies over time and velocity. For simplicity, the shift of the SA mechanoreceptor was taken as a constant, independent of velocity, and the results are adequate. A more complex model could account for the small discrepancies, but that is not necessary within the scope of this thesis.

From the neurophysiological recordings, the mean burst width as each curvature segment passed over the fingerpad was found to be independent of velocity (Figure 5-3). The strain energy at a depth of 915 microns was also found to be independent of velocity. This supports the claim that the strain energy density is a candidate relevant stimulus to the SA mechanoreceptor. The burst width can be predicted for each curvature segment, as the length of time the strain energy is above a threshold. Figure 5-16 compares the predicted burst widths with the experimental recordings, for stroking velocities of 5, 10, 20, and 40 mm/sec. The results are in good agreement for all of the curve segments, with the exception of the first broad curvature. The neural response to the first curvature is also influenced by the sharp corner at the beginning of the wavy surface (Figure 5-1), and therefore, the recorded burst width is longer than can be predicted from the strain energy due to the first curvature alone.

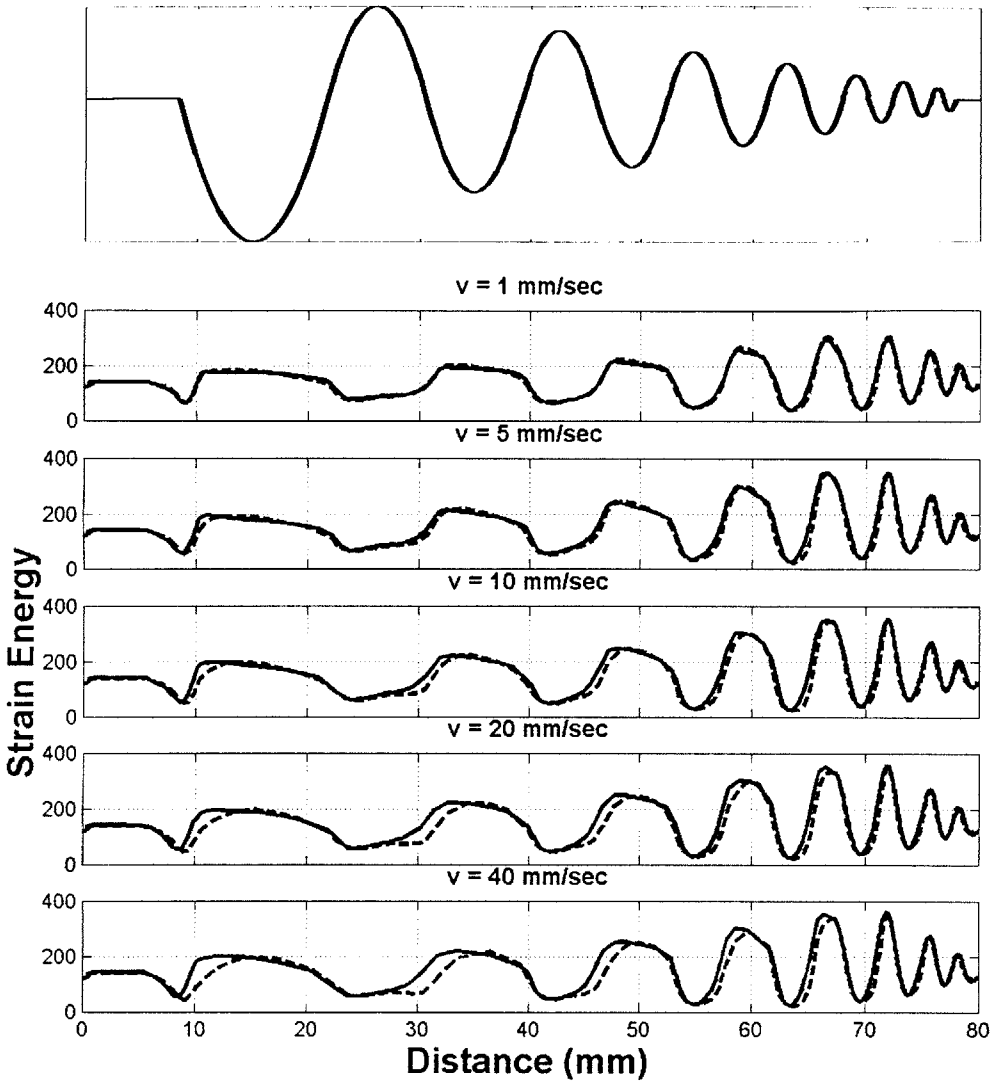

Figure 5-14. Strain energy at a depth of 915 microns (solid lines) as the wavy surface described in text is stroked across the fingerpad from the broadest curve segment to the sharpest, at velocities of 1, 5, 10, 20, and 40 mm/sec. The dashed line is the strain energy predicted by the convolution sum of the contact pressure profile, as described in the text. The convex curvatures that comprise the wavy surface are, from left to right, 26, 39, 52, 79, 105, 157, 210, and 315 m^{-1}.

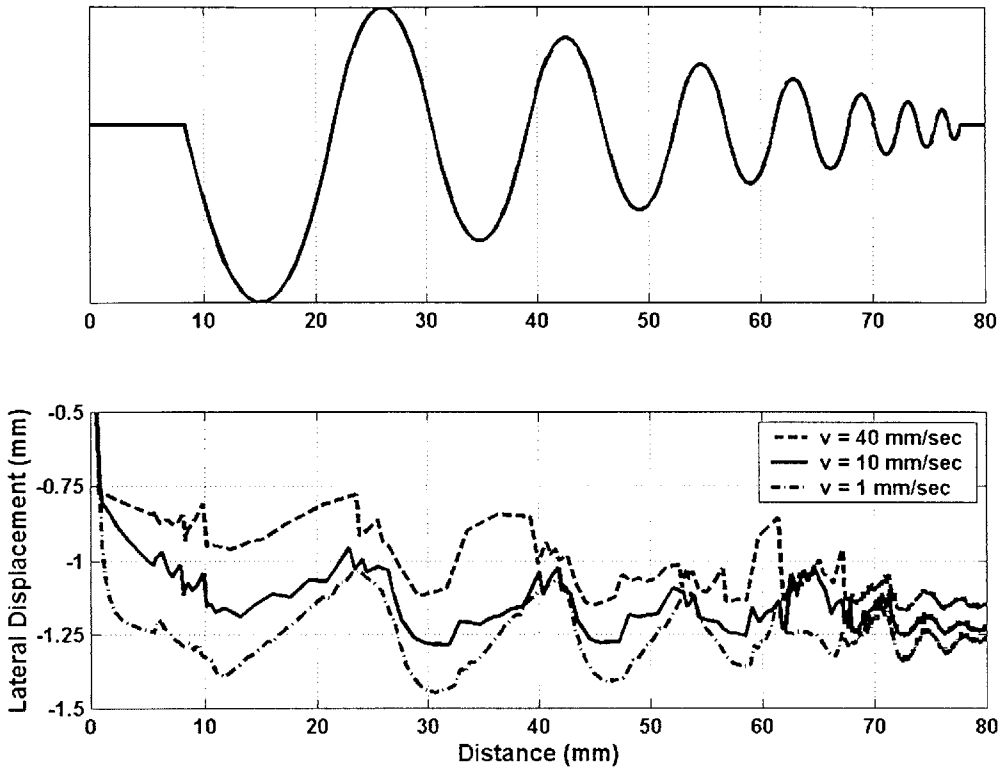

Figure 5-15. Lateral displacement of the center node of the MSS (bottom trace), as the wavy surface in the top trace is stroked across the finger pad from the right to the left, at velocities of 1, 10, and 40 mm/sec. The convex curvatures that comprise the wavy surface are, from left to right, 26, 39, 52, 79, 105, 157, 210, and 315 m^{-1}.

The strain energy cannot by itself predict the burst rate for each velocity of stroking. From examining Figure 5-3, it is clear that the burst rate at for each curvature segment increases as a the stroking velocity increases. The strain energy, however, remains approximately the same within the range of stroking velocities used in the neurophysiological experiments (Fig. 5-13). Also, for a particular stroking velocity, the strain energy does not have the same dependence on curvature as the burst rate recordings exhibit. Figure 5-17 compares the burst rate from a signal SA unit to the wavy surface stroked at a velocity of 10mm/sec, to the ramp and hold response from a single SA unit. The curvatures used in the wavy surface fall in the linear range of the ramp and hold response. For the smallest curvature segments, the stroking response lies between the

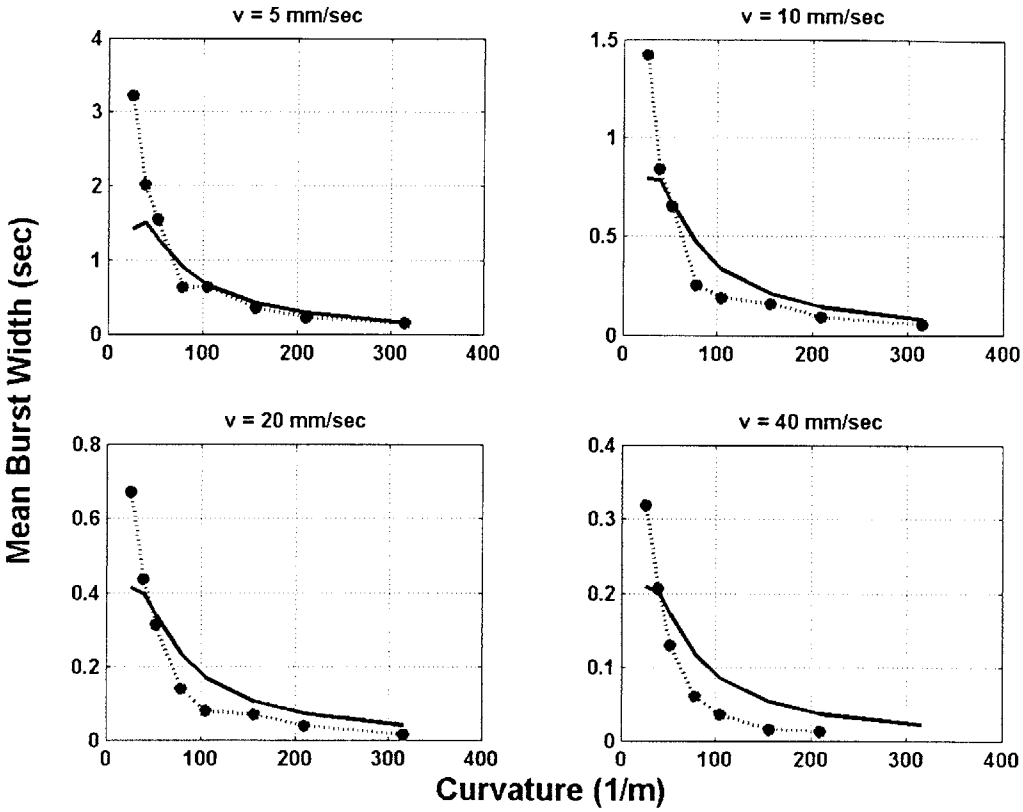

Figure 5-16. Mean burst width of the neural response as the wavy surface described in the text is stroked across the fingerpad at velocities of 5, 10, 20, and 40 mm/sec. The data points are from neurophysiological recordings from a single SA fiber. The solid is the predicted results using the strain energy at a depth of 915 microns, cut-off at a threshold of 150. Note, the burst width is expressed in time ($t = d / v$)

peak ramp and hold response and the steady state response. As the curvature increases the neural response from stroking increases out of the range of the ramp and hold response. The peak strain energy, which is a measure of the overall magnitude of the strain energy for each curvature segment, does not have similar properties as does the neural response. Figure 5-18 compares the peak strain energy from each curvature segment for stroking at 10 mm/sec to the peak strain energy from the ramp and hold simulations. For the smallest curvature, the peaks are approximately the same; but as the curvature increases, the stroking results decrease below those from the ramp and hold simulations. This is not consistent with the characteristics of the neural response shown

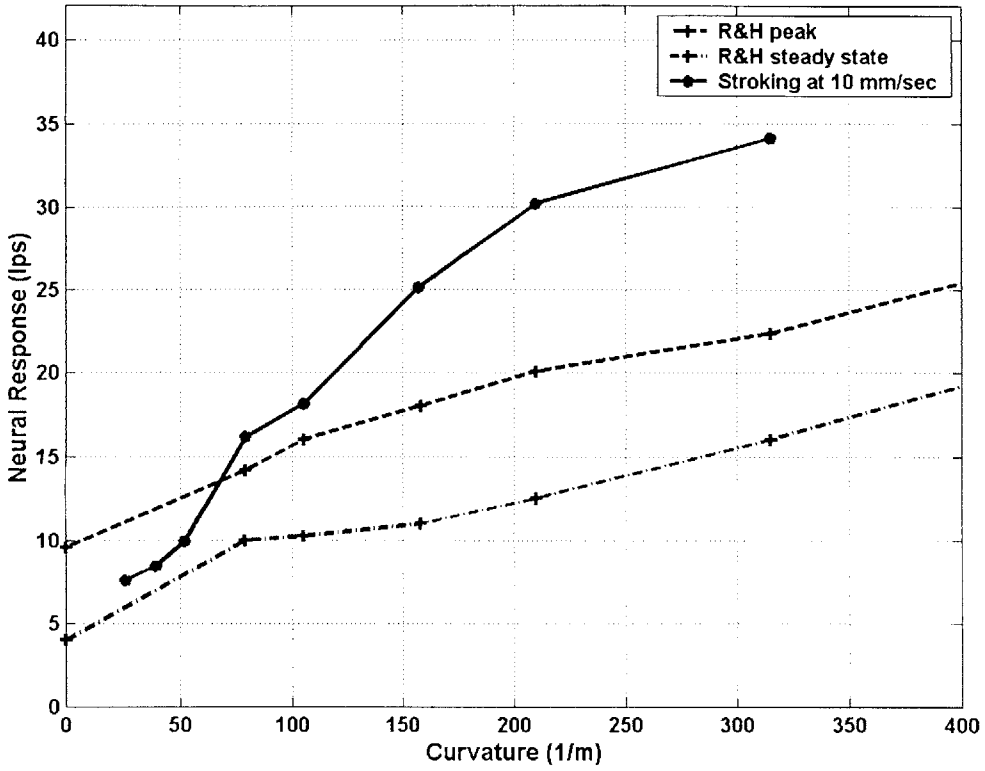

Figure 5-17. Average neural response of an SA fiber as the wavy surface described in the text is stroked across the fingerpad at 10 mm/sec (solid line), compared to the peak and steady state response of the same SA fiber during the ramp and hold experiments with cylinders of various curvatures (chapter 4).

in Figure 5-17. Another mechanism must then account for the SA response due to stroking. As proposed in chapter 4, the strain energy rate is a good candidate as the relevant stimulus to the SA dynamic response. Because the strain energy profile is similar for all stroking velocities used, the strain energy rate for each curvature segment will be directly proportional to the stroking velocity. This corresponds with the finding that the neural response is directly proportional to the stroking velocity, supporting the claim that the strain energy rate is also part of the relevant stimulus for the SA mechanoreceptor.

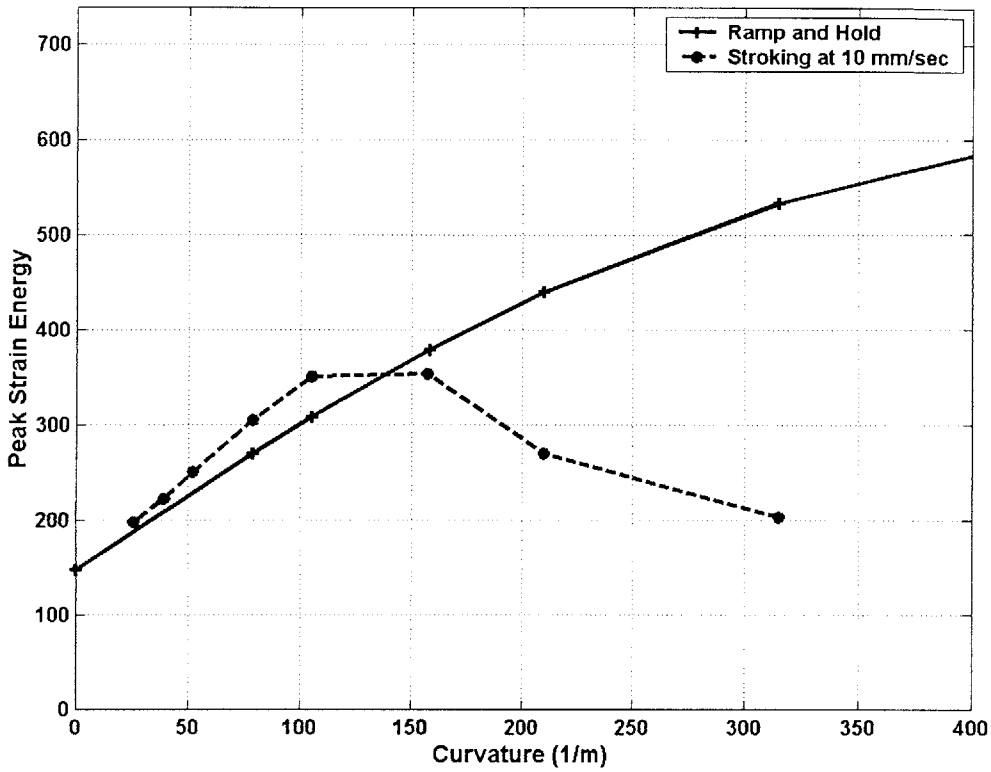

Figure 5-18. Peak strain energy at a depth of 915 microns. Solid line is from ramp and hold indentations with cylinders of various curvatures (chapter 4); dashed line is from the wavy surface described in the text stroked across the fingerpad at v=10 mm/sec.

From the ramp and hold experiment/simulations in chapter 4, the peaks of the neural response were found to be proportional to the peaks in the strain energy rate, while the steady state neural response was governed by the strain energy value. The same observations can be seen to hold for the stroking results. The SA neural response to the wavy surface stroked across the fingerpad at 10 mm/sec are shown in Figure 5-19. Also shown is the strain energy at a depth of 915 microns cut-off at a threshold level of 150, along with the positive strain energy rate. Both the strain energy and the strain energy rate can be used to explain the SA neural response. The peaks of the neural response correspond in time with the peaks of the strain energy rate. For the smaller curvature segments, the decay in the neural response matches in shape and in duration with the

strain energy profiles. As the highest curvature segments stroke across the fingerpad more rapidly (because of smaller widths), the response is brief and steady state is not reached; correspondingly, the neural response is governed predominantly by the strain energy rate.

A simple model is developed to predict the neural response from the strain energy and strain energy rate:

$$Ips = A_1(SE - Thresh_1) + A_2(\frac{dSE}{dt} - Thresh_2) \qquad \textbf{5-1}$$

Ips is the neural response in impulses per second. A_1, A_2, $Thresh_1$, *and* $Thresh_2$ are constants that are fixed for a given mechanoreceptor. Neural impulses recorded from a single SA fiber in wavy surface stroking experiments and ramp and hold indentation experiments imply fixed receptor constants. From finite element simulation data, the neural response is predicted using Equation 5-1 (A_1, A_2, $Thresh_1$, *and* $Thresh_2$ are fixed) for a wavy surface stroked at 10mm/sec and ramp and hold indentations of the surfaces described in Chapter 4. The predicted response is compared to the recorded response in Figures 5-20 and 5-21. The overall agreement between the experimental data and the simulated response is good. For the ramp and hold indentations, the rise and decay portions of the response and the magnitude of the steady state response correlate well with the neurophysiological recordings. The shape and average magnitude of the bursts in the predicted stroking response match with the experimental results. The major discrepancy between the predicted and actual results is in the value of the dynamic peak for each curvature, especially at the end of the indentation ramp. A more complex formulation could account for this difference. The purpose of Equation 5-1, however, is to provide a simple model that describes the general characteristics of SA neural fibers to mechanical loadings during both static and dynamic touch.

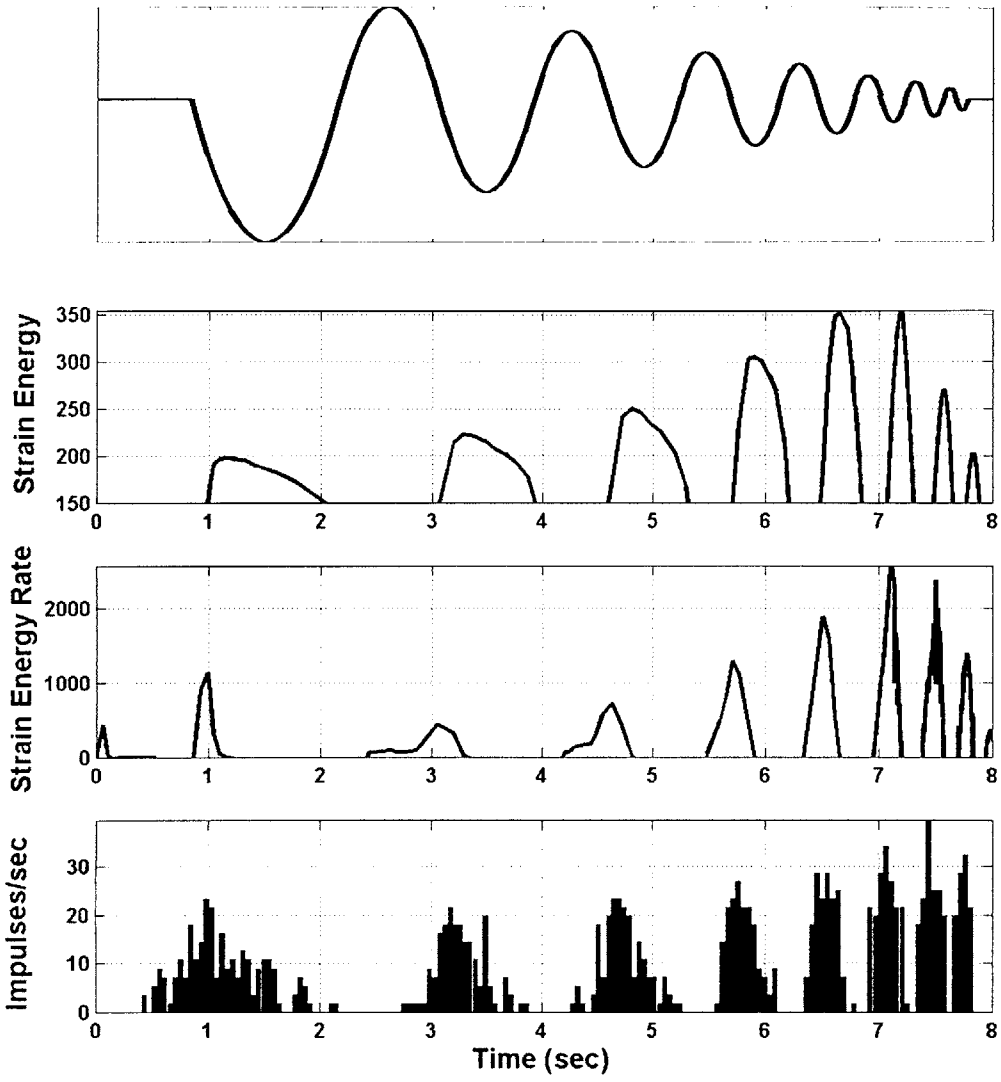

Figure 5-19. Finite element results compared to neurophysiological recordings as the wavy surface in the top trace is stroked across the fingerpad from right to left at a velocity of 10 mm/sec. The top trace is the strain energy at a depth of 915, cut-off at a threshold of 150; the middle trace is the positive strain energy rate at the same depth; the bottom trace is a histogram of the neurophysiological recordings from a single SA fiber (0.5 mm bins were used on 12 separate recordings).

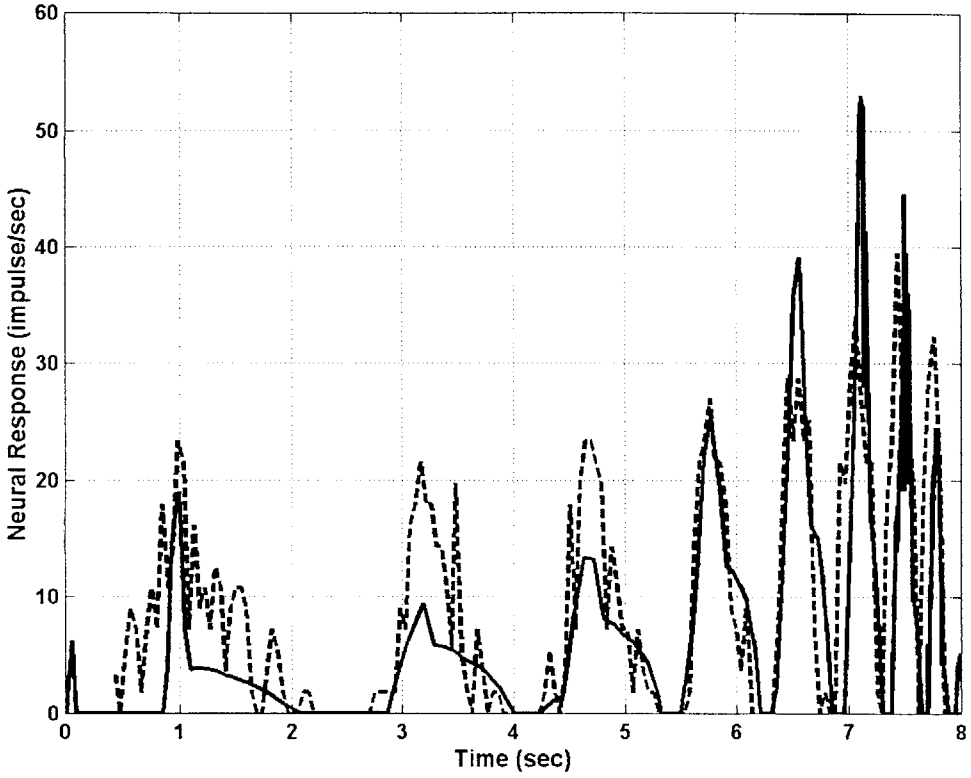

Figure 5-20. Neural response from a single SA fiber as the wavy surface described in text is stroked across the fingerpad at a velocity of 10 mm/sec. (dashed line) The solid line is the neural response predicted from the strain energy and strain energy rate using the equation given in text. ($A_1 = 0.081$; $A_2 = 0.0182$; $Thresh_1 = 150$; $Thresh_2 = 100$)

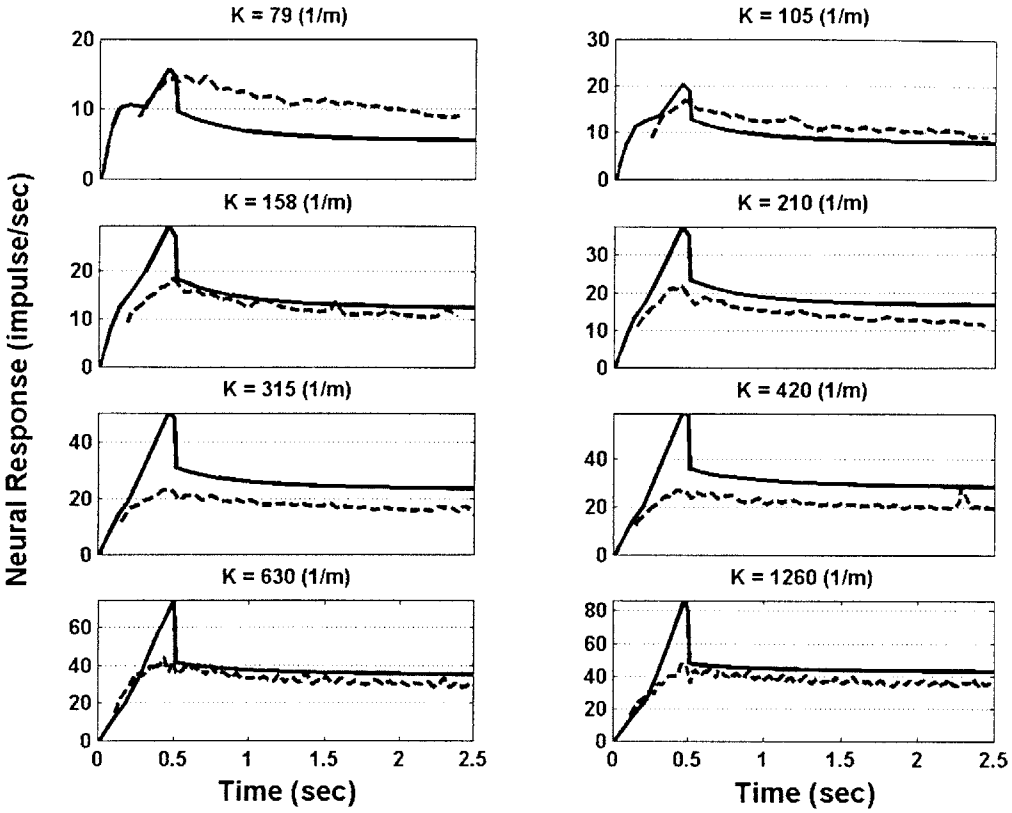

Figure 5-21. Neural response from the same SA fiber used in Fig. 5-21, to the ramp and hold experiments described in chapter 4. (dashed line) The solid line is the neural response predicted from the strain energy and strain energy rate using the equation given in text. ($A_1 = 0.081$; $A_2 = 0.0182$; $Thresh_1 = 150$; $Thresh_2 = 100$)

Occasionally during neurophysiological experiments, responses similar to those shown in Figure 5-22 are recorded. The tick marks in the figure represent four recordings from an SA fiber as a portion of the wavy surface is stroked across the fingerpad at 10 mm/sec. For the first two curvatures, two bursts can be seen as the curvature segments stroke across the fingerpad. This is not an artifact of the trial: for successive trials at various stroking velocities, the same two peak phenomena can be seen for this SA fiber. Figure 5-23 shows the instantaneous frequency of the neural impulses to 12 strokes at velocities of 1, 5, 10, 20, and 40 mm/sec across the fingerpad. The response from the same SA afferent fiber as in Figure 5-22 was recorded. The double peak effect can be seen at each stroking velocity, and the peaks get closer together as the curvature increases.

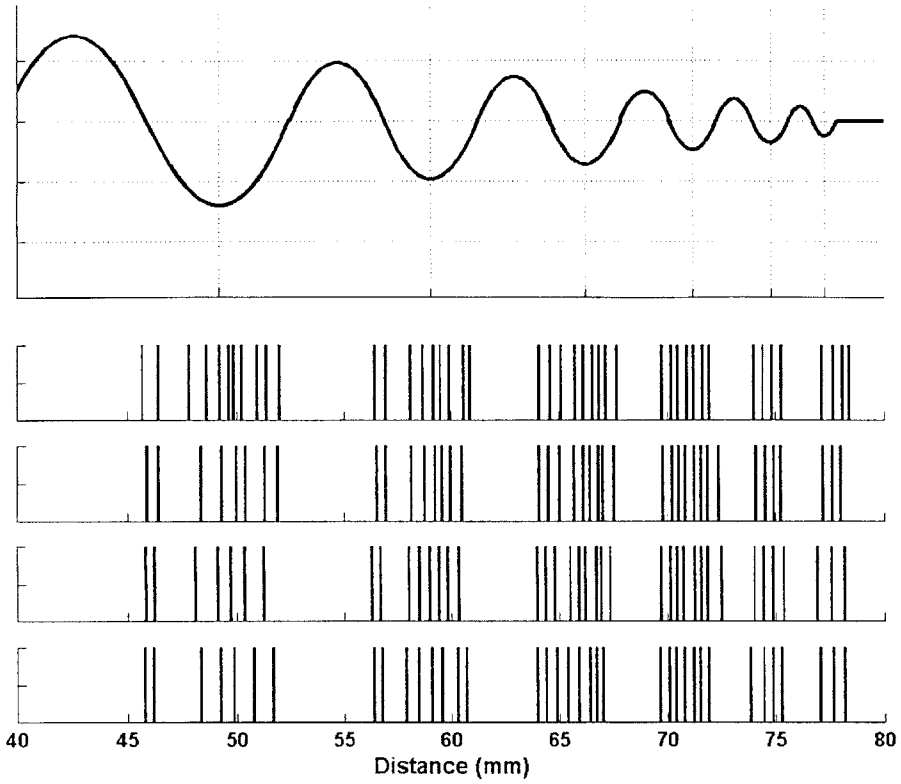

Figure 5-22. Neural response from a single SA mechanoreceptor to a surface of varying curvatures stroked across the fingerpad at a velocity of 10 mm/sec. Four recordings are shown, each tick mark represents one neural impulse. The x-coordinate of each tick mark represents the location on the surface of the most sensitive spot (MSS) in the fiber's receptive field at the time the action potential occurred. The top trace is the surface used, with convex curvatures, in m^{-1}, of 52, 79, 105, 157, 210, and 315. Stroking was from left to right.

Observers often speculate that more than one SA fiber was inadvertently recorded during the experiment, with the MSS for each fiber at different locations across the fingerpad (for the static case, see Phillips and Johnson, 1981). As the surface strokes across the surface, the peak response for each fiber occurs at different times, giving rise to the double peak effect. Although this may be true, the double peak can also be explained by examining the strain energy profiles. Figure 5-24 is the strain energy profile at a depth of 560 microns to the partial wavy surface stroking across the fingerpad at velocities of 1, 5, 10, 20 ,and 40 mm/sec. The same double peak is seen in the strain energy profiles for

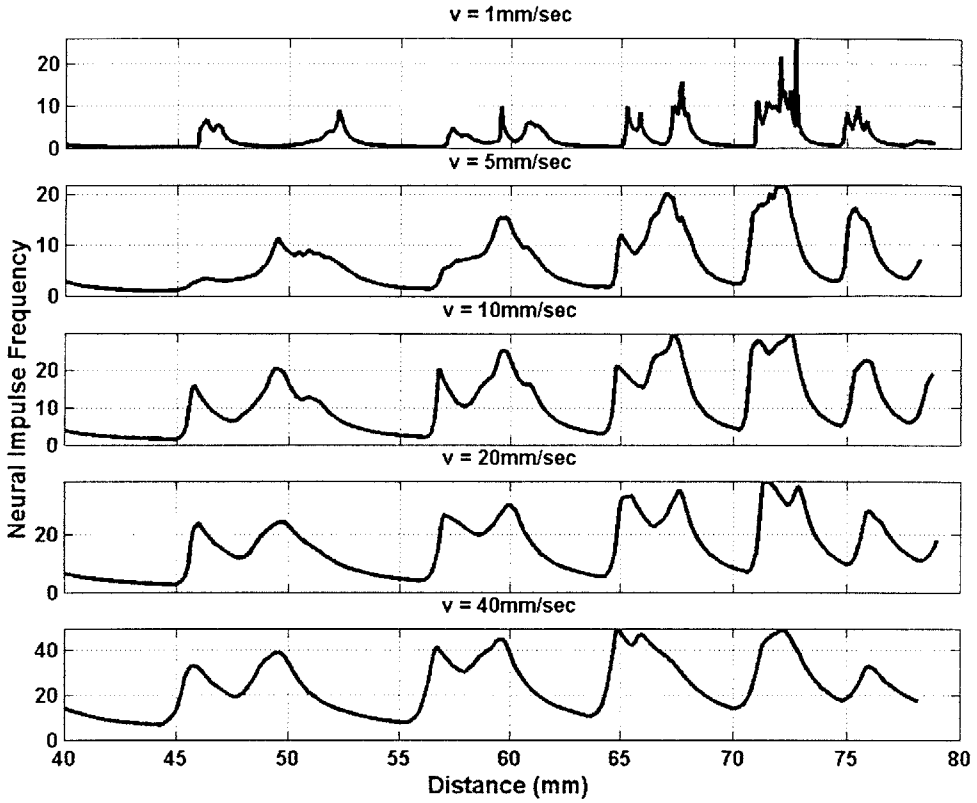

Figure 5-23. Instantaneous frequency of the neural impulses recorded from a single SA mechanoreceptor (S60) to a surface of varying curvatures stroked across the fingerpad at velocities of 1, 5, 10, 20, and 40 mm/sec. The distance represents the location on the surface of the most sensitive spot (MSS) in the fiber's receptive field at the time of the neural impulse firing. The top trace is the surface used, with convex curvatures, in m^{-1}, of 52, 79, 105, 157, 210, and 315. Note: the response from the rightmost curvature is not well-defined due to the fact that the frequency calculation ends of the final tick mark. For the v=40 mm/sec plots only one neural impulse fired for the sharpest curve, and hence, no impulse frequency could be computed. Stroking was from left to right.

each velocity, and the peaks become closer together as the curvature increases, as in the neurological recordings. Therefore, the neural response can be interpreted as the response from a single SA mechanoreceptor, closer to the skin surface. The strain energy and strain energy rate are still valid as the relevant stimuli for the unusual behavior of this SA fiber.

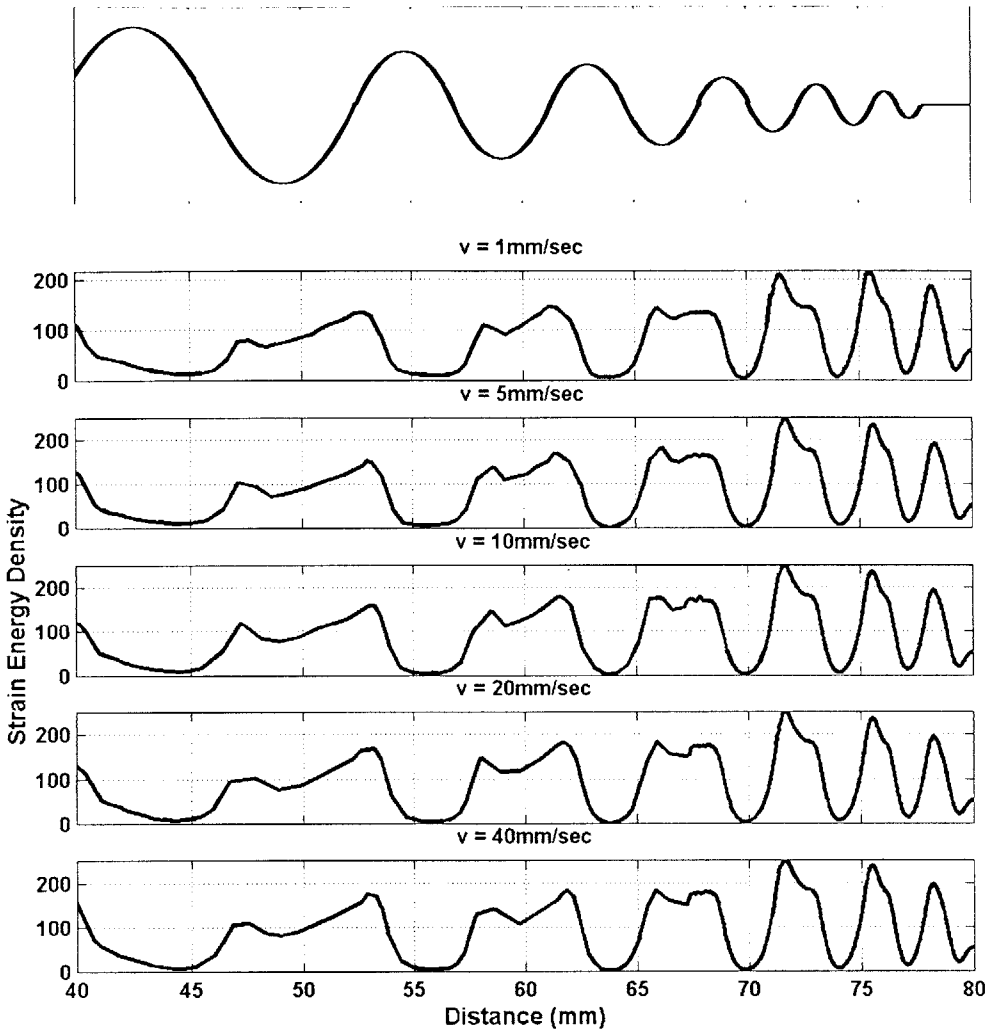

Figure 5-24. Strain energy density at a depth of 560 microns in the center of the fingerpad, computed during simulations of a surface of varying curvatures stroked across the fingerpad at velocities of 1, 5, 10, 20, and 40 mm/sec. The distance represents the horizontal displacement of the surface shown in the top trace. (The corresponding curvatures, in m^{-1}, are 52, 79, 105, 157, 210, and 315.) Stroking was from left to right.

5.5 Inner Ridges

In the fingerpad model used for simulations, there is a straight boundary between the dermis and the epidermis layers. In actuality there exists a series of ridges between the two layers as described in Chapter 2 (Fig. 2-1). The RAs are located at the top of the ridges on the dermis side, while the SAs are in the valleys, both in the dermis and epidermis regions. These ridges were incorporated into the finger model as shown in Figure 5-25. With the modified fingerpad model, the effect of the inner ridges on the strain energy during indentation and stroking can be studied.

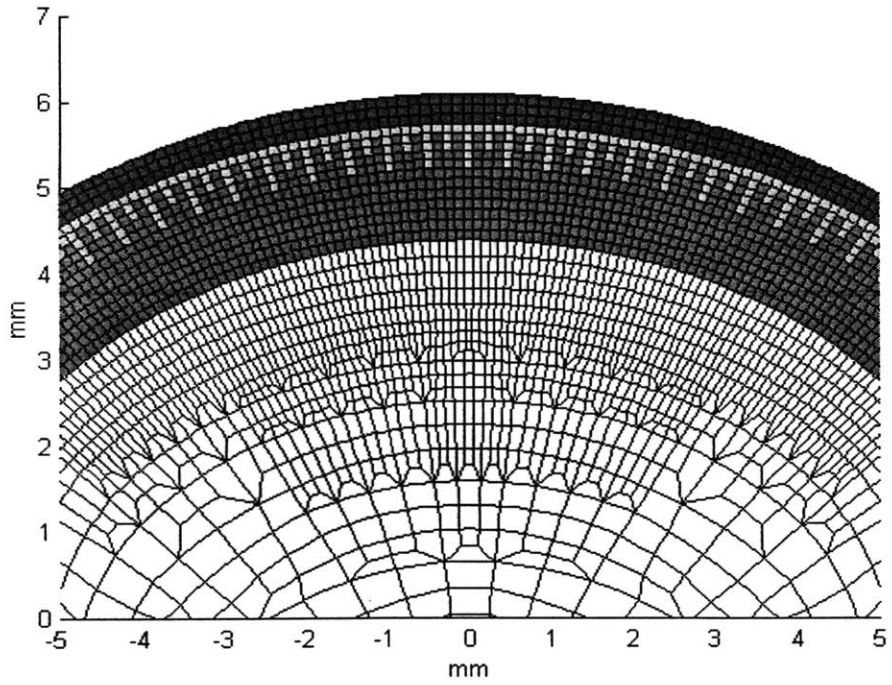

Figure 5-25. Finite element model of the fingerpad with the inner ridges between the dermis and epidermis included. The shaded layers are, from outside to inside, the strateum corneum, epidermis, dermis, and cutaneous fat.

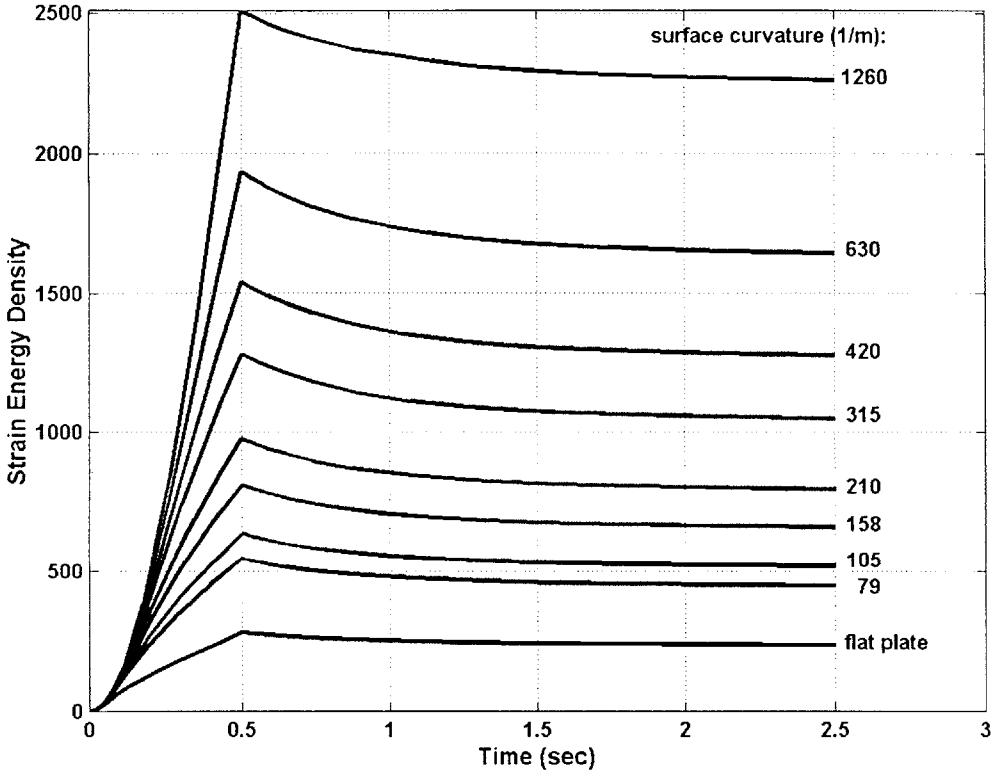

Figure 5-26. Strain energy at a depth of 915 microns, computed during the ramp and hold indentations of the flat plate and curved surfaces. The finite element model incorporating inner ridges was used in the simulations.

The ramp and hold indentations with the nine surfaces used in Chapter 4 were simulated using the fingerpad model with inner ridges. The strain energy results at a depth of 915 microns are shown in Figure 5-26 for each curvature. The profiles have similar characteristics as the strain energy computed using the original model. (refer to Fig. 4-23) The magnitudes differ, and the strain energy for the sharpest curvature in the ridges model has a greater separation in magnitude from the other curvatures. Overall, the profiles have the same rise and fall characteristics, and the same general dependence on curvature.

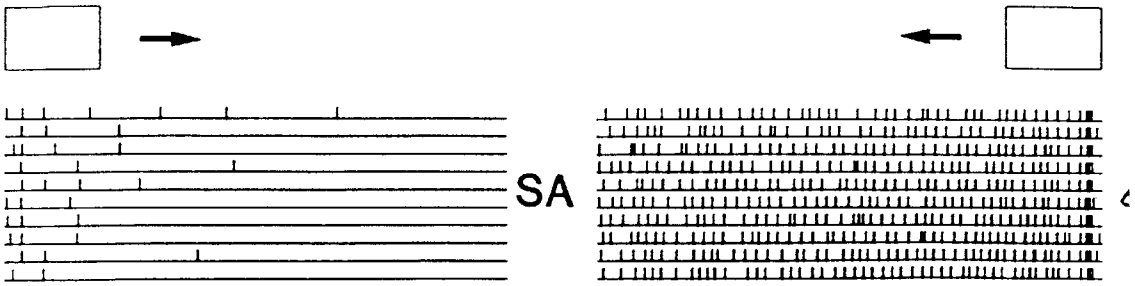

Figure 5-27. Neural response of an SA mechanoreceptive afferent fiber as a blank plate is stroked across the monkey fingerpad in opposite directions, at a velocity of 10 mm/sec and under a constant force of 20 g (adapted from Srinivasan *et. al.*, 1990).

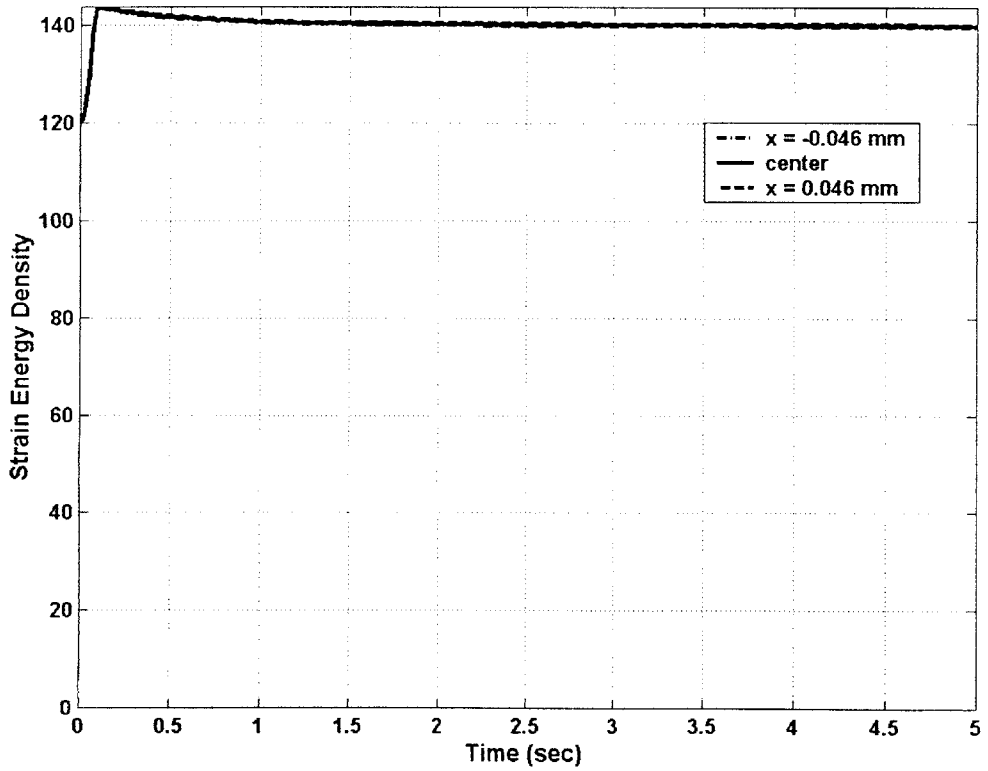

Figure 5-28. Strain energy at a depth of 915 microns, and locations in the center of the fingerpad and 46 microns to the left and right of center. Results are for a flat plate stroked across the fingerpad, from left to right, at a velocity of 10 mm/sec, using the original finite element model of the fingerpad.

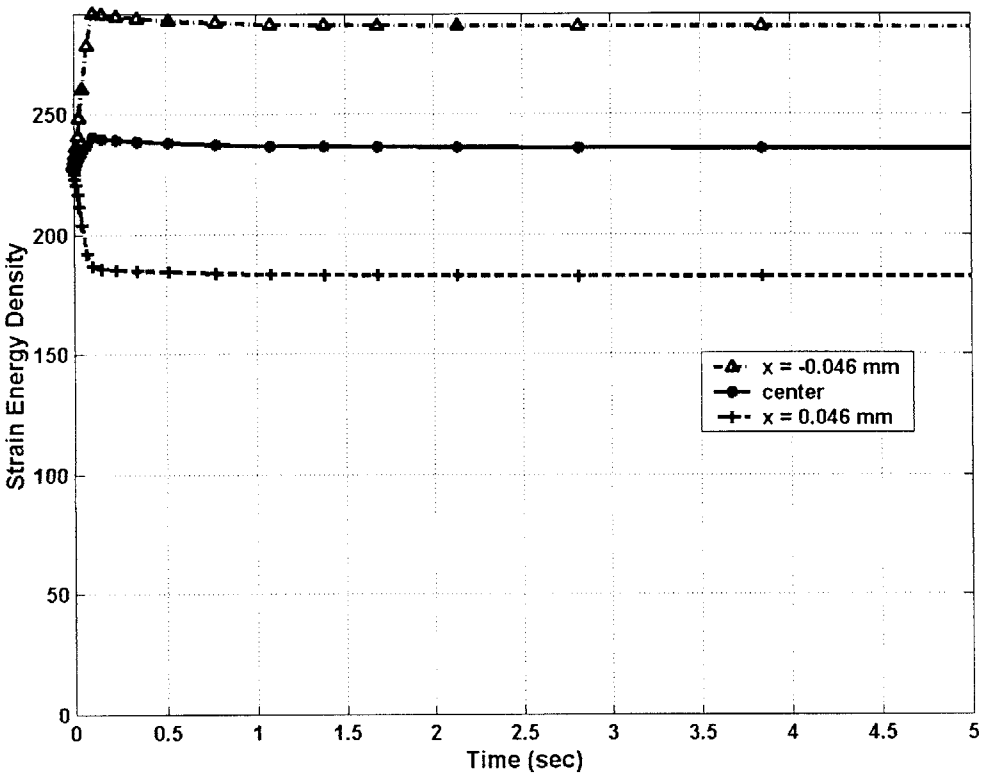

Figure 5-29. Strain energy at a depth of 915 microns, and locations in the center of the fingerpad and 46 microns to the left and right of center. Results are for a flat plate stroked across the fingerpad, from left to right, at a velocity of 10 mm/sec, using the finite element model of the fingerpad incorporating inner ridges.

During ramp and hold indentations, the presence of inner ridges does not play a critical role in the neural response profile. Once lateral movement of the indenting surface is introduced, the inner ridges cause a directional sensitivity in the mechanical response. Srinivasan *et. al.* (1990) observed that as a flat plate is stroked across the fingerpad, the response from an SA fiber can be greatly dependent on the direction of stroking. Figure 5-27 is the response from a single SA afferent to a flat plate stroked across the finger in opposite directions at a velocity of 10 mm/sec and a constant vertical force of 20g. In one direction the SA responds predominantly at the beginning of the stroke, while in the opposite direction the SA responds throughout the entire stroke. The response was measured over 10 trials, and therefore, the directional sensitivity cannot be attributed as

an artifact of the measurement. In the neurophysiological recording, the SA fibers were selected based on the location of their MSS. It is not assured that the receptor is located at the exact center of the fingerpad; a receptor located slightly to the left or to the right of center would have the same MSS as a receptor located directly at the center. The directional sensitivity is likely to depend on the off-center location of the SA fiber. Using the original fingerpad model, without ridges, the flat plate stroking experiment was simulated. The strain energy was computer at a depth of 915 microns at the center of the fingerpad and at locations of ± 46 microns (Figure 5-28). It can be assumed that a receptor located at these three locations would have the same MSS. From Figure 5-28 it can be seen that the strain energy is approximately equal at the three locations, and no directional sensitivity is apparent. Figure 5-29 shows the strain energy at the same three locations, from the flat plate stroking simulation using the model incorporating inner ridges. There is a large difference in magnitude between the strain energy at each location. If an SA receptor were located just 50 microns of center, the response in one direction of stroking would be significantly greater than the response in the opposite direction. The incorporation of inner ridges into the fingerpad model can explain the directional sensitivity seen in the neurophysiological experiments.

6

Summary

This thesis focused on furthering the understanding of the biomechanics involved in the human tactile system. A finite element model of the human fingerpad was developed of the human fingerpad in order to investigate the skin dynamics of tactile sensing. Neurophysiological recordings obtained previously from SA receptors in macaque monkeys were compared with finite element simulation results to gain insight into tactile encoding of shape.

Model Generation

Using previously obtained MRI images of the human fingerpad, a two dimensional finite element model of the fingerpad was developed, with accurate internal tissue layer boundaries. The material properties for each layer of the model were estimated from experimental data previously obtained from human subjects. The model was validated against MRI images of deformed and undeformed human fingertips, surface deformation profiles and force response data on human subjects. The major contributions of this model are the addition of realistic internal geometry and the incorporation of viscoelastic time constants in order to model skin dynamics.

Biomechanics Simulations

Using the fingerpad model created, finite element simulations were conducted in order to understand the biomechanics of touch. Cylinders of various curvatures were indented into the skin at a constant force. The contact pressure on the skin surface was found to be directly dependent on the surface curvature. The pressure at each point on the skin is linearly dependent on the local displacement, for small displacements only. At large displacements, there is a nonlinear relationship between the local pressure and the local displacement across the fingerpad. The strain energy at the depth of the SA mechanoreceptors is a low pass filtered version of the contact pressure profile at the skin surface. A convolution sum of the contact pressure at each point on the skin surface can approximate the strain energy below the skin for a broad range of surface curvatures.

A wavy surface of alternating concavities and convexities, with varying curvatures, was stroked across the skin surface at different velocities. The contact pressure across the skin surface is directly dependent on the local curvature. The stroking velocity did not have a profound effect on the contact pressure distribution. The strain energy at the depth of the mechanoreceptors could be predicted by the convolution sum of the contact pressure distribution proposed for the indentation studies. However, due to skin stretch during stroking, a shift factor must be included in the summation.

Neurophysiological Comparisons

Neurophysiological recordings from previous indentation and stroking experiments were compared with results from the finite element simulations. In general, the SA neural response is directly dependent on surface curvature and stroking velocity. For the ramp and hold indentation experiments, the dynamics of the neural response during the ramp phase and the peak response can be predicted by the strain energy rate. The slow decay of the response during the hold phase can be predicted by the strain energy. The neural response for the wavy surface stroked at various velocities can be predicted by a linear combination of the strain energy and strain energy rate.

Effect of Inner Ridges

The internal ridges between the dermis and epidermis layers were included into the model in order to study their effect. The SA mechanoreceptors are located at the base of these ridges. The inner ridges appear to be important to the directional sensitivity of SA mechanoreceptors during stroking. For locations a small lateral distance from the center of the fingerpad, the strain energy is greatly dependent on the direction of stroking. This same stroking dependence is seen in the neurophysiological recordings.

7

Future Work

In order to fully understand the human tactile system, continued research is necessary. With a fingerpad model that can predict the skin dynamics of touch, the role of rapidly adapting (RA) mechanoreceptors can be studied. The neurophysiological data is available from RA units during indentation and stroking experiments. Using the finite element model created, the relevant stimulus can be determined from matching simulation results with the neural recordings. Determining the firing mechanism for RA afferents, coupled with the knowledge of SA afferents, would lead to a powerful understanding of the complete tactile system in the human fingerpad.

Preliminary studies on the role of internal ridges has shown great promise in understanding the directional sensitivity of mechanoreceptors. In the current model, the resolution of the inner ridges is not sufficient to fully believe in the results. A new model with finer resolution should be created that includes the internal ridges as well as the ridges at the surface of the fingerpad. This would allow for further studies on the effect of the internal and external ridges on the biomechanics of touch.

While the finite element simulations can give an estimate to the contact pressure distribution across the fingerpad, it would be useful to be able to determine the pressure distribution experimentally. Microelectromechanical Systems (MEMS) devices offer that ability. Technology is constantly improving, and it is feasible that a device could be manufactured that can measure the contact pressure across the fingerpad dynamically

during touch. Other optical techniques are available that could possibly measure the steady state pressure profile. Using these techniques, the results from the finite element simulation could be validated with experimental measurements of contact pressure distributions. In addition, it has been shown in this thesis that the strain energy at the mechanoreceptor depth can be predicted from the contact pressure distribution across the skin surface. A tactile sensor array could be developed that mimics the human tactile system by measuring the pressure distribution, computing the strain energy from the convolution sum, and predicting the neural response of the afferent fibers. A device such as this would be of great benefit to robotic touch sensors and smart prosthetic fingers.

The finite element modeling techniques can predict the mechanical state of the fingerpad during touch, and with the neurophysiological recordings, the relevant stimulus of the mechanoreceptors can be determined. However, the underlying mechanism of the afferent neural fibers is still not well understood. There are many theories on the role of stretch activated receptors and the release of neurotransmitters during mechanical loading. In order to completely understand the human tactile system, the mechanoreceptors and afferent fibers must be studied at a molecular level. The following question must be answered: how are the stresses and strains on the mechanoreceptors transduced into a series of electrical impulses?

References

1. Abaqus, Abaqus/Standard User's Manual, Hibbit, Karlsson & Sorensen, Pawtucket, R.I., **1998.**
2. Akoev, G. N., Mechanoreceptors, their functional organization, Springer-Verlag, Berlin, **1988**.
3. Bathe, Klaus-Jurgen, Finite Element Procedures, Prentice Hall, Upper Saddle River, New Jersey, **1996**.
4. Bolanowski, S. J., Gescheider, G. A., Verillo, R. T., and Checkosky, C. M., "Four channels mediate the mechanical aspects of touch," *J. Acoust. Soc. Am.*, vol. 84, no. 5, pp. 1680-1694, **1988.**
5. Burgess, P. R. and Perl, E. R., in Handbook of Sensory Physiology, ed. Iggo, A., Springer, Berlin, vol. 2, pp. 29–78, **1973.**
6. Dandekar, K. and Srinivasan, M. A., "Role of Mechanics in Tactile Sensing of Shape," Touch Lab Rpeort 2, *RLE Technical Report – 604*, MIT, **1996.**
7. Darian-Smtih, I., "The sense of touch: performance and peripheral neural processes," Handbook of Physiology – The Nervous System III, pp. 739-788., **1984.**
8. De, S. and Srinivasan, M. A., "A finite element model of the human fingertip incorporating viscoelasticity, **1999.** (manuscript in preparation for *Journal of Biomechanics*)
9. Duncan, Sophie. *http://eleceng.ukc.ac.uk/~sd5/research/nn_index.html*
10. Freeman, A. W. and Johnson, K. O., "Cutaneous mechanoreceptors in macaque monkey: Temporal discharge patterns evoked by vibration, and a receptor model," *Journal of Physiology*, vol. 323, pp. 21-41, **1982a.**

11. Freeman, A. W. and Johnson, K. O., "A model accounting for effects of vibratory amplitude on responses of cutaneous mechanoreceptors in macaque monkey," *Journal of Physiology*, vol. 323, pp. 43-64, **1982b.**

12. Goodwin, A. W., Browning, A. S., and Wheat, H. E., "Representation of curved surfaces in responses of mechanoreceptive afferent fibers innervating the monkey's fingerpad," *Journal of Neuroscience*, vol. 15,no. 1, pp. 798-810, **1995.**

13. Goodwin, A. W., John, K.T., and Marceglia, A. H., "Tactile discrimination of curvature by humans using only cutaneous information from the fingerpads," *Experimental brain research*, vol. 86, pp. 663-672, **1991.**

14. Goodwin, A. W. and Morley, J. W., "Sinusoidal movement of a grating across the monkey's fingerpad: Representation of grating and movement features in afferent fiber responses," *Journal of Neuroscience*, vol. 7, no. 7, pp. 2138-2180, **1987a.**

15. Goodwin, A. W. and Morley, J. W., "Sinusoidal movement of a grating across the monkey's fingerpad: Temporal patterns of afferent fiber responses," *Journal of Neuroscience*, vol. 7, no. 7, pp. 2181-2191, **1987b.**

16. Goodwin, A. W. and Wheat, H. E., "Human tactile discrimination of curvature when contact area with the skin remains constant," *Experimental brain research*, vol. 88, pp. 447-450, **1992.**

17. Guass, C. F., "Disquisitiones generales circa superficies curvas." *Commentationes Societatis Regiae Scientiarum Gottingenesis Recentiores,* vol. 6, pp. 99-147, **1827.**

18. Gulati, R. J. and Srinivasan, M. A., "Determination of Mechanical Properties of the Human Fingerpad, *in vivo*, Using a Tactile Stimulator," Touch Lab Report 3, *RLE Technical Report -605*, MIT, 1996.

19. Ho. C.-H. and Srinivasan, M., "Human haptic discrimination of thickness," Touch Lab Report 6, *RLE Technical Report – 608*, MIT, **1996**.

20. Hodgkin A. L. and Huxley A. F., "A quantitative description of membrane current and its application to conduction and excitation in nerve," Journal of Physiology, pp. 117-500, **1952.**

21. Johansson, R. S. and Vallbo, A. K., "Tactile sensory coding in the glabrous skin of the human hand," *Trends in Neuroscience*, Elsevier Biomedical Press, Cambridge, vol. 6, no. 1, pp. 27-32, **1983.**

22. John, K. T., Goodwin, A. W., and Darian-smith, I., "Tactual discrimination of thickness," *Experimental brain research*, vol. 78, no. 1, pp. 62-68, **1989.**

23. Lamb, G. D., "Tactile discrimination of textured surfaces: Psychophysical performance measurements in humans," *Journal of Physiology (London)*, vol. 338, pp.551-565, **1983.**

24. LaMotte, R. H. and Srinivasan, M .A., "Responses of cutaneous mechanoreceptors to the shape of objects applies to the primate fingerpad," *Acta Psychologica*, vol. 84, pp. 41-51, **1993.**

25. LaMotte, R. H. and Srinivasan, M .A., "Neural encoding of shape: Response o cutaneous mechanoreceptors to a wavy surface stroked across the monkey fingerpad," *Journal of Neurophysiology*, vol. 76, no. 6, pp. 3787-3797, **1996.**

26. Lanir, Y., Dikstein, S., Hartzshtark, A., and Manny, V., "*In Vivo* Indentation of Human Skin," *Journal of Biomechanics*, vol. 112, pp. 63-69, **1990.**

27. Lederman, S. J. and Taylor, M. M., "Fingertip force, surface geometry, and the perception of roughness by active touch," *Perception & Psychophysics*, vol. 12, pp. 401-408, **1972.**

28. Levitan, I. B., The neuron: cell and molecular biology, Oxford University Press, New York, **1991.**

29. Liao, J. C. and Srinivasan, M. A., "Experimental Investigation of Frictional Properties of the Human Finger Pad," Touch Lab Report 11, *RLE Technical Report – 629*, MIT, September, **1999.**

30. Lochhart, R. D., Fyfe, F. W., and Hamilton, G. F., "The Skin," *Anatomy of the human body*, J. P. Lippincott Company, Philadelphia, pp. 3-6, **1965.**

31. Loomis, J. M., "An investigation of tactile hyperacuity," *Sensory Processes,* vol. 3, pp. 289-302, **1979.**

32. Phillips, J. R. and Johnson, K. O., "Tactile spatial resolution – II. Neural representation of bars, edges and gratings in monkey primary afferents," *J. Neurophysiol.*, vol. 46, pp. 1192-1203 **1981a.**

33. Phillips, J. R. and Johnson, K. O., "Tactile spatial resolution – III. A continuum mechanics model of skin predicting mechanoreceptor responses to bars, edges and gratings," *J. Neurophysiol*, vol. 46, pp. 1204-1225, **1981b**.

34. Raju, B. I. and Srinivasan, M. A., "Encoding and Decoding of Shape in Tactile Sensing," Touch Lab Report 12, *RLE Technical Report – 630*, MIT, September, **1999.**

35. Srinivasan, M. A., "Surface deflection of primate fingertip under line load," *J. Biomechanics*, vol. 22, no. 4, pp. 343-349, **1989.**

36. Srinivasan, M. A. and LaMotte, R. H., "Tactile discrimination of shape: Responses of slowly adapting mechanoreceptive afferents to a step stroked across the monkey fingerpad," *Journal of Neuroscience*, vol. 7, no. 6, pp.1655-1671, **1987a.**

37. Srinivasan, M. A. and LaMotte, R. H., "Tactile discrimination of shape: Responses of rapidly adapting mechanoreceptive afferents to a step stroked across the monkey fingerpad," *Journal of Neuroscience*, vol. 7, no. 6, pp.1672-1681, **1987b.**

38. Srinivasan, M. A. and LaMotte, R. H., "Tactile discrimination of shape: Responses of slowly and rapidly adapting mechanoreceptive afferents to a step indented into the monkey fingerpad," *Journal of Neuroscience*, vol. 7, no. 6, pp.1682-1697, **1987c.**

39. Srinivasan, M. A. and LaMotte, R. H., "Encoding of Shape in the Responses of Cutaneous Mechanoreceptors," Information Processing in the Somatosensory System, Franzen and Westman, Wenner-Gren International Symposioum Seires, MacMillan Press, pp. 59-69, **1991.**

40. Srinivasan, M. A. and LaMotte, R. H., "Tactual discrimination of softness," *J. Neurophysiol.*, vol. 73, no. 1, pp. 88-101, **1995**.

41. Srinivasan, M. A., Whitehouse, J. M., and LaMotte, R. H., "Tactile detection of slip: Surface microgeometry and peripheral neural codes," *Journal of Neurophysiology*, vol. 63, no. 6, pp. 1323-1332, **1990.**

42. Talbot, W. H., Darian-Smith, I., Kornhuber, H. H., and Mountcastle, V. B., "The sense of flutter-vibribatrion: Comparison of the human capacity with response

patterns of mechanoreceptive afferents from the monkey hand," *J. Neurophsyiol.*, vol. 31, pp. 301-334, **1968.**

43. Tubiana, R., The Hand, W. B. Saunders Company, Philadelphia, **1981.**

44. Voss., K. J. and Srinivasan, M. A., "Investigation of the Internal Geometry and Mechanics of the Human Fingertip, *in vivo*, using Magnetic Resonance Imaging," Touch Lab Report 10, *RLE Technical Report – 622*, MIT, January, **1998**.